Structural studies on cyanobacterial trimeric Photosystem I-related protein complexes

A Doctoral Thesis

By

Li Jiannan

Submitted to the Graduate School of Science, Osaka University

Graduate School of Science, Osaka University

Acknowledgments

During the academic and scientific training as a Ph.D. candidate at Osaka University from 2017, I have received innumerable help and support from many, many people. Professor Genji Kurisu admitted me as a member of the Laboratory for Protein Crystallography, which made it possible to set sail to Japan and study abroad as an international student. His support throughout, not only from an academic aspect but also from financial support during my extension period, was the most important cornerstone of my eventual study achievements. I feel so lucky to meet such a kind and approachable supervisor, and would like to express sincere appreciation to him. Hopefully I can enjoy much communication and cooperation with this learned and elegant scholar also in the future.

Moreover, many lab mates devoted valuable efforts to the research projects. I would especially appreciate Dr. Christoph Gerle and Ms. Yuko Misumi who teach me from almost zero about many practical techniques from cyanobacteria cultivation to the usage of electron microscopy and academic writing. I will never forget their warm and patient guidance, and would like to express my sincere thanks to them here. As a predecessor with a similar research topic, Dr. Orkun Çoruh generously shared his academic and experimental experience with me, and the productive communication with this easy-going partner brought me countless inspirations and gains.

The smooth progress of the research project was due to the generous support from fellows and collaborators. Here I would like to appreciate Dr. Hideaki Tanaka and Dr. Akihiro Kawamoto for their kind help, especially in Cryo-EM data processing and modeling. I would also express gratitude to Professor Keiichi Namba and Dr. Fumiaki Makino for their valuable support and suggestions in the Cryo-EM data collection, which made it possible to obtain Cryo-EM single particle analysis results at impressive resolution. Meanwhile, Professor Young-Ho Lee and Dr. Yuxi Lin should be highly appreciated for their excellent ITC measurement support, which made our research conclusion sounder and more informative. Furthermore, Mr. Noriyuki Hamaoka generously prepared and offered the Ga-substituted

Ferredoxin to me, who should be thought of as my first research cooperative fellow as a young scholar. I wish him a successful and fruitful Ph.D. career as an active explorer. Moreover, without the routine maintenance of related scientific facilities, which was supported by Professor Takayuki Kato and Dr. Mika Hirose, the research project could not progress smoothly. I express my sincere thanks to all these enthusiastic and knowledgeable scientists.

The scientific communications and academic guidance gave concrete progress and polishing to the conclusion and discussion described in this thesis. I would like to thank Dr. Takanori Nakane and Dr. Hiroyasu Koteishi for their active and hearty comments on my research project. Meanwhile, I would also thank all the reviewers for their careful supervision of this thesis, their comments were precious for me to polish my description of research results during the doctoral period. Besides, the experimental material utilized in this research project was a gift from Prof. Matthias Rögner's laboratory at Ruhr-University Bochum (German). Here I sincerely appreciate Emeritus Professor Matthias Rögner and his successor Professor Marc M. Nowaczyk, whose relevant research achievements and suggestions to this project were constructive and precious.

Living abroad is not always smooth sailing, I would like to express my heartfelt gratefulness to the laboratory secretary Ms. Miho Tsutsui and her successor Ms. Satoe Tomita for their great help and assistance when I met troubles in daily life. With their warm concern, I could still feel the family-like warmness even far from home. Moreover, all the lab members, especially Ms. Naoko Norioka, Ms. Jennifer Neumann, and Mr. Seolmin Ko, were solid supporters of my daily research life. I would like to share my joy of graduation with these sincere friends and hope our friendship will never end.

My former girlfriend and current wife, Ms. Li Aonan, followed me to Japan after graduation and continued her study as a Ph.D. student in the Graduate School of Dentistry, Osaka University. Her unselfish love and warm accompany are the sources of my courage and confidence. I will love, honor, comfort, and cherish her forsaking all others, keeping only unto her for as long as we shall live, for better for worse, for richer or poorer, in sickness and

in health, to love, honor, and cherish until death do us part.

My dear families, especially my mother Peng Hui, father Li Lijun, and my grandparents, are always supporting me unconditionally and immutably. They taught me to be honest and trustworthy from when I was a kid, and I hope I can make them proud with all my academic achievements and contributions to science.

Finally, but most importantly, I would like to express my sincere appreciation to the Chinese Scholarship Council, which financially supported me and my wife’s studying in Japan. In my perspective, such support in essence derived from every single Chinese people. I am more than willing to offer my efforts and time to build China a better country and make people's lives better, even the contributions may be minuscule and faint.

There are still lots of people’s names not being listed here, but their help and support will be kept in my mind. One cannot grow without the support and encouragement of others, and I also want to be a man who can support and help others. The scientific exploration never ends, and I hope my work could push it forward even if just a little bit.

李 剣南

李 剣南

Li Jiannan

Symbols and Abbreviations

Photosystem I	PSI
Cytochrome	Cyt
NADH-like complex I	NDH1
Great Oxidation Event	GOE
Plastocyanin	Pc
Ferredoxin	Fd
Flavodoxin	Fld
Electron Transport Chain	ETC
nicotinamide adenine dinucleotide phosphate	$NADP^+$
Light Harvesting Chlorophyll protein	LHC
Chlorophyll	Chl
Sucrose Density Gradient	SDG
Electron Microscopy	EM
Sodium Dodecyl Sulfate Poly Acrylamide Gel Electrophoresis	SDS-PAGE
Charge-Coupled Device	CCD
Poly Ethylene Glycol	PEG
Super Photon ring-8 GeV	SPring-8
Plastoquinone	PQ
Gallium-substituted Ferredoxin	GaFd
Nuclear Magnetic Resonance	NMR
Ferredoxin $NADP^+$ oxidoreductase	FNR
Isothermal Titration Calorimetry	ITC
glyco-diosgenin	GDN
n-dodecyl-β-D-maltoside	β-DDM
lauryl maltose neopentyl glycol	LMNG

Ammonium Sulfate	AS
Fast Protein Liquid Chromatography	FPLC
Immobilized Metal Affinity Chromatography	IMAC
Ultraviolet-visible	UV-Vis
Luria-Bertani	LB
hydrogen chloride	HCl
Contrast Transfer Function	CTF
Fourier Shell Correlation	FSC
Protein Data Bank	PDB
Electron Microscopy Public Image Archive	EMPIAR
Electron Microscopy Data Bank	EMDB
critical micelle concentration	CMC

TABLE OF CONTENTS

Chapter I. Abstract

Oxygenic photosynthesis is the most fundamental biochemical process, not only because it provides us with food, energy, and a variety of valuable substances, but also because it supports almost all life on Earth, either implicitly or explicitly. The complete photosynthetic process consist of complex physical and chemical reactions, which start with light absorption, followed by excitation energy transfer to the reaction centers, primary photochemistry (charge separation), electron and proton transport, NADPH and ATP synthesis, and finalized by CO_2 fixation to stable carbon products and their export to other cells.

The photon absorption process starts in the thylakoid membrane with two light reactions taking place simultaneously at photosystem II and photosystem I (PSI) reaction centers. All photoautotrophic species, including cyanobacteria, algae, and higher plants, utilize both pigment-protein antenna complexes to capture light energy and convert it to redox chemical energy with high efficiency.

It is commonly assumed that the debut of oxygenic photosynthesis corresponded with Cyanobacteria's birth. Cyanobacterial PSI mainly exists in homo-trimeric form and contains numerous protein subunits along with plenty of pigments and cofactors. The exploration of cyanobacterial photosystems, especially the determination of the structure of these old but huge protein-pigments complexes will help our better understanding of the origin of photosynthesis of the early Earth and the development of photoautotrophic evolution.

In this thesis, the purification trials and structural analysis are described with the cyanobacterial PSI trimer as the study focus. Chapter 2 is about the purification of PSI trimers from the thermophilic cyanobacteria *Thermosynechococcus elongatus* BP-1. This includes experiments on the crystallization and optimization of the crystallization condition for X-ray diffraction measurements aimed at obtaining high resolution structure information. Chapter 3 describes how PSI trimer sample was mixed together with its electron transfer partners: the Cytochrome c_6 as the electron donor and the Ferredoxin as the electron acceptor. Moreover,

detailed structure determination of the PSI-centered triple electron-transfer complex using cryo-EM single-particle analysis and the use of the resulting density map for modeling at high resolution were described in this chapter. The topic of chapter 4 is the exploration of iron-starved cyanobacteria for the expression of extra antenna proteins (IsiAs) surrounding PSI trimers. Comprehensive purification trials were performed to obtain PSI-IsiA supercomplex at high purity and homogeneity. At last, the overall evaluation and conclusion of all experimental results were included in Chapter 5.

Keywords

Photosynthesis, Cyanobacteria, Photosystem I, Electron transfer, Cryo-EM

Chapter II. Isolation and crystallization trials of PSI trimers

2.1 Introduction

2.1.1 The most important chemical reaction on earth——Photosynthesis

Except for a few chemosynthetic autotrophs, practically all life on modern Earth is reliant on solar energy. Photosynthesis is the most basic biological reaction, which converts solar energy into chemical energy. Photosynthesis can be defined as the biological collection and storage of light energy, with the stored energy being used to power energy-intensive cellular processes. By far, the most common type of photosynthesis used by living organisms is oxygenic photosynthesis[1]. The complete oxygenic photosynthesis operation is made up of a succession of intricate physical and chemical processes that begin with photon absorption and end with the export of stabilized carbon compounds[2]. Although there are significant changes in the overall process of oxygenic photosynthesis in plants, algae, and cyanobacteria, the basic mechanism is fairly similar.

There are two stages[3] of oxygenic photosynthesis: 1) Light-dependent reactions, also known as light reactions, capture the energy of light and use it to generate the hydrogen carrier NADPH and the energy-storage molecule ATP in the first stage. 2) The light-independent reactions (carbon reactions[4], also termed as "dark" reactions) utilize these products to capture and reduce carbon dioxide during the second stage. Oxygenic phototrophs, from cyanobacteria to algae and higher plants, have specialized membrane-bound compartments called thylakoids[5,6] where major photosynthetic reactions took place. Within the thylakoid membrane, four major membrane protein complexes, Photosystem II, Cytochrome (Cyt) b_6f, Photosystem I (PSI), and NADH-like complex I (NDH1) functioned as an electron transport chain[7–10].

2.1.2 Primitive photosynthetic autotrophs——Cyanobacteria

At least eight bacterial lineages have photosynthetic reaction centers today[11,12]: Cyanobacteria, Proteobacteria, Chloroflflexi, Acidobacteria, Chlorobi, Firmicutes,

Gemmatimonadetes, and the recently discovered Candidatus Eremiobacterota. Since oxygenic photosynthesis is only found in cyanobacteria and other bacteria have evolved different types of anoxygenic photosynthesis[13], it is commonly assumed that the debut of oxygenic photosynthesis corresponded with the presence of Cyanobacteria.

Cyanobacteria are photosynthetic prokaryotes present in a variety of lighted habitats, and probably exercised the most significant quantitative impact on the planet[14]. Cyanobacteria are one of the most morphologically diverse prokaryotic groups, with growth forms ranging from unicellular to filamentous and multicellular[14,15]. A thousand million tons of wet biomass was estimated to be their global weight[16]. It is currently thought that photosystems were the first to evolve the ability to undertake water oxidation, and that as photosystems became more specialized, this led to what we now call oxygenic photosynthesis[17–19]. Consequently, crown-group Cyanobacteria may have become the dominant primary producers near the late Archean period (around 2.5 billion years ago) as oxygenic photosynthesis reached a higher level of complexity and sophistication[20]. Furthermore, based on the endosymbiotic theory (Symbiogenesis[21,22]), cyanobacteria were thought as the origin of chloroplasts in algae and higher plants. Despite various changes[23] in appearance and a considerably degraded chloroplast genome when compared to that of autonomous cyanobacteria, sequence alignment analysis of the remaining sections revealed a relationship between them[24,25].

Chlorophyll[26] was generated in cyanobacteria to funnel photons into the reaction center as the driving force of electron transfer, whereas water was used as an electron donor, culminating towards the liberation of oxygen[27]. Such a series of reactions generalized as oxygenic photosynthesis were indicated as a possible cause of the Great Oxidation Event (GOE)[28,29], which triggered dramatic changes in the Earth's surficial environment and significantly altered the composition of life forms. The identification and investigation of cyanobacteria's photosynthetic mechanism were crucial in understanding the origin and evolution of photosynthetic systems, as well as the interaction of

photoautotrophs with their living environment.

The idea of two light-dependent reactions and two basic types of photosystems began with Robert Emerson and Charleton Lewis's experiments[30] in 1943 on the “red drop” in the action spectrum of the quantum yield of photosynthesis and the 1957 “Emerson enhancement” effect[31,32], in which the rate of photosynthesis in two lights presented together was higher than the total of the rates of photosynthesis measured when the two lights were supplied individually. The well-known “Z-scheme” of photosynthesis was born as a result of these observations[33,34] (See **Fig. 2-1**). The isolation and characterization of the high-resolution spatial structure of PSII[35] and PSI[36] using X-ray crystallography provided physical support for the presence and organization of the two photosystems.

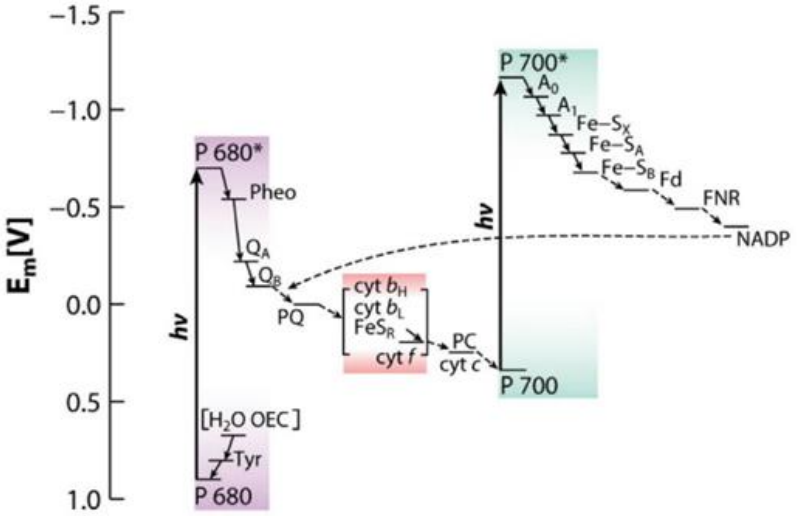

Figure 2-1 Energy diagram of the electron transport pathway, incorporating the major reactions of photosynthesis into what is called the “Z-scheme” of photosynthesis[2].

2.1.3 The Photosystem I in cyanobacteria

The PSI is a multi-subunit protein complex anchored in the thylakoid that is involved in photosynthetic light-dependent processes[37]. As a light-driven membrane-embedded subassembly, the PSI may be the most efficient energy converter in nature, with a

quantum efficiency of about 100%[37]. The PSI played the role of electron transfer with a name as “plastocyanin–ferredoxin oxidoreductase[38]” because the reaction center of PSI catalyzed the oxidation[39] of reduced Plastocyanin (Pc) or Cytochrome c_6 (Cyt c_6) and reduction[40] of soluble Ferredoxin (Fd) or Flavodoxin (Fld). Emitted photons can be used by the protein complex to stimulate the flow of electrons across the thylakoid membrane through Electron Transport Chain (ETC). The light energy absorbed by pigment-protein antenna complexes of the photosystems is converted into redox chemical energy with very high efficiency, whereas a small part of the energy is dissipated as heat (internal conversion), and as chlorophyll (Chl) fluorescence[41].

Based on the immunological analysis results[42], protomer of cyanobacterial PSI contain 12 subunits (termed as PsaA-PsaF, PsaI-PsaM, and PsaX) whereas higher plants PSI has a total of 14 polypeptides. Another notable distinction is the presence of the cyanobacterial PSI complex in oligomeric forms[43,44], which mainly exist in homo-trimeric[36], and some in a monomeric[45] or tetrameric[46] form, whereas in higher plants and algae[47] PSI is only found as a monomer.

The overall layout of the PSI trimer resembles a cloverleaf in the prior structures determined by X-ray crystallography[36], with its threefold rotation axis matching with the crystallographic C3 axis (3-fold rotational symmetry). The contacts at the center of trimerization domain are contributed mainly by subunit PsaL at the core of PSI trimer. Three subunits at the PSI stromal side (to keep definition uniform, in this thesis, we specified cytoplasmic side in cyanobacteria as stromal side according to the definition of thylakoid in the chloroplast) are without transmembrane domains (PsaC, PsaD, and PsaE), and the other nine subunits contain transmembrane α-helices. At each center of a PSI protomer, PsaA and PsaB form a pseudo dimer orientated parallel to the C3 axis and coordinating most key cofactors of the ETC. In addition, most of the pigments related to energy transfer, carotenoids and internal lipids are also bound to the PsaA/PsaB pseudo-dimer. Moreover, the first atomic model of cyanobacterial PSI[36] suggested

potential docking sites of electron transfer partners namely Pc/Cyt c_6 and Fd/Fld based on the structural features for possible inter-protein interactions.

In the PSI reaction center, charge separation takes place at a special pair of chlorophyll *a* molecules (termed as P700) using photon energy funneled by surrounding antenna pigments[48]. The activated electron is then transferred through the internal ETC, and finally relayed to the downstream soluble electron acceptor (usually Fd served this role) at the stromal side[49]. The reduced electron acceptor Fd is a strong reductant, providing electrons in a variety of downstream reactions such as the reduction of nicotinamide adenine dinucleotide phosphate ($NADP^+$), nitrogen and sulfur assimilation, fatty acid desaturation among others[50,51]. The excited P700 (termed as P700*) has lost an electron and is then subsequently reduced by an electron donor protein (Cyt c_6 or Pc) bound at the luminal side, sequentially launching the next round of electron transfer[52]. For a more detailed descriptions about the PSI electron transfer process, please refer to Chapter 3.

2.1.4 Progress in the structural exploration of PSI

The X-ray structure of trimeric cyanobacterial PSI from *Thermosynechococcus elongatus* (formerly named as *Synechococcus elongatus*) was determined in 2001 at 2.5 Å resolution (PDB ID: 1JB0[36]), and later that from *Synechocystis* sp. PCC 6803 at same resolution (PDB ID: 5OY0[53]). This resolution of 2.5 Å was the highest record for a long time. Recently, several other PSI structures, including green plant-type PSI complexed with light-harvesting chlorophyll proteins I (LHCI), were revealed at better resolution by X-ray crystallography and later by Cryogenic Electron Microscopy (Cryo-EM): PSI-LHCI from pea at 2.393 Å (PDB ID: 7DKZ[54]), and two PSI-LHCI complexes from diatom at 2.38 and 2.4 Å (PDB IDs: 6LY5[55], 6L4U[56]). Benefiting from the resolution revolution of Cryo-EM[57], two more Cryo-EM structures of cyanobacterial PSI at slightly better resolution were published: trimeric PSI from *Halomicronema hongdechloris* C2206 at 2.35 Å (PDB ID: 6KMW[58]), and tetrameric PSI from a heterocyst-forming *Anabaena* sp.

PCC7120 at 2.37 Å (PDB ID: 6K61[46]).

2.1.4 Research motivation and target

A precise atomic model of PSI built based on maps at higher resolution can complete missing parts of the current structure, and give deeper insights about cofactor arrangement. To build a better atomic model of this huge protein-pigment complex by the X-ray diffraction method purification and crystallization trials of cyanobacterial Photosystem I (PSI) trimer were performed and are described detail in this chapter. The thermophilic cyanobacterium, *Thermosynechococcus elongatus* (*T. elongatus*) BP-1, which was originally isolated from a hot spring in Beppu (Japan), was cultivated for PSI trimer extraction and purification reasoning that its thermostability is advantageous for structural analysis. Gene modification was performed in the laboratory of Prof. Matthias Rögner at Ruhr-University Bochum (Germany) and the mutant was given to us as a kind gift for facilitation of cell cultivation and protein purification.

2.2 Materials and Methods

2.2.1 Culture conditions

Thermophilic cyanobacteria of the *T. elongatus* BP-1 mutant strain, genetically modified with an N-terminal His_{10}-tag on the PsaF subunit as well as a chloramphenicol-resistant gene as a selectable marker, were cultivated under illumination for the purification of PSI trimers. Cultivation was performed under continuous illumination at 30 µM photons m^{-2} s^{-1} at 50 ℃ in BG11 medium as described previously[41]. A total of 16 L culture solution was harvested when the $OD_{730\ nm}$ absorbance reached 1.0. His-tagged PSI trimers were purified from thylakoid membranes according to Kubota *et al*.[42] with minor modifications as following described.

2.2.2 Cell disruption

Harvested cells were concentrated by centrifugation (8,000 g, 2 min at 4℃, JLA

9.1000 rotor, Avanti™ HP-26XP), re-suspended in Buffer A (50 mM MES (pH 6.5) 25% glycerol, 20 mM $CaCl_2$, 20 mM $MgCl_2$) and then frozen by liquid nitrogen for storage at -80℃ or used immediately for cell disruption by the beads-beating method as previous described[43]. Cells were disrupted in freshly prepared pre-cooled Buffer B (same components as in Buffer A with the addition of 1 mM Benzamidine, 1 mM 6-aminohexanoic acid, 1 mM PMSF solubilized in ethanol, and 1 mM DNase I) and thylakoid membranes were separated from soluble cellular contents by ultracentrifugation (40,000 g, 30 min at 4℃, P50AT2 rotor, HITACHI himac CP80WX).

2.2.3 Isolation of thylakoid membrane

Thylakoid membranes were re-suspended in Buffer A at a chlorophyll concentration of 1 mg/mL, and subsequently a 10% β-DDM stock solution was added dropwise until the concentration of β-DDM in buffer reached 1%. Then the mixture was incubated in the dark at 4℃ with gentle stirring for 45 min. After membrane solubilization, insoluble contents were removed by ultracentrifugation (50,000 g, 30 min at 4℃, P50AT2 rotor, HITACHI himac CP80WX) and the supernatant was applied to an open column with Ni-NTA Sepharose (Qiagen). PSI trimers were eluted from the column using Buffer C (20 mM MES (pH 6.5), 20 mM $CaCl_2$, 20 mM $MgCl_2$, 0.05% β-DDM and 100 mM imidazole). Eluted PSI trimers were concentrated by ultrafiltration (Amicon15 ultrafiltration tubes, 100 kDa MWCO at 3,000 g and 4℃) to a final chlorophyll concentration of ~10 mg/mL.

2.2.4 Chlorophyll concentration measurement

The chlorophyll concentration (C_{chl}) was measured by a spectrophotometer (U5100, Hitachi) based on previous protocol. For PSI-related samples, chlorophyll concentration was determined by measuring absorbance at wavelength of 663 nm (A_{663}) in 80% acetone as C_{chl} (mg/mL) =12.17×A_{663}. Based on the chlorophyll molecular weight ratio in PSI, the PSI protein concentration (C_{pro}) could be calculated as C_{pro} (mg/mL)=C_{chl}×3.92.

2.2.5 Sucrose Density Gradient (SDG) centrifugation

The concentrated PSI trimer sample was polished by SDG centrifugation for optimal homogeneity and purity. The step gradient buffer was prepared containing 20 mM MES (pH 6.5), 20 mM $CaCl_2$, 20 mM $MgCl_2$, 0.05% β-DDM and sucrose concentration were 40% (w/v), 30%, 20% and 10% from centrifuge tube bottom to top respectively. Step gradient buffers were applied at the top of Ultra-Clear™ centrifuge tubes (Beckman Coulter™) gently using a 5 mL pipette in sequence from highest sucrose (bottom) to lowest (top). The total volume for each tube was 30 mL (7.5 mL for each step buffer). Gradient buffer mixture should be prepared before use (within 3 hours), and maximum 1 mL concentrated PSI sample could be loaded at top of each tube. Centrifugation was performed at 4℃ with speed of 20,000 g for 20 hours (P28S rotor, HITACHI himac CP80WX). After centrifugation, each separated bounds were extracted carefully in sequence from top to bottom for following SDS-PAGE and negative staining EM.

2.2.6 SDS-PAGE

Subunit composition analysis of isolated bounds extracted from SDG centrifugation was performed by standard polyacrylamide gel electrophoresis. After desalting (PD-10 with buffer same as SDG step buffer but without sucrose) and concentration (Amicon4 ultrafiltration tubes, 100 kDa MWCO) purified PSI was mixed with SJ-sample buffer, heated at 60℃ for 30 min. After short centrifugation (2 min, 10,000 g at 20℃), samples of each bounds were applied on the polymerized SDS gel with 18% acrylamide concentration. The PSI subunits were separated at voltage of 120 V in 2 hours. After electrophoresis, protein staining was performed by using CBB Stain One Super (NACALAI TESQUE) through standard protocol.

2.2.7 Negative stain EM

Protein sample quality were assessed by negative staining EM. An aliquot of 3.5 μL

final sample was diluted 1/100 and applied to glow-discharged (5 mA, 10 s, Eiko) continuous carbon film coated copper grids (Nisshin EM). Staining was performed by applying 3.5 μL 2% uranyl acetate solution. After incubation for 30 s, staining solution was blotted by filter paper (Whatman #1) and dried at room temperature. EM grids were inspected using a H-7650 HITACHI transmission electron microscope at 80 kV acceleration voltage equipped with a 1 x 1 K Tietz FastScan-F114 CCD camera.

2.2.8 Crystallizing initial screening

To explore proper precipitants for crystallization of PSI, various crystallization reagent kits were used for initial crystallizing condition screening. Accurate, reproducible automation of screening tests was realized by a robotic crystallization system (Mosquito LCP-136, TTP Labtech). **Table 2-1** listed all involved crystallization reagent kits. Total 1 μL of protein sample was automatically mixed with 1 μL of diluted precipitant buffer in VCP-1 96 well plate. Mixture droplets were sealed by scotch tape and incubated in dark at 20℃. Crystals appeared from around 3 days after mixing with precipitant buffer, and photos of typical crystals were collected as **Fig. 2-4** presented.

Crystallization reagent kit (commodity code)	Company	Dilution
PEG/Ion Screen™ (HR2-126)	Hampton research	34%, 25%
Crystal Screen 2 Cryo™ (HR2-121)	Hampton research	34%, 20%
PEG/Ion 2 Screen™ (HR2-098)	Hampton research	34%, 25%
Crystal Screen™ (HR2-110)	Hampton research	50%, 34%
MembFac™ (HR2-114)	Hampton research	50%, 34%
MemGold™(MD1–39)	Molecular Dimensions	50%, 34%, 25%
MemGold2™(MD1–63)	Molecular Dimensions	50%, 34%, 25%
MemStart™ (MD1-21)	Molecular Dimensions	100%, 50%
MemSys™ (MD1-25)	Molecular Dimensions	100%, 50%

Table 2-1 Crystallization reagent kit used for initial screening.

2.2.9 Crystal optimization

In order to get X-ray diffraction results with higher resolution and quality, optimizations of crystal were performed including precipitant buffer optimization, seeding and additive screening. Various Cryo-protectants were also tested for the elimination of ice rings in diffraction patterns. The **Fig. 2-5** showed typical crystals obtained after various optimized conditions were applied.

Precipitant buffer optimization was performed based on result of crystallizing initial screening. Optimal concentration of each component was determined based on optimization screening tests (for each condition, at least 3 repeats were preformed). For each well, 3 μL PSI trimers at concentration of 10 mg/mL in buffer containing 20 mM MES (pH 6.5), 2% (w/v) glycerol, 20 mM $CaCl_2$, 20 mM $MgCl_2$ and 0.05% β-DDM were mixed with equivalent precipitant buffer at ratio of 1:1. Protein sample and precipitant buffer was mixed in VCP-1 96 well plate, and mixture droplets were covered by 2 μL mineral oil to avoid evaporation. Plates were sealed by scotch tape and incubated in dark at 20℃. Crystals with regular parallelepiped contour and large size (around 1 mm length) were observed in precipitant condition of 100 mM $(NH_4)_2SO_4$, 50 mM NaCl, 50 mM Sodium citrate (pH 6.0) and 8-12 % (w/v) PEG 2000.

Micro-seeding and macro-seeding trials were performed to get optimal crystals. PSI trimers crystals derived from optimized crystallization condition described above were collected and crushed by Seed bead™ (HR2-320, Hampton research) with standard protocol. Crystal debris were diluted by precipitant buffer in various dilution degrees. Micro-seeding was realized by mixing protein sample of PSI trimers with diluted crystal debris as described above. **Figure 2-5** presented typical crystals obtained by micro-seeding. For macro-seeding, complete crystals from 96 well plate were picked up and put into mixture droplets of protein sample and precipitant buffer. In the same figure, typical crystals obtained by macro-seeding were also presented.

Additive screening test was performed by using Additive Screen HT™ (HR2-138,

Hampton research) kit. Total 96 unique additives were tested for optimizing crystal quality. Total 5 μL of protein sample was mixed with 4 μL of precipitant buffer as well as 1 μL of additive buffer. After gently homogenizing in 96 well plates, mixture droplet was sealed by scotch tape and incubated in dark at 20℃. Precipitant buffers with adding of 4 kinds of additives (Tert-butanol, Formamide, 1, 3-Propanediol and Acetone) were observed with crystals appeared, but no crystal from these conditions got better diffraction resolution result.

Cryo-protectant screening was performed to find proper protectant and concentration after promising crystals were obtained. Common protectants including ethylene glycol, triethylene glycol, glycerol and small molecular weight PEGs (PEG200, PEG300, PEG400 and PEG1000) were tested in different concentration. Crystals were fished out and transferred to 100 μL droplets of the same precipitant buffer using a hand-made loop. Prepared buffers included identical precipitant components at stepped concentration (2%, 4% 6%...until proper final concentration, which was determined by a pre-experiment) of cryoprotectants. Buffer was exchanged by adding 50 μL protectant buffer from an initial concentration (usually 2%), mixing well with buffer containing crystals, and discarding 50 μL buffer to keep total volume stable at around 100 μL. Buffer exchanging was performed every 15-30 min/step, and for final step repeated at least 5 times to make sure crystals were in buffer with identical protectant concentration. **Figure 2-6** presented typical X-ray diffraction patterns of crystals from different cryo-protection conditions. After cryo-protectant buffer exchange, crystals were incubated in dark for 2 hours and shock frozen by liquid nitrogen. Frozen crystals were stored in cryogenic tank filled with liquid nitrogen before X-ray diffraction checking.

2.2.10 X-ray diffraction

The test of X-ray diffraction for all crystals were performed at the SPring-8 (Beamline BL44XU) synchrotron facilities in Koto, Hyogo. Snapshot diffraction tests were performed

at single data collection job mode using an EIGER16M detector and an Al 0.800mm attenuator. The camera position distance was 500 mm, with the exposure time of 0.1 s at a wavelength of 0.90000 Å and 0.1° oscillation step. Diffraction data was collected on beamline BL44XU at SPring-8 using CCD detector MX-300HE (Rayonix) at cryogenic temperature (100K). The on-the-spot and remote access X-ray diffraction tests were also performed at Taiwan Photon Source (TPS, Hsinchu). The spacegroup and unitcell determination based on diffraction snaps were performed using iMosflm[59].

2.3 Results

The SDG centrifugation result and SDS-PAGE result are presented in **Fig. 2-2**. After SDG centrifugation, PSI sample separated into bands of green color (B1, B2 and B3). Each band was checked by SDS-PAGE after extraction from the SDG tube. In general, there was no obvious difference in regard to the protein distribution in the SDS-PAGE gel. In regard to sample yield, B2 with the darkest color also had the highest yield and concentration.

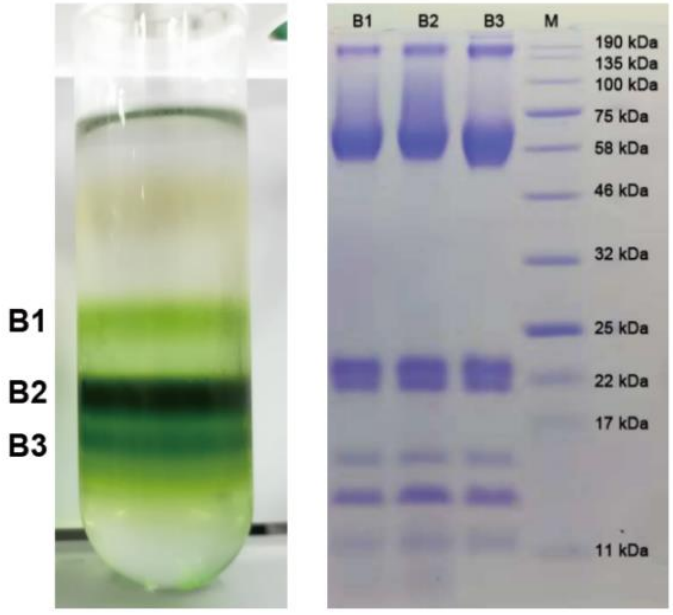

Figure 2-2 Sucrose density gradient (SDG) centrifugation result and SDS-PAGE result for each band extracted from the SDG.

Negative staining grids were prepared for each band with proper sample dilution and applied for EM checking. **Figure 2-3** presents typical micrographs of negative stained grids. Based on SDS-PAGE result as well as molecular size and shape, proteins in B1 were mainly identified as PSI monomers. Whereas proteins in B2 and B3, trimeric shape of PSI could clearly identified, and the diameter of each trefoil-shaped particles was close to that of the PSI trimer. However the characteristics of particle distribution was different between B2 and B3. Based on the results of negative stain transmission electron microscopy, PSI trimer particles in B2 sample tended to be separated and homogeneous, whereas PSI trimer particles in B3 stacked to each other and formed aggregates to some degree. For crystallization, protein sample with high degree of homogeneity is more suitable and accordingly B2 sample was selected for crystallization trials.

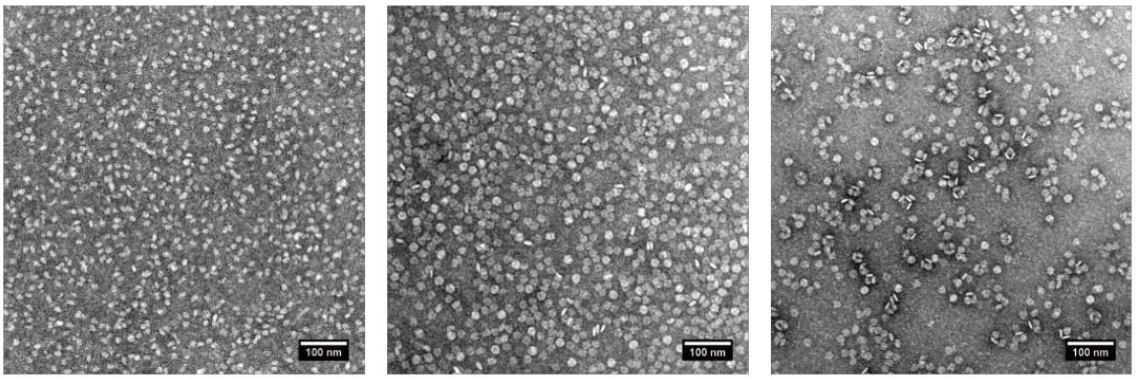

Figure 2-3 Micrographs of negative stained PSI trimer protein samples.

From left to right: B1, B2 and B3 marked in **Fig. 2-2**.

Several crystallization conditions were found possible to crystallize PSI sample buffer extracted from the SDG band B2, which are presented in **Fig. 2-4** with overall view and zoomed-in view of typical crystals and also precipitant buffer conditions. The protein sample formed crystals in various shapes and sizes, indicating multi-arrangements. Some conditions were highly reproducible, whereas some other conditions were just a flash in the pan and no crystals were observed in following optimization trials.

The most promising precipitant buffer condition with best reproducibility and regular-shaped crystals contained ammonium sulfate, sodium chloride, sodium citrate (pH 6.0) and PEG 2000. The following buffer optimization trials were performed mainly by adjusting the concentration and ratio of these chemical components. Meanwhile, various additives and detergents were also tried for potential improvements of crystal formation and X-ray diffraction as described in the Methods part. In addition, micro-seeding by smashing crystals into pieces as potential crystalizing cores, as well as macro-seeding which transits complete crystals into mixture of protein buffer and precipitant buffer were also applied for exploring the possible optimal crystallization strategy. **Figure 2-5** summarized photos of typical results of crystal optimization trials. In general, buffer components being optimized to proper concentration and ratio made most progress, whereas additives including detergent screening gave only limited improvement in crystal formation and diffraction quality. No promising crystals were obtained from seeding trials.

To avoid radiation damage of high-energy X-ray from synchrotron radiation source, crystals should be shock frozen into liquid nitrogen before diffraction measurements. In order to find optimal cryoprotectants type and proper concentration, ice ring test was performed to crystals in different chemicals as described in the Method section. The highest resolution for a distinguishable diffraction spot was around 6.3 Å. **Figure 2-6** presented typical diffraction snaps of crystals in different cryoprotectants, detailed condition and unit cell parameters were summarized in **Table 2-2**.

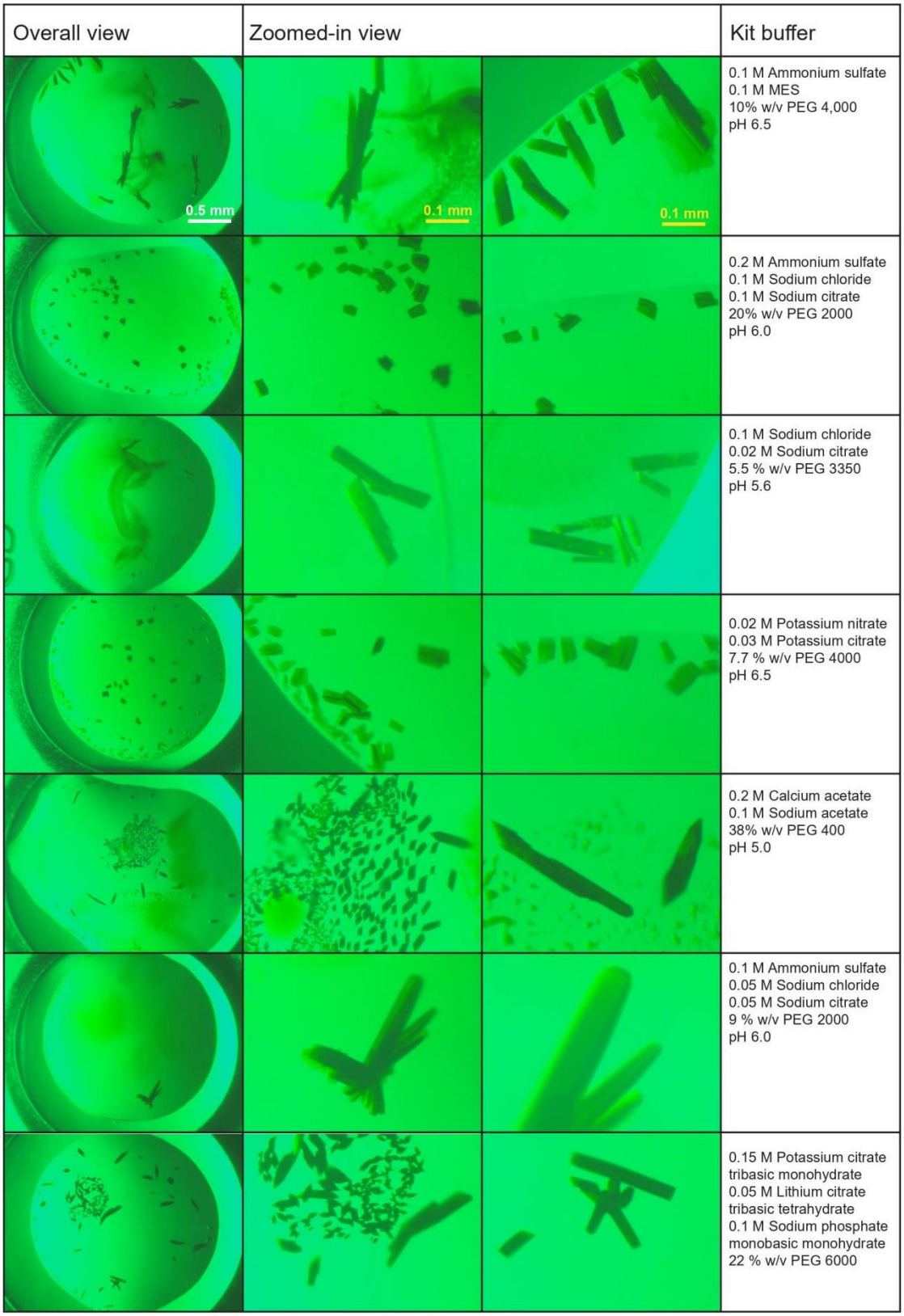

Figure 2-4 Initial crystallization screening results

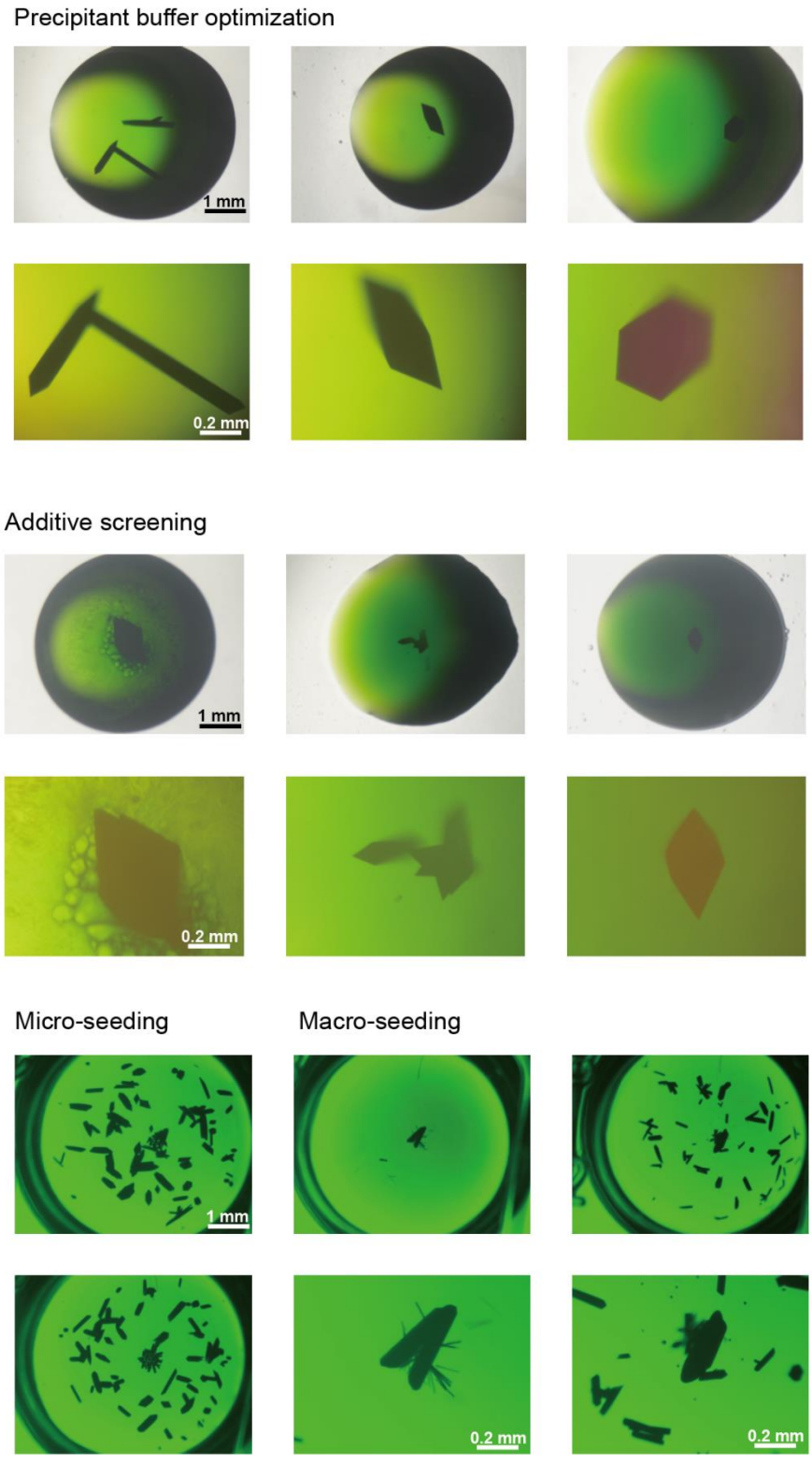

Figure 2-5 Summary of crystallizing optimization trials

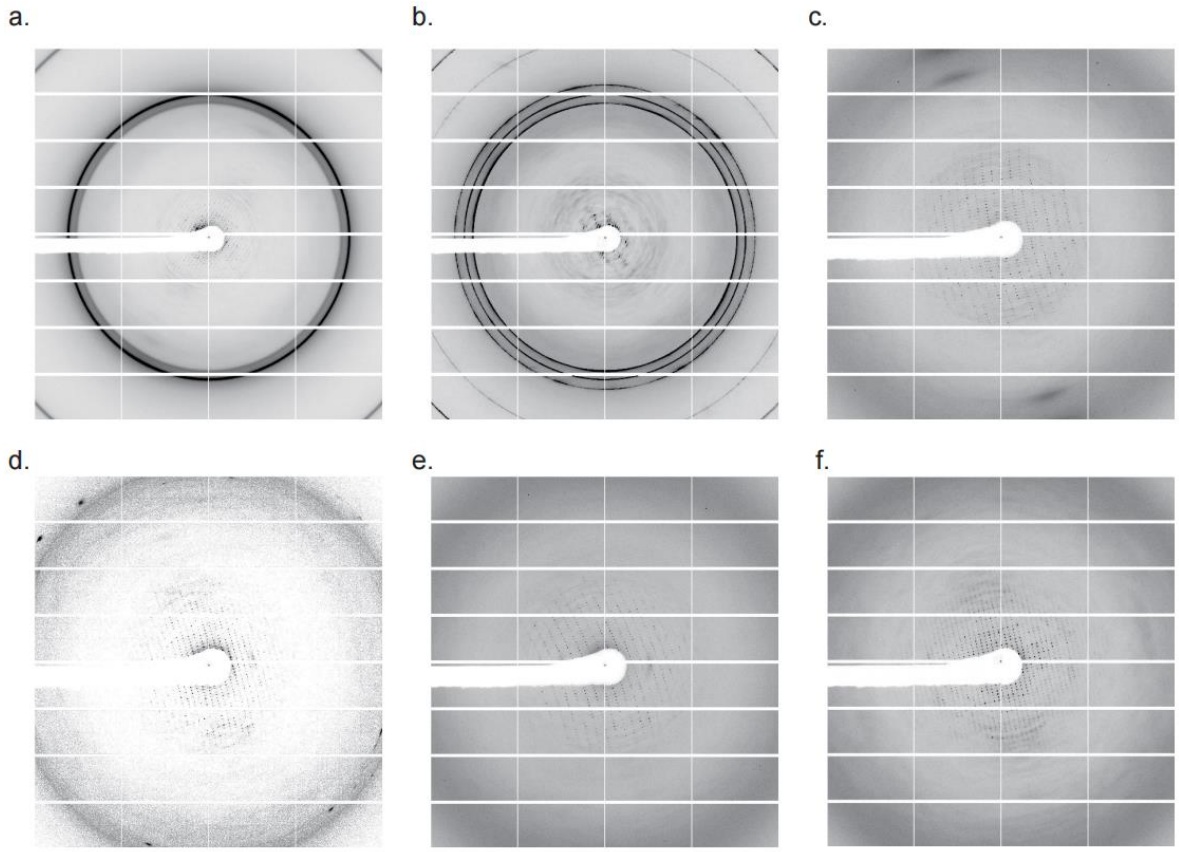

Figure 2-6 Diffraction snaps of crystals in various cryoprotectants

No.	Cryoprotectant	Spacegroup	Mosaicity	*a*	*b*	*c*	*α*	*β*	*γ*
a.	Ethylene glycol	P1	1.40	92.3	144	230	89.9	86.5	81.4
b.	Ethylene glycol	P1	0.30	192.4	523.7	1025	94.4	84.5	98.2
c.	Triethylene glycol	P1	0.55	142.2	255.4	787.9	89.9	90.6	90.0
d.	Glycerol	P1	0.05	124	145.8	191.4	94.1	96.3	99.2
e.	Glycerol	P1	0	80.8	107	232.1	91.8	92.4	99.3
f.	PEG 2000	P1	0.05	95	143.8	225.6	89.9	93.0	93.8

Table 2-2 Diffraction pattern statistics of typical crystals

2.4 Discussion

The cyanobacterial photosynthesis-related protein complex Photosystem I (PSI) genetically modified with a 10x his-tag on the N-terminal of subunit PsaF was purified from thermophilic cyanobacteria *T. elongatus* BP-1 cells at high purity and homogeneity. Crystals were found during the initial screening of crystallizing conditions and optimized through various strategies including seeding, precipitant components, and additive screening. Regular-shaped and large (over 1 mm length) crystals were shock frozen and stocked in liquid nitrogen after exchanging buffer containing proper cryoprotectants. X-ray diffraction by synchrotron radiation source at SPring-8 (Harima) and Taiwan Photon Source (TPS, Hsinchu) was performed for crystal quality checking. Even though efforts were spent for optimization, limited resolution and high anisotropy hindered the high-quality structure determination.

Optimization trials gave some hints of how to optimize the crystallization of huge membrane protein complexes like PSI. In general, the seeding method did not contribute much if the number of crystal cores was reasonable. Sometimes, on the contrary, the seeding method could cause improper crystals growing (such as multi-crystals and crystal branches). Based on current crystallization results, since improper crystallization will obstruct diffraction, the seeding method was only applicable in case of crystal cores were hard to form, and not suitable in PSI trimer crystallization in this case. As for additive (including detergent) screening, since no crystal was detected with a better resolution during following diffraction tests, no obvious beneficial contribution was observed by adding additives into crystallizing mixtures. Until now, optimization of precipitant concentration worked best in the aspect of crystal appearance, and cryoprotectants screening contributed in the aspect of diffraction patterns and protect crystals from shock-frozen by liquid nitrogen. Before precipitant buffer and cryoprotectants optimization, crystals with the best resolution were around 10 Å, and thick black ice rings were observed around the periphery of diffraction pattern (as **Fig. 2-6 a.**). Whereas after optimization, the ice ring was eliminated, and the resolution was also improved to around 6.5 Å (as **Fig. 2-6 e.**). However, current diffraction result, especially in the aspect of

resolution, is still not satisfying for the better atomic model building when compared with previous structures (such as the 2.5 Å PSI trimer crystal structure).

According to the current results of PSI trimer crystallizing trials, some factors could be considered to cause a significant effect on crystal quality, such as:

1). The surface charge of complex, which could be changed in different buffers and precipitants.

2). The ratio of detergent and protein concentration, since empty detergent micelles could hinder regular protein arrangement in crystals.

3). purification methods including thylakoid membrane treatment and concentration strategy (PEG precipitation, ultrafiltration etc.), because harsh treatments could cause damages to flexible subunits such as PsaK.

4). Cryoprotectants and cryoprotection strategy, which could have a remarkable influence on diffraction quality and resolution.

On the other hand, since the purified PSI protein sample was with high purity and homogeneity from the view of negative staining result, it was promising to be utilized in the following Cryo-EM single particle analysis data collection and processing. In the following Chapter 3, purified PSI played its potential in exploring binding mechanism of electron transfer with its partners, and atomic model of PSI in presence of Fd and Cyt c_6 was built based on a high resolution Coulomb potential map.

Chapter III. Cryo-EM single particle analysis of Cyt c_6-PSI-GaFd triple complexes

3.1 Introduction

3.1.1 The photosynthetic electron transport chain in cyanobacteria

Oxygenic photosynthesis can be divided into two phases: the light-dependent reactions and light-independent reactions, the former of which includes photon absorption by PS-internal pigments and drives the photosynthetic electron transport originating from water to the final electron carrier protein, Ferredoxin (Fd). In the reaction center of Photosystem I (PSI), light-driven charge separation takes place at a special pair of one Chlorophyll *a* (Chl *a*) and its isomer Chlorophyll *a'* (Chl a') molecule (termed as P700) using the energy of photon funneled to it by antenna pigments. The activated electron is then transferred through the Electron Transport Chain (ETC) and finally relayed to the downstream soluble electron acceptor proteins at the stromal side. Reduced electron acceptors, as strong natural reductants, provided electrons in a variety of downstream reactions such as the production of NADPH, nitrate assimilation, and fatty acid desaturation[40]. In some cases of iron deficiency, Flavodoxin (Fld) could be expressed by some cyanobacteria for the replacement of Fd, which will be described thoroughly in Chapter 4. The **Fig. 3-1** is a spatial picture presenting the arrangement of ETC-involved protein complexes and major reaction sequences.

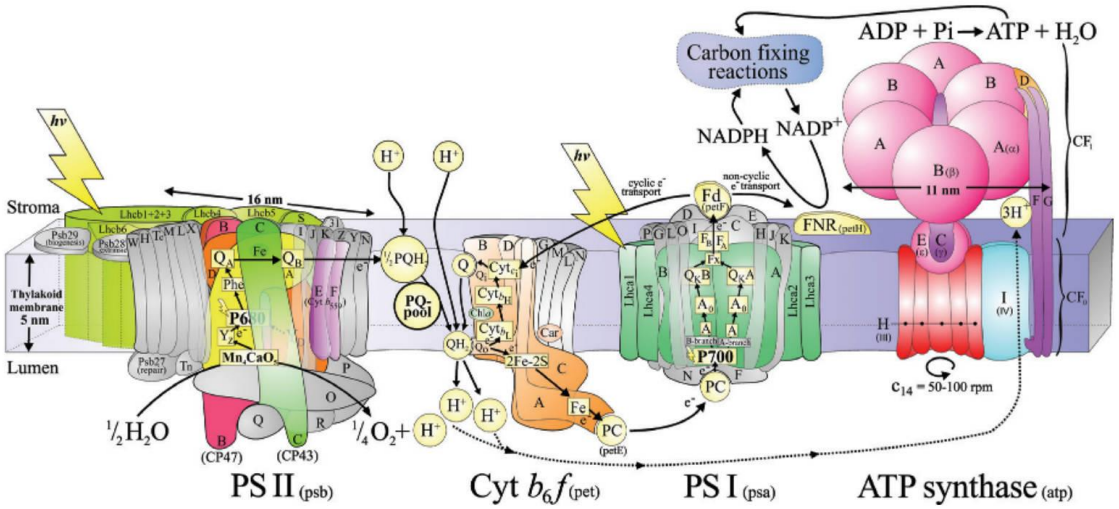

Figure 3-1 The spatial picture showing the major protein complexes and how they are arranged in the photosynthetic membrane[2].

3.1.2 The PSI-related electron transfer partners

Lipophilic and hydrophilic mobile electron carriers, Plastoquinone (PQ), and Plastocyanin (Pc) or Cytochrome c_6 (Cyt c_6) perform an electron relay between the membrane bound complexes of the light reactions[39,60,61]. Two of those electron transferring players in the oxygenic photosynthesis form a transient electron transfer complex and immediately dissociate after passing/receiving an electron[62,63]. These electron transfer events should be sequential, and each electron transfer takes place with the specificity and kinetic competence, which means how to pass an electron is the key in the maximum performance of this electrochemical reaction. The excited P700 (P700*) which lost one electron would be reduced by an electron donor protein at the lumenal side, sequentially launching the next round of electron transfer. Cytochrome c_6 (Cyt c_6, formerly termed Cytochrome *c*-552[64]) and plastocyanin (Pc) function as interchangeable upstream electron donor of PSI, widely distributed in diverse phototrophs from cyanobacteria to higher plants. Cyt c_6 utilizes one iron-contained heme as a redox center, whereas copper plays a similar role in Pc. While the inter-molecular interaction of lipophilic organic molecules, plastoquinone or quinone analogues, between Photosystem

II and Cyt b_6f were characterized relatively well by kinetics or X-ray crystallography[65–67], the protein-protein interaction of electron carrier, Pc or Fd, to Cyt b_6f, PSI or NDH1 are still challenging to be characterized because of their colossal molecular size and redox-dependent structural changes[68]. Among these huge integral membrane proteins interacting with electron carrier proteins, PSI is executing very fast charge separation by absorbing light energy, and the transfer of electrons across the thylakoid membrane[47,69,70].

3.1.3 The evolutionary origin and function of Cyt c_6

The Great Oxidation Event (GOE)[1] caused by oxygenic photosynthesis made an profound impact on the form of element in Earth's biosphere. The bioavailability of iron decreased as the consequence of its oxidative deposition[71]. Most cyanobacteria and green algae expressed both Cyt c_6 and Pc simultaneously, which was regulated by the accessibility of copper[72]. Evidence from *Synechocystis sp.* PCC 6803 indicated such kind of regulation was controlled by protease-mediated mechanism[73]. It is commonly believed that Pc gradually replaced Cyt c_6 as the major photosynthetic electron donor of PSI during the evolution from cyanobacteria to higher plants[39].

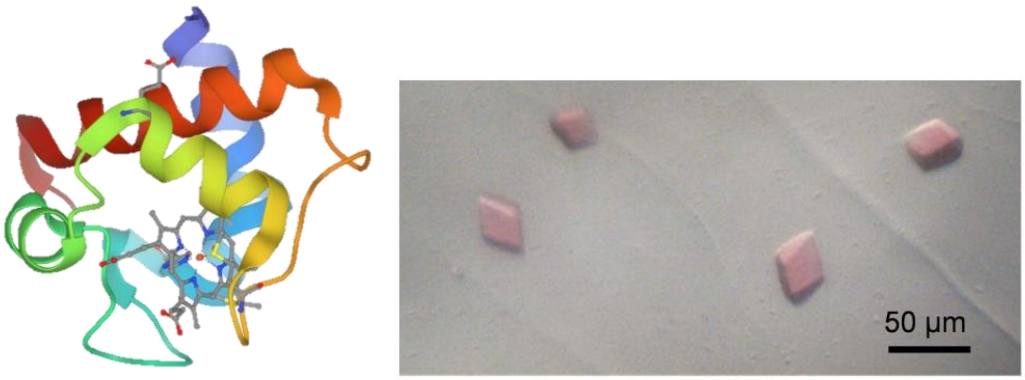

Figure 3-2 Structure of native Cyt c_6 from *Thermosynechococcus elongatus* BP-1 and the crystal obtained by vapour-diffusion crystallization[74] (PDB ID: 6TR1).

The thermophilic cyanobacteria *Thermosynechococcus elongatus* BP-1 was initially isolated from a hot spring in Beppu, Japan. As an ancestral photoautotroph, no Pc-synthesis gene was found in its genome[75], indicating Cyt c_6 functioned as the only PSI electron donor in this cyanobacterium. Meanwhile, Pc is the electron donor in higher plants[76] although Cyt c_6-like gene existed[77]. From this aspect, the electron transfer from Cyt c_6 to PSI may have played an indispensable role in the primordial photosynthesis. The Cyt c_6 seemed to be endowed with other functions during evolution, whereas the electron transfer role was gradually undertaken by Pc[78].

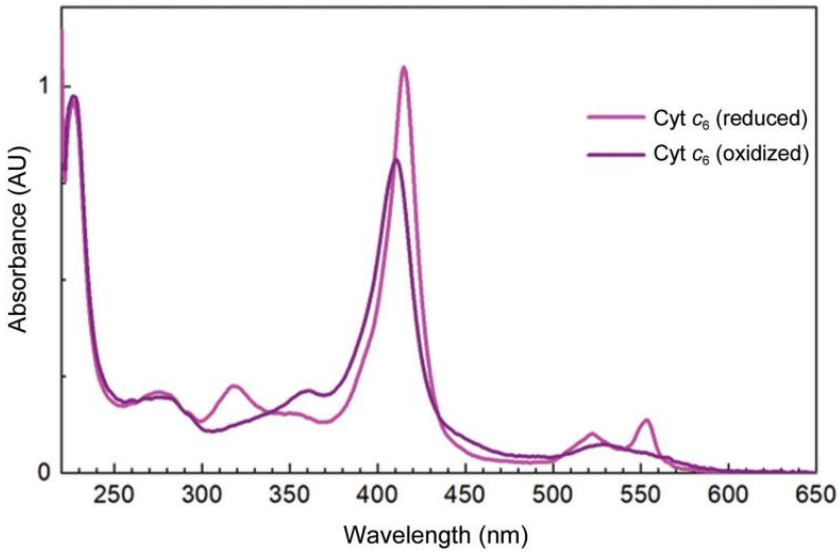

Figure 3-3 Absorbance properties of Cyt c_6 from *Thermosynechococcus elongatus* BP-1 characterized by UV–Vis absorbance spectroscopy[74].

3.1.4 The Fd and Gallium-substitution of its redox center

Ferredoxin serves as an electron acceptor and uses [2Fe-2S] cluster as its redox center. Flash-absorption spectroscopy of Fd reduction by PSI revealed kinetic complexity of this reaction with several phases of intra-complex electron transfer[79]. Since the diamagnetic nature of the [2Fe-2S] cluster complicates structure determination using nuclear magnetic resonance (NMR), Gallium-substituted Ferredoxin (GaFd, see **Fig. 3-4**),

whose [2Fe-2S] cluster was replaced by [2Ga-2S], was applied in the NMR study of its interaction between PSI and Ferredoxin $NADP^+$ oxidoreductase (FNR)[80] . In addition, because [2Ga-2S] is redox inactive and cannot be reduced as a normal redox center, GaFd was also exploited as a tool in the investigation of binding effects to PSI with the disability of reduction[81]. The GaFd has almost identical structural features when compared with native Fd, however, its binding affinity to PSI is much stronger than that of native Fd[82].

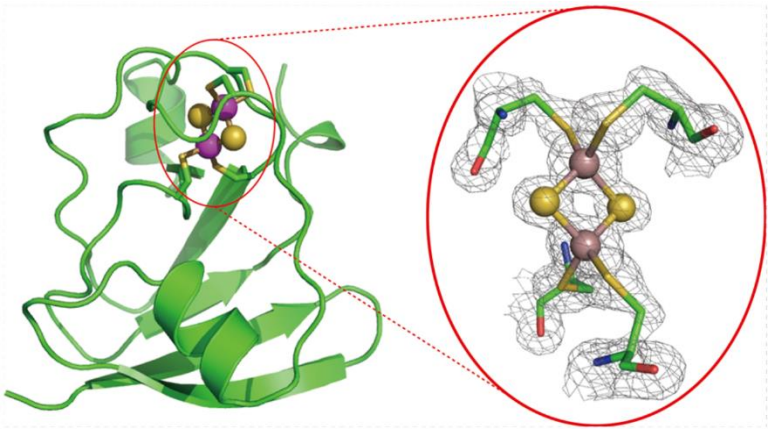

Figure 3-4 Structure of Ga-substituted Ferredoxin (PDB ID: 5auk) and the zoom-in view of its [2Ga-2S] redox center[80].

3.1.5 Progress of PSI-related electron transfer complex structure determination

To advance our understanding of the PSI-related transmembrane electron transfer mechanism, various methods such as co-crystallization[82] as well as chemical cross-linking[68] were applied to PSI with its electron transfer partner(s). A transiently formed noncovalent electron transfer complex of photosynthesis, Fd:PSI, was first crystallized in 2002. Perhaps because the crystals reported in 2002 were of low quality or not reproducible, the first X-ray structure of Fd:PSI was independently solved at 4.2 Å resolution in 2018[82], which confirmed Fd-binding sites on PSI previously suggested by site-directed mutagenesis and kinetic analysis[49,83–86]. In that report, redox inert GaFd,

whose 3D structure is identical except that the [2Fe-2S] cluster is replaced to [2Ga-2S], was used to fix the redox state of bound Fd to the oxidized state even under the light[81].

After Cryo-EM became common around 2014, several noncovalent electron transfer complex structures of PSI started to be reported, such as PSI:Fd (PDB ID: 7S3D[46]), PSI-IsiA additional antenna complex with Flavodoxin (PDB ID: 6KIF[87]), PSI-LHCI-LHCII (PDB ID: 7D0J[88]) and the triple complex of Pc:PSI-LHCI:Fd (PDB ID: 6YEZ[89]). In most cases, however, low local resolution of bound mobile carrier protein prevented detailed discussion at the residue level. This is rather disappointing and thus far the only exception to this situation is the analysis of the Pc:PSI-LHCI complex at 2.74 Å (PDB ID: 6ZOO[90]) which provides first more detailed structural insights into the interaction of the electron donor Pc at the luminal docking side of PSI.

3.1.6 Research motivation and target

To understand the redox-dependent protein-protein interaction around PSI more clearly, higher resolution structure of PSI together with its electron donor and acceptor under the determined redox state is required. In this chapter, we describe the Cryo-EM single particle analysis results of cyanobacterial PSI from *Thermosynechococcus elongatus* BP-1 at overall 1.97 Å resolution complexed with its electron transfer partner proteins GaFd and Cyt c_6. Supplemented by the Isothermal Titration Calorimetry (ITC) measurement, the structural basis for transient but highly specific molecular interactions is described and discussed. In addition, the detailed redox-dependent electron transfer mechanism around PSI is proposed.

3.2 Materials and Methods

3.2.1 Optimized PSI trimer purification

The PSI purification protocol is similar as described in Chapter 2 with some minor modifications. Thermophilic cyanobacteria of the *Thermosynechococcus elongatus* BP-1

mutant strain, genetically modified with an N-terminal His_{10}-tag on the PsaF subunit as well as a chloramphenicol-resistant gene as a selectable marker, were cultured under illumination for the purification of both PSI trimer and Cyt c_6. Cultivation was performed under continuous illumination at 30 μM photons m^{-2} s^{-1} at 50℃ in BG11 medium as described previously[91]. A total of 16 L culture was harvested when the OD_{730nm} absorbance reached one. His-tagged PSI trimers were purified from thylakoid membranes according to Kubota *et al.*[92].

Harvested cells were concentrated by centrifugation (8,000 g, 2 min at 4℃, JLA 9.1000 rotor, Avanti™ HP-26XP), re-suspended in Buffer A containing 50 mM MES (pH 6.5), 25% glycerol, 20 mM $CaCl_2$ and 20 mM $MgCl_2$, then frozen for storage at -80℃ or used immediately for cell disruption as previously described[93]. Cells were disrupted in freshly prepared pre-cooled Buffer B (same components as in Buffer A with the addition of 1 mM benzamidine, 1 mM 6-aminohexanoic acid, 1 mM PMSF solubilized in ethanol, and 1 mM DNase I) and thylakoid membranes were separated from soluble cellular contents by ultracentrifugation (40,000 g, 30 min at 4℃, P50AT2 rotor, HITACHI himac CP80WX).

Thylakoid membranes were re-suspended in Buffer A at a chlorophyll concentration of 1 mg/mL, and subsequently a 10% n-dodecyl-β-D-maltoside (β-DDM) stock solution was added dropwise until the concentration of β-DDM reached 1%. Then the mixture was incubated in the dark at 4℃ with gentle stirring for 45 min. After membrane solubilization, insoluble contents were removed by ultracentrifugation (50,000 g, 30 min at 4℃, P50AT2 rotor, HITACHI himac CP80WX) . The supernatant was applied for Immobilized Metal Affinity Chromatography (IMAC) to an open column with Ni-NTA Sepharose (Qiagen). PSI trimers were eluted from the column using Buffer C containing 20 mM MES (pH 6.5), 20 mM $CaCl_2$, 20 mM $MgCl_2$, 0.05% β-DDM and 100 mM imidazole. Eluted PSI trimers were concentrated by ultrafiltration at 3,000 g, 4℃ (Amicon15 ultrafiltration tubes, 100 kDa MWCO) to a final chlorophyll concentration of around 10 mg/mL.

The GraDeR[94] approach was applied for exchanging the detergent to glyco-diosgenin (GDN) and the removal of excess free detergent: a sucrose step gradient was prepared with sucrose concentrations of 1.7 M, 1.3 M, 0.9 M, 0.5 M and 0.1 M from bottom to top, and GDN of 0.1%, 0.05%, 0.03% 0.01% and 0.005% from bottom-to-top. After sucrose density gradient centrifugation (25,000 g, 20 hours at 4℃, P28S rotor, HITACHI himac CP80WX), PSI trimers from the corresponding band were collected, and a desalting column (PD-10, GE Healthcare) was used for sucrose removal and buffer exchange. Final PSI trimers were concentrated to a chlorophyll concentration of 10 mg/mL in buffer D (10 mM Tricine, pH 8.0, 10 mM $MgCl_2$ and 0.005% GDN) and examined for purity, stability and monodispersity using SDS-PAGE and negative stain electron microscopy. Final PSI trimer sample was shock frozen in liquid nitrogen in 10 µL aliquots using photophobic EP tubes and stored until further use at -80℃. Protein concentration of PSI trimer was determined based on chlorophyll content ratio of C_{Pro}/C_{Chl} =3.92. The **Fig. 3-5a** showed sucrose density gradient result of PSI and red arrow indicated the PSI trimer accordingly.

3.2.2 Negative stain EM

Protein sample quality were assessed by negative staining. An aliquot of 3.5 µL final sample was diluted 1/100 and applied to glow-discharged (5 mA, 10 s, Eiko) continuous carbon film coated copper grids (Nisshin EM). Staining was performed by applying 3.5 µL 2% uranyl acetate solution. After incubation for 30 s, staining solution was blotted by filter paper (Whatman #1) and dried at room temperature. EM grids were inspected using a H-7650 HITACHI transmission electron microscope at 80 kV acceleration voltage equipped with a 1 x 1 K Tietz FastScan-F114 CCD camera. A typical PSI trimer negative staining EM micrograph is presented in **Fig. 3-5b**.

3.2.3 Cyt c_6 purification

Supernatant obtained by disruption of *T. elongatus* BP-1 cells and ultracentrifugation as described above was utilized for the isolation of Cyt c_6 based on previous purification method[95] with some modifications. Ammonium Sulfate (AS) powder was added gradually at 25 ℃ to the supernatant until saturation reached 45% and after magnetic stirring for 45 min at 25 ℃ precipitates were removed by centrifugation (9,500 g, 30 min at 25 ℃, JLA 9.1000 rotor, Avanti™ HP-26XP). The resulting supernatant was loaded onto a hydrophobic interaction chromatography column (HiTrap® Phenyl HP) pre-equilibrated with buffer containing 10 mM Tricine (pH 7.5) and 45% AS by Fast Protein Liquid Chromatography (FPLC, ÄKTA explorer). Fractions containing Cyt c_6 were eluted by decreasing the AS concentration to around 20%. After column mediated desalting (PD-10, GE Healthcare), fractions were exchanged to a buffer containing 10 mM Tricine (pH 7.5) and 10 mM NaCl, and loaded onto an anion exchange column (HiTrap® Q HP) pre-equilibrated with the same buffer. Fractions exhibiting pink color were eluted by increasing the NaCl concentration to around 100 mM, pooled and polished by a final gel filtration step (Superose® 75 16/60) using a running buffer containing 30 mM Tricine (pH 8.0) and 10 mM $MgCl_2$. Sample quality and redox state was assessed by measuring the OD_{553nm}/OD_{273nm} absorbance ratio based on a previously published protocol[96] and absorbance properties were characterized by UV–Vis absorbance spectroscopy. The deep pink color and characteristic absorption peak at 553 nm verified the reduced state of purified Cyt c_6 when compared with previous spectroscopic results[74] of reduced Cyt c_6. SDS-PAGE analysis of the sample is presented in **Fig. 3-5c**.

3.2.4 Ferredoxin purification and preparation of Gallium-Substituted Ferredoxin

A DNA fragment encoding native *T. elongatus* BP-1 Ferredoxin (Fd) was cloned into the *p*ET28a vector (Novagen) using NcoI−BamHI restriction sites, and expressed using the *E. coli* strain BL21-(DE3) using a Luria-Bertani (LB) medium. Purification of Fd and the

subsequent substitution of its native [2Fe-2S] cluster with the redox inert [2Ga-2S] cluster were performed as previously described[80]. In brief, cells were harvested by centrifugation, re-suspended in a buffer containing 50 mM Tris (pH 7.5) and 10% glycerol. After cell disruption by sonication resulting lysates were centrifuged for 30 min at 45,000 rpm, 4 ˚C (P45AT rotor, Hitachi CP80WX) and the resulting supernatant loaded onto anion exchange cellulose column (DE52, Whatman). Red-colored fractions containing Fd were eluted using a buffer containing 50 mM Tris (pH 7.5) and 500 mM NaCl and dialyzed over night at 4℃ against 3 L of buffer containing 50 mM Tris (pH 7.5) and 50 mM NaCl. The dialysate was then applied to a HiTrap Q HP column (GE Healthcare) in buffer containing 50 mM Tris (pH7.5), and eluted using a linear NaCl gradient (0 - 1 M NaCl). Subsequently, for ammonium sulfate precipitation a 100% saturated AS buffer (50 mM Tris (pH 7.5) was added 1:1 to the pooled fractions, the precipitate spun down (8,000 g, TOMY) and was discarded. Phenyl Sepharose column (GE Healthcare) was used for purity polishing with buffer A containing 50 mM Tris (pH 7.5) and 40 % saturated ammonium sulfate, and buffer B containing 50 mM Tris (pH 7.5). Elution was performed using a linear gradient of 0 - 100 % buffer B with red fractions being collected.

For Gallium substitution, total 45 mg of Fd were denatured by adding hydrogen chloride (HCl) at concentration of 6 M to a final concentration of 1 M HCl. The turbid solution was pelleted (10 min, 10,000 g at R.T., TOMY's centrifuge machine) and the white precipitate was immediately rinsed with Milli-Q water, followed by resuspension in a buffer containing 100 mM Tris (pH 8.0). The above steps were repeated twice to ensure removal of all iron atoms from Fd. The final protein precipitate was re-suspended in a buffer containing 100 mM Tris (pH 8.0), 6 M guanidine hydrochloride and 10 mM dithiothreitol in an anaerobic tent.

The denatured Fd was refolded at 4℃ by diluting it into a refolding buffer (2 mM $GaCl_3$, 2 mM Na_2S, 2 mM DTT, and 20 mM Tris, pH 8.0), and incubated at 4 °C overnight under anaerobic conditions. Refolded GaFd was purified via HiTrap-Q column (GE Healthcare)

chromatography using an elution gradient from 0 to 1 M NaCl in 20 mM Tris-HCl (pH 7.5). Elution profiles of the proteins were monitored by absorbance at 280 nm, eluted fractions collected and concentrated by ultrafiltration using 10 kDa cut off Amicon Ultra-15, using swing rotor (2,000 g, 4 ˚C) before loading onto a Superdex 75 16/60 column (GE Healthcare), flow rate 0.5 ml/min pre-equilibrate with 100 mM Tris (pH8.0). Fractions containing GaFd were detected by 280 nm absorbance for final polishing by size exclusion chromatography. The concentration of native Fd and GaFd were calculated using their respective molar extinction coefficient of ε_{422} = 9.68 mM^{-1} cm^{-1}, and ε_{280} = 170.2 mM^{-1} cm^{-1} as described before[80]. Purity of GaFd was monitored using SDS-PAGE as shown in **Fig. 3-5d**.

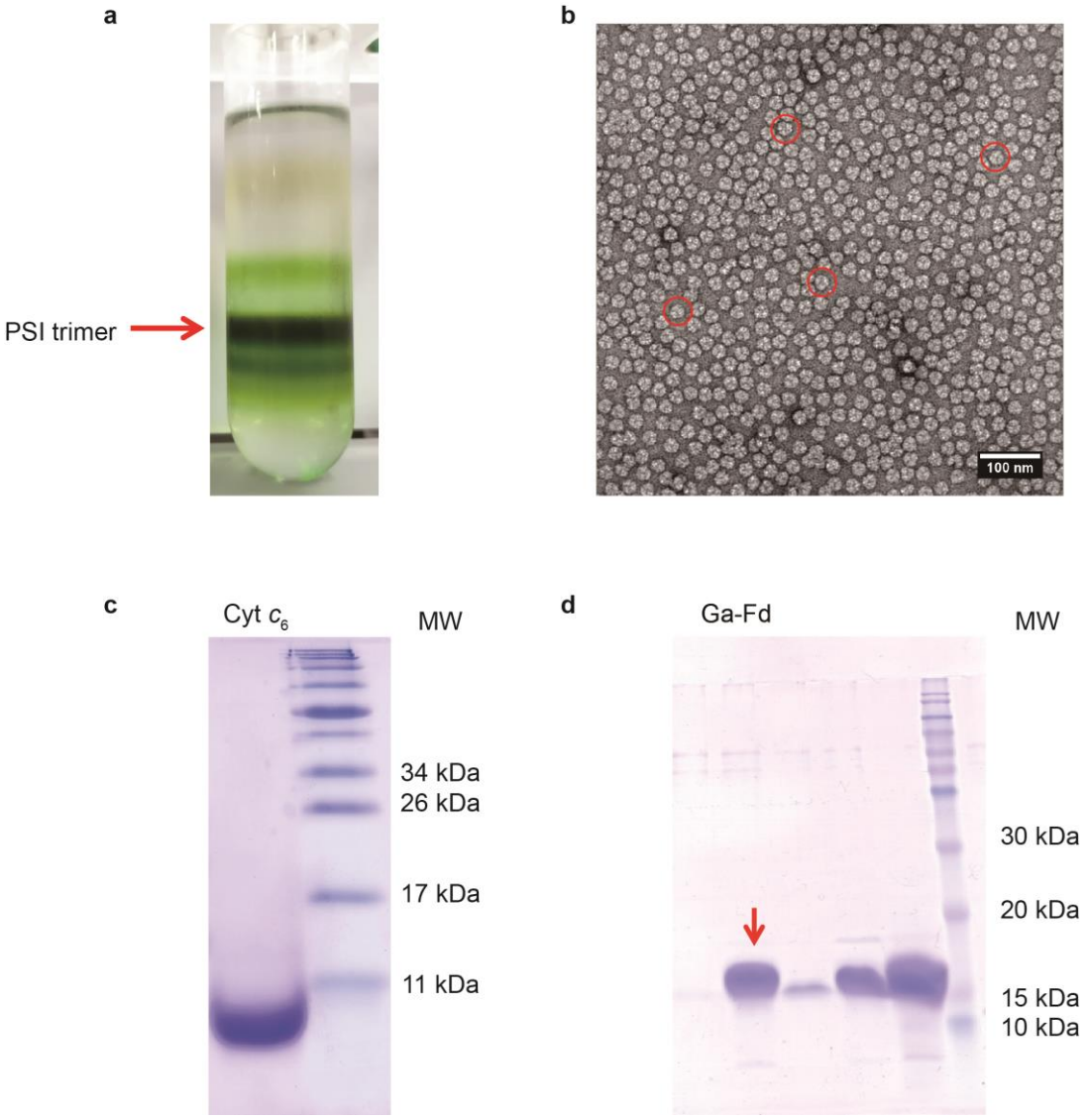

Figure 3-5 Purification results of PSI trimers, Cyt c_6 and Ga-substituted Fd.

3.2.5 ITC measurement

The ITC measurements were performed as a cooperation with Prof. Young-ho Lee lab at Korea Basic Science Institute (KBSI, Korea). All ITC measurements were performed with a MicroCal PEAQ-ITC instrument (Malvern Panalytical, UK) at 25℃. The concentrations of GaFd in the syringe and PSI trimer in the cell were 600 μM and 11 μM, respectively. All protein solutions were subjected to buffer exchange into 30 mM

Tricine-NaOH buffer (pH 8.0) containing 10 mM $MgCl_2$, 50 mM NaCl and 0.005% GDN by using PD-10 columns (GE Healthcare Life Sciences), and air bubbles were removed by centrifugation for 5 min at 10,000 g prior to ITC. The following ITC parameters were used: titration, 19 injections; initial delay, 60 s; spacing time, 150 s; reference power, 10 µcal; and stirring speed, 500 rpm. The injection volume was 0.4 µL for the first injection and 2 µL for the remaining injections. The heat of dilution was measured by titrating 800 µM GaFd in the syringe into a sample cell filled with buffer alone. The heat flow and binding isotherm were calculated by subtracting the heat of dilution. The data were fitted to the one-site binding model in MicroCal PEAQ-ITC analysis software.

3.2.6 Cryo-grid preparation

A total 10 µL purified PSI trimer at a protein concentration of 37 µM (40 mg/mL), 1 µL of purified GaFd in concentration of 400 µM (4.4 mg/mL) and 2 µL of purified Cyt c_6 in concentration of 75 µM (0.75 mg/mL) were mixed together on ice at a final concentration of 30 mg/mL PSI trimer. After incubation on ice in the dark for two hours, an aliquot of 2.6 µL was applied to a glow-discharged (JEC-3000 FC, 30 s, carbon support film facing up) Quantifoil cryo-EM grid (R 1.2/1.3 Cu 300 mesh) and plunge frozen in liquid ethane using a Vitrobot Mark IV (Thermo Fisher Scientific) fitted with Whatman #1 filter paper for blotting at 4 ℃ and 100% humidity for 3.5 s at blot force 0. Frozen grids were transferred to liquid nitrogen for storage, and screening was performed using a Talos Arctica (Thermo Fisher Scientific) transmission cryo electron microscope operated at 200 kV. Cryo-grids exhibiting appropriate particle distribution and ice thickness were taken out of the Talos Arctica and further used for high resolution data collection.

3.2.7 Cryo-EM image data collection

Using the auto-grid adapter cartridge (JEOL), a single pre-screened cryo-grid clipped as an auto-grid (Thermo Fisher Scientific) was transferred to a CRYO ARM 300

(JEOL) transmission cryo electron microscope operated at 300 kV equipped with a cold-field emission gun and an in-column Ω filter. Image acquisition was performed using flood beam parallel illumination in bright field imaging mode. Movies were automatically recorded by SerialEM using image shift (5x5 holes per stage position) using a K3 Summit detector (Gatan, AMETEK) in CDS mode at a nominal magnification of 60,000× at the camera level, corresponding to a pixel size of 0.806 Å with 48 frames in 3 s exposure time, resulting in a total dose of 48 $e^{-}/Å^{2}$. A total of 3,018 movies were collected in series within a defocus range of -0.5 μm to -1.5 μm. Typical micrograph with sufficient quality for data processing and density map construction was represented in **Fig. 3-6b**, whose Fourier transform with Thon rings extending to 2.0 Å resolution was presented in **Fig. 3-6c**. Detailed Cryo-EM data collection, refinement and validation statistics are listed in the **Table 3-1**.

EMDB: 31605 PDB: 7FIX EMPIAR: 10928	
Data Collection and Processing	
Microscope	JEOL CRYOARM 300 (300 kV)
Camera	Gatan K3 Bioquantum
Defocus range (μm)	0.5-1.5
Electron dose (frame/total) (e^{-}/Å^2)	1 / 48
Pixel size (Å)	0.806
Exposure time (s)	3
Micrographs (initial/final)	3,018 / 1,959
Magnification	×60,000
Particles (initial/final)	367,967 / 207,142
Symmetry imposed	C1 / C3
Map Sharpening B-factor (Å^2)	-45.9257 (C1) / -38.073 (C3)
FSC threshold	0.143
Map resolution (Å)	2.06 (C1) / 1.97 (C3)
Refinement	
Initial model used (PDB code)	1JB0 (PSI), 5AUI (Fd)
R.M.S.D. (bonds (Å)/angles (°))	0.01 / 1.059
Clash score	6
Ramachandran outliers	0
Rotamer outliers	0
Sidechain outliers	0
Cβ outliers	0
MolProbity score	1.33

Table 3-1 Cryo-EM data collection, refinement and validation statistics.

3.2.8 Cryo-EM image processing

All image processing was performed using RELION 3.1[97] and UCSF CHIMERA[98] on a local GPU workstation equipped with two GPUs (see **Fig. 3-6a** for the workflow). Total 3,018 movies were divided into six groups, and dose-weighted motion-correction was

performed by implemented MotionCor2[99] algorithm. For each motion corrected micrograph the contrast transfer function (CTF) was estimated using CTFFIND4[100].

For *de novo* building of an initial model, total 40,483 particles were picked automatically from one group of 500 micrographs using the Laplacian of Gaussian. Picked particles were subjected to one round of reference-free 2D classification and the initial model was calculated using 30,580 particles of the best 2D classes. The **Fig. 3-6e** presented an isosurface visualization of the initial model at thresholds. Auto-picking on micrographs of all six groups was performed by using the initial model as a 3D reference. A total of 511,737 particles were picked from all micrographs and 2D classification was performed on the particles picked from each group of micrograph. The 2D classes with clear background and clear protein appearance (as shown in **Fig. 3-6d**) containing a total of 366,174 particles were selected and used for the 3D classification. Particles of the best 3D class, indicated by a red caption in **Fig. 3-6f** representing 56.6% (207,142 particles) of all particles were selected for an initial reconstruction using standard auto-refinement. Subsequently, several rounds of CTF refinement and Bayesian polishing were performed until the overall map resolution did not improve further.

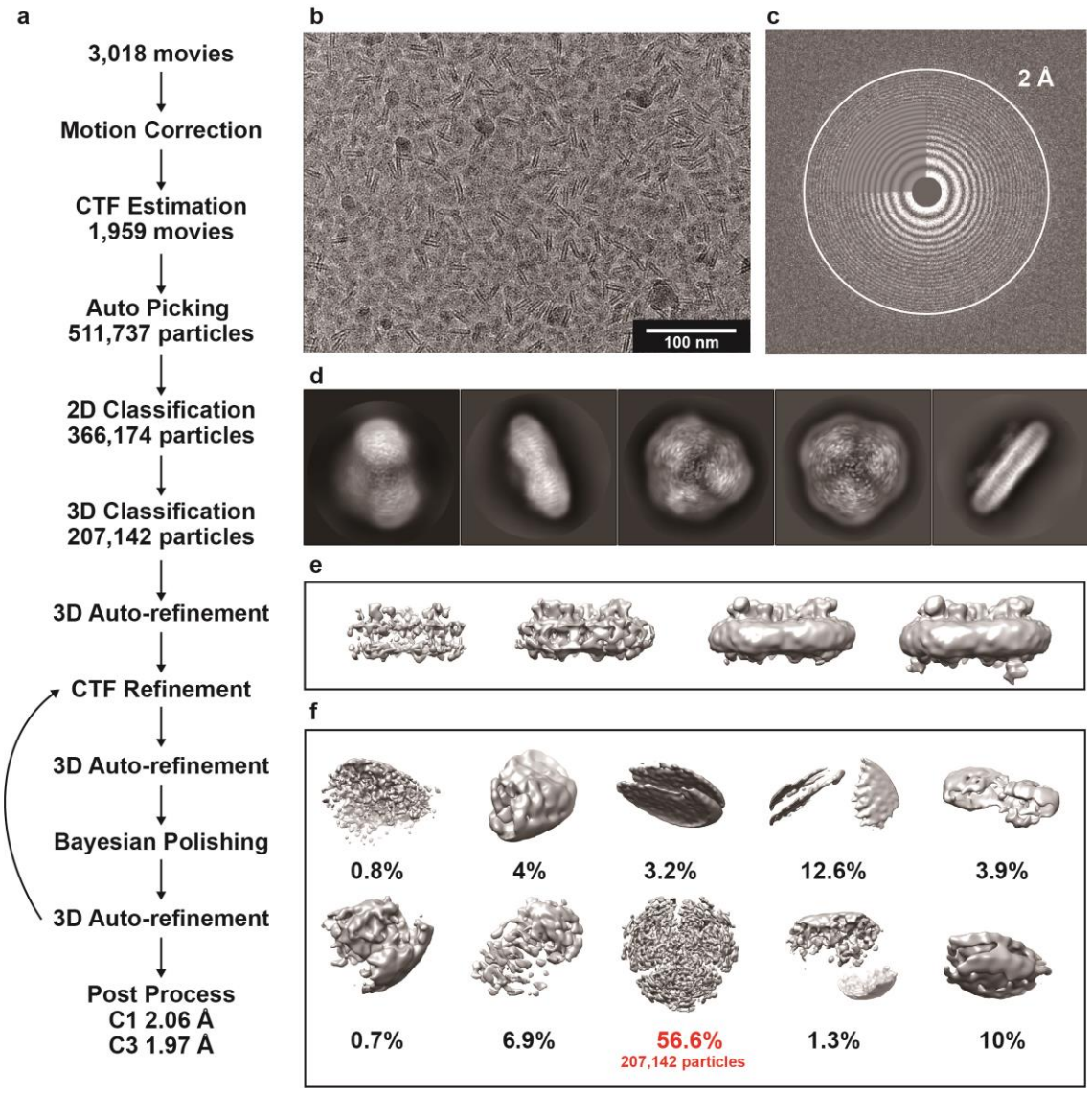

Figure 3-6 Cryo-EM single particle analysis and data processing results. a. The workflow of data processing was performed in RELION 3.1. b. A representative micrograph and c. its Fourier transform with Thon rings extending to 2.0 Å resolution. d. 2D classes selected for further 3D classification. e. Initial *de novo* model based on auto-picked particles rendered at four different thresholds. f. The results of 3D classification. Particles in the best class (colored in red) were used for 3D refinement.

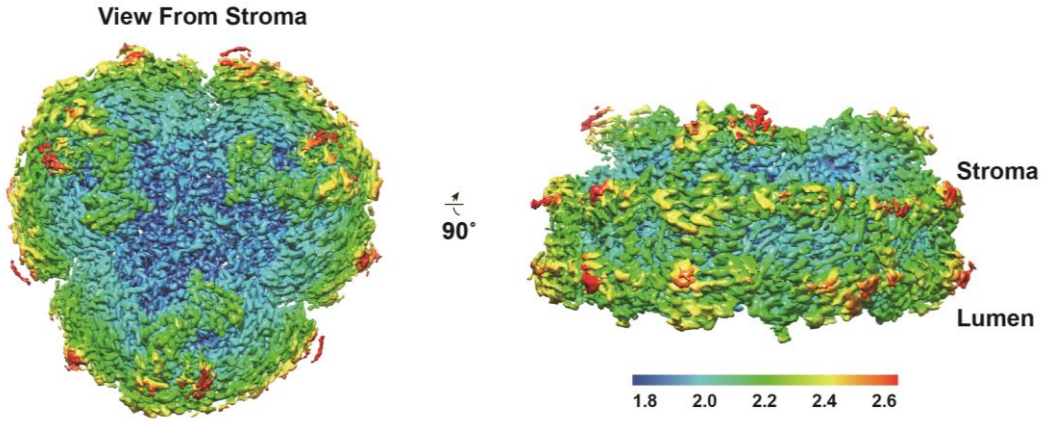

Figure 3-7 Local resolution distribution of post-processed density map in C3 symmetry.

3.2.9 Movie artificial screening

After initial trials of data processing, the movies with low auto-picking hits (<30 particles) and problematic Thong ring as well as low estimated resolution (>5 Å) were omitted (as shown in **Fig. 3-9, 3-10** and **3-11**). The remaining 1,959 movies were applied for the following processing, which resulted in a better overall resolution statistics in post-processing step.

Following standard post-processing procedures, the final map gave an estimated resolution of 2.06 Å without symmetry applied (C1) and 1.97 Å with symmetry applied (C3). No obvious difference could be observed between the C1 and C3 maps in terms of structural features. The C3 symmetrized map was used for the following model building with the reason of better Euler angle distribution and reduced level of noise. Local resolution distribution was calculated using RELION, and results were shown in **Fig. 3-7**. The FSC curves and Euler angle distribution (both C1 and C3 map) of post-processed density map were presented in **Fig. 3-8**. In the map in C3 symmetry presented density bias of each protein, the density of PSI was with highest level, following with GaFd, and the density of Cyt c_6 was most invisible and in lowest resolution as shown in **Fig. 3-12**.

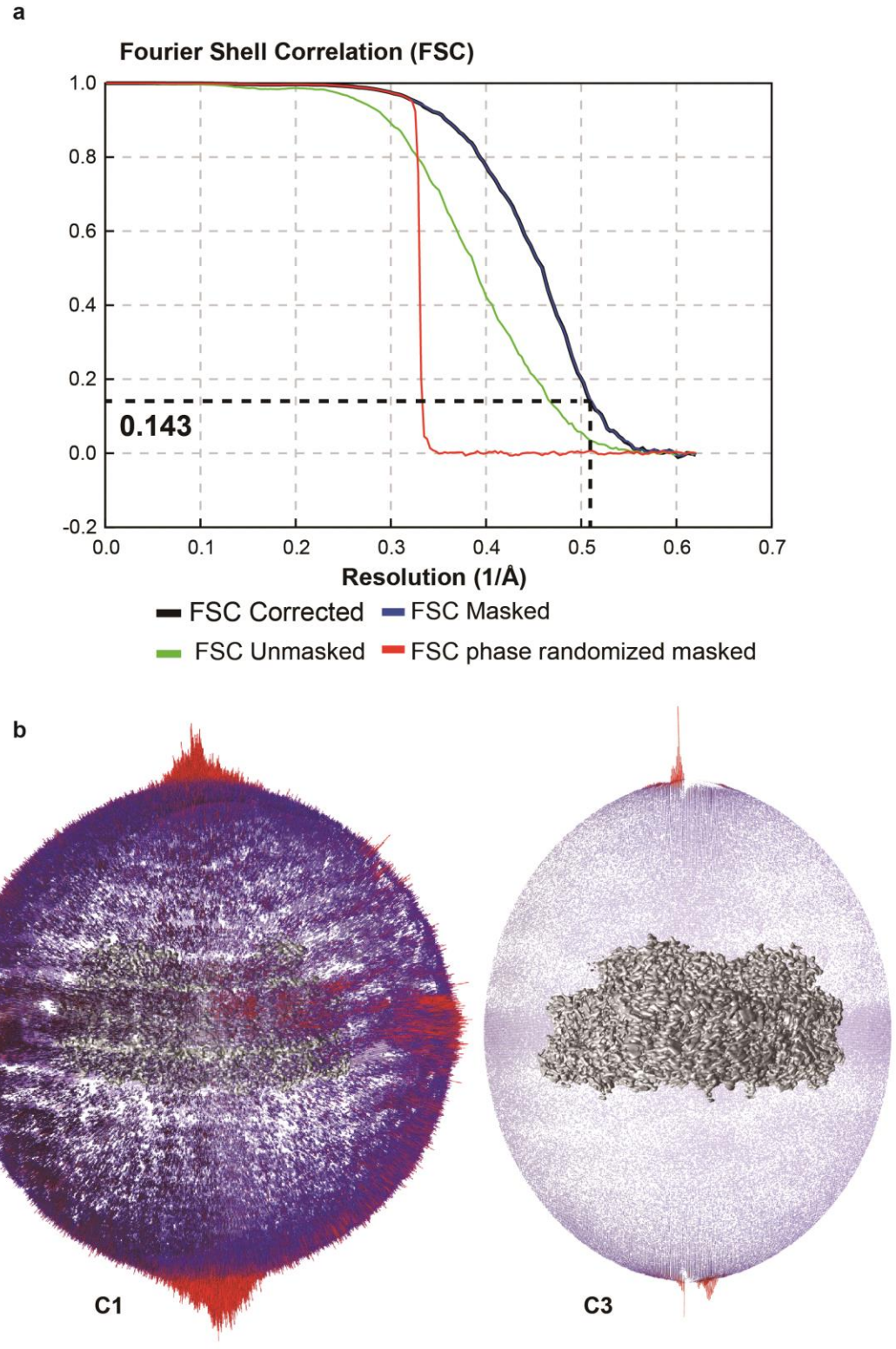
a
Fourier Shell Correlation (FSC)
1.0
0.8
0.6
0.4
0.2
0.0
-0.2
0.143
0.0
0.1
0.2
0.3
0.4
0.5
0.6
0.7
Resolution (1/Å)
FSC Corrected
FSC Masked
FSC Unmasked
FSC phase randomized masked
b
C1
C3

Figure 3-8 The FSC curves and Euler angle distribution**. a.** The Gold Standard Fourier Shell Correlation (FSC) curves as implemented in RELION 3.1 for the post-processing results of the final map in C3 symmetry. The overall resolution of the masked density map was determined as 1.97 Å at 0.143 Gold Standard FSC cut-off. **b.** The Euler angle distribution of the final cryo-EM maps in C1 (left) and C3 (right) symmetry.

3.2.10 Masked 3D classification and auto-refinement

After first round of data processing, the density maps in both C1 and C3 symmetry were applied for local masked 3D classification and following auto-refinements at the binding site of GaFd and Cyt c_6, respectively (See **Fig. 3-12** and **Fig. 3-13**). All the binding areas were extracted by the "segment map" tool (Segger v1.9.5) in UCSF Chimera 1.13.1 at the binding areas of the density map accordingly, and masks of these areas were made by "Mask creation" command in RELION with default parameters. Masked 3D classification and auto-refinement results were presented in the Results part of this chapter with all parameters attached in the following form.

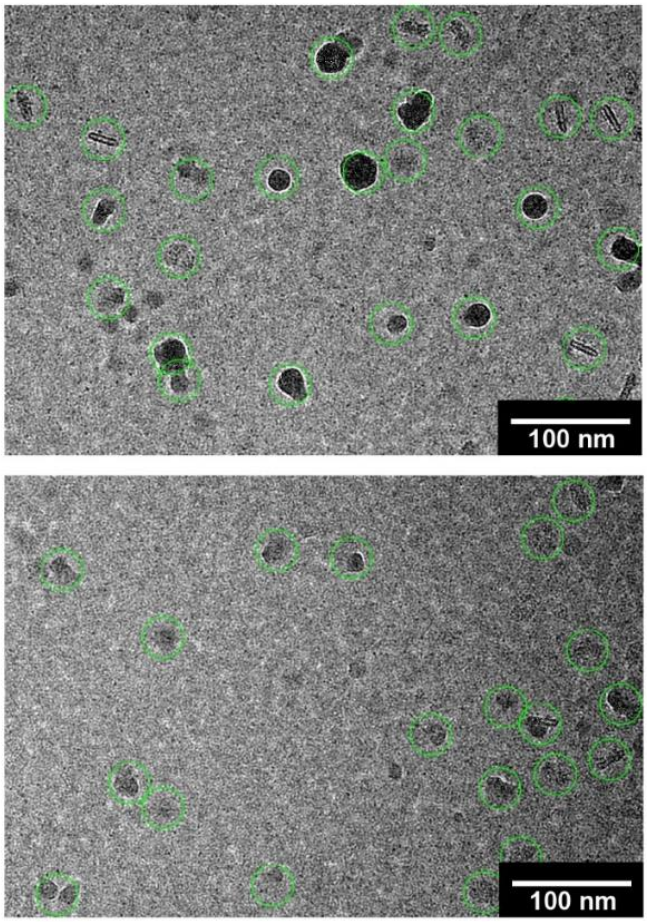

Figure 3-9 Typical movies which were omitted after CTF estimation for the reason of limited auto-picking hits (<30 particles).

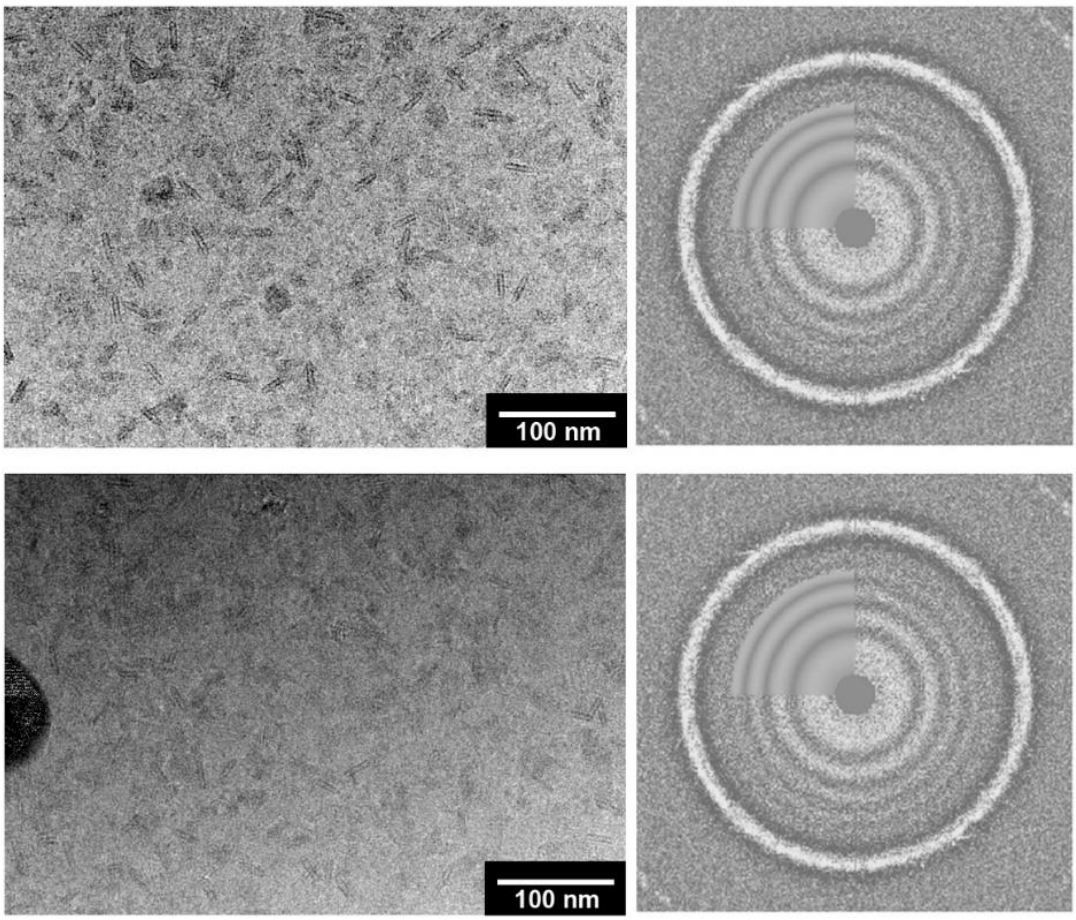

Figure 3-10 Typical movies which were omitted after CTF estimation characterized by problematic Thon rings, which may be caused by the carbon film of cryo-grids, i.e. the image was accidentally taken off the hole.

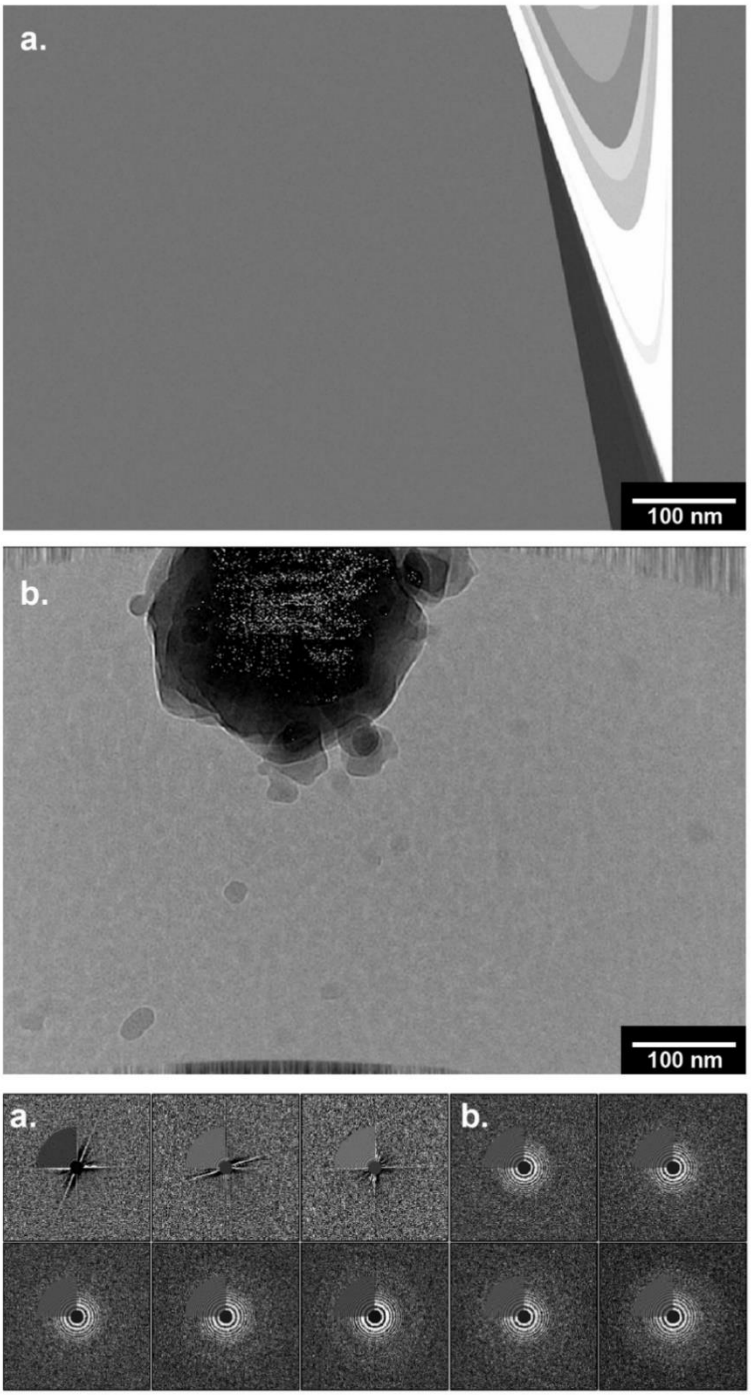

Figure 3-11 Typical movies which were omitted after CTF estimation for the reason of improper data collection (Type a.) and losing focus caused by impurities (Type b.). The estimated resolution of these movies were also limited (>5 Å).

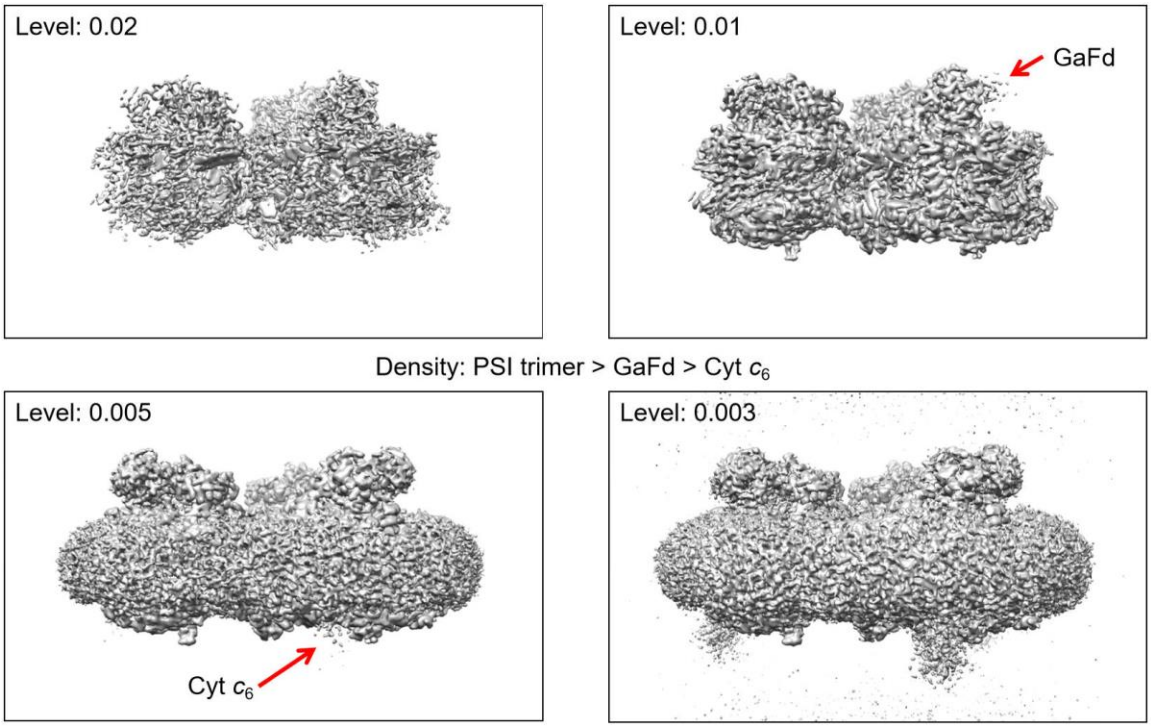

Figure 3-12 Density map after 3D auto-refinement with different threshold applied, which presented the density level difference of each protein.

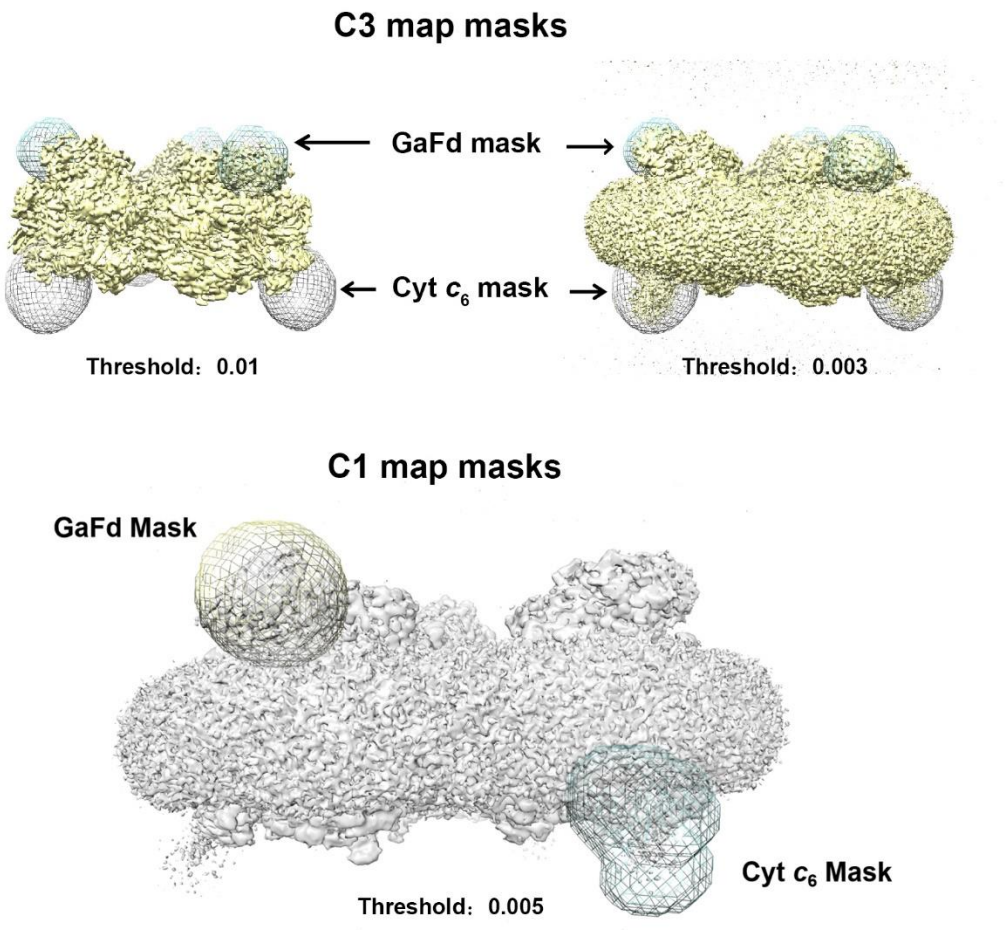

Figure 3-13 The masks for local 3D classification and auto-refinements in density maps applying C3 and C1 symmetry, respectively.

3.2.11 Atomic model building and refinement

Coot[101], Phenix[102], MolProbity and UCSF Chimera were used for model building and real space refinement. The X-ray crystal structures of the *Synechococcus elongatus* PSI trimer determined at 2.5 Å resolution (PDB ID: 1JB0[36]) and of the *T. elongatus* BP-1 ferredoxin X-ray crystal structure determined at 1.5 Å (PDB ID: 5AUI[80]) were used as a starting model for real space refinement in Phenix 1.19.2 after manual fitting in UCSF Chimera 1.13.1. Coot 0.9.5 was used for manual correction and minimization of rotamer, geometry, and Ramachandran outliers in the real space refined model. Accurate

non-metal ligand restraint files were downloaded from Grade Server (http://grade.globalphasing.org) and utilized during refinement. To account for the observed presence of magnesium on both sides of chlorine ring plane the chirality limitation of the magnesium binding plane in the restraints of chlorophylls (CLA and CL0) was deleted for realizing reasonable fitting within the density map. In addition, new iron-sulfur cluster restraints[103] using a rhomboid geometry were applied for iron–sulfur clusters (SF4) refinement. The newly modified restraint files have been uploaded together with model to the wwPDB deposition site Visualization of maps and models in all figures were performed using UCSF Chimera 1.13.1 and ChimeraX 1.2.5. For the docking simulation trial of Cyt c_6 we used the Phenix "Dock in map" routine with the input of local density map and the *T. elongatus* BP-1 Cyt c_6 X-ray crystal structure determined at 1.7 Å resolution (PDB ID: 6TR1[74]).

3.2.12 Data availability

All 3,018 raw Cryo-EM movies were deposited in the Electron Microscopy Public Image Archive (EMPIAR) under the accession number EMPIAR-10928. The final Cryo-EM Coulomb density map has been deposited in the Electron Microscopy Data Bank (EMDB) under the accession number EMD-31605. The atomic coordinates of the refined PSI-Fd model have been deposited in the Protein Data Bank (PDB) under the accession number 7FIX. All relevant data are available from the corresponding authors upon reasonable request.

3.3 Results

3.3.1 Structure Determination

For high resolution structure determination by single particle cryo-EM trimeric PSI was purified using the membrane fraction obtained from large scale cultures of the thermophilic cyanobacterium *T. elongatus* BP-1 employing a combination of nickel affinity

chromatography and sucrose density gradient ultracentrifugation. This yielded PSI trimer preparations of high purity, homogeneity and concentration which were further optimized for single particle cryo-EM by detergent exchange to GDN and removal of excess free detergent by GraDeR[94]. The soluble electron donor Cyt c_6 was purified from the same *T. elongatus* cultures employed for PSI isolation using the water soluble fraction, whereas the water soluble electron acceptor Fd was expressed and isolated using *E. coli* cultures. The latter enabled us to prepare Gallium substituted Fd that cannot be reduced, ensuring strong binding to PSI at redox state homogeneity. Fd and Cyt c_6 were mixed with PSI and used for cryo-grid screening in a 200 kV cryo-TEM (Talos Arctica, TFS).

A cryo-grid exhibiting large areas of suitable vitreous ice thickness with high particle density in hole centers was then transferred to a high end 300 kV cryo-TEM equipped with a cold-FEG, energy filter and a K3 direct electron detector (CRYO ARM 300, JEOL; Gatan) for automatic acquisition of 3,018 movies by SerialEM. Image processing in Relion 3.1 yielded a final map calculated from 207,142 particles at an overall resolution of 1.97 Å and of sufficient quality at the Fd-PSI binding interface to visualize side chain density and water molecules.

3.3.2 Overall structure

Viewed along the membrane plane the Ferredoxin bound PSI trimer resembles the shape of a clover leaf with a diameter of ~200 Å and a total weight of 1,110 kDa. Since no significant differences between the non-symmetrized (C1) Coulomb density map at 2.07 Å and the symmetrized (C3) map at 1.97 Å resolution were observed, the latter one was used for atomic model building. As starting models we employed the *T. elongatus* PSI crystal structure solved to 2.5 Å resolution (PDB ID 1JB0) and the Gallium substituted *T. elongatus* Ferredoxin crystal structure solved to 1.5 Å resolution (PDB ID 5AUI).

In our model (**Fig. 3-14**) all 12 subunits of each *T. elongatus* PSI monomer, that is PsaA, PsaB, PsaC, PsaD, PsaE, PsaF, PsaI, PsaJ, PsaK, PsaL, PsaM and PsaX, were

included in addition to three Ferredoxins equally bound to the stromal side to PsaA, PsaC and PsaE. Though density for luminal bound Cyt c_6 is visualized in the map its poor density prompted us to not include Cyt c_6 in our atomic model. The complete model thus contains a total of 39 polypeptide chains, 285 chlorophyll a, three chlorophyll a', 72 β-carotenes, 6 phylloquinones, 9 [4Fe-4S] iron-sulfur clusters, 3 [2Fe-2S] iron-sulfur clusters, 3 Ca^{2+} ions, 6 phosphatidyl glycerols, 3 digalactosyldiacylglycerols, 348 water molecules and 51 lipids built without headgroup.

Notable differences to our starting model 1JB0 are the identification of the previously as a monogalactosyldiacylglycerol modelled Lipid II as a digalactosyldiacylglycerol and the change of PsaL residue 143 from a leucine to a serine, matching now the primary sequence data bank entry for PsaL (UniProtKB - Q8DGB4). The **Fig. 3-16** presents representive added/modified molecules) In addition, our map allowed us to extend the starting model by 40 amino acid residues, namely Lys11-Val12, Gly263-Ile265 in PsaA, Gly740 in PsaB, Thr5-Val19, Ala33, Pro44-Phe54, Gln78-Leu83 in PsaK and Glu3 in PsaL. We also found that the chlorophyll bound to PsaM (CLA 1601 in 1JB0) to be missing. Furthermore, the β-carotenes BCR102 of PsaK, BCR855 of PsaA have been newly modelled together with a newly found chlorophyll CLA4017 of PsaJ. Finally, a total of 17 new lipids at each monomer-monomer interface could be built into our model.

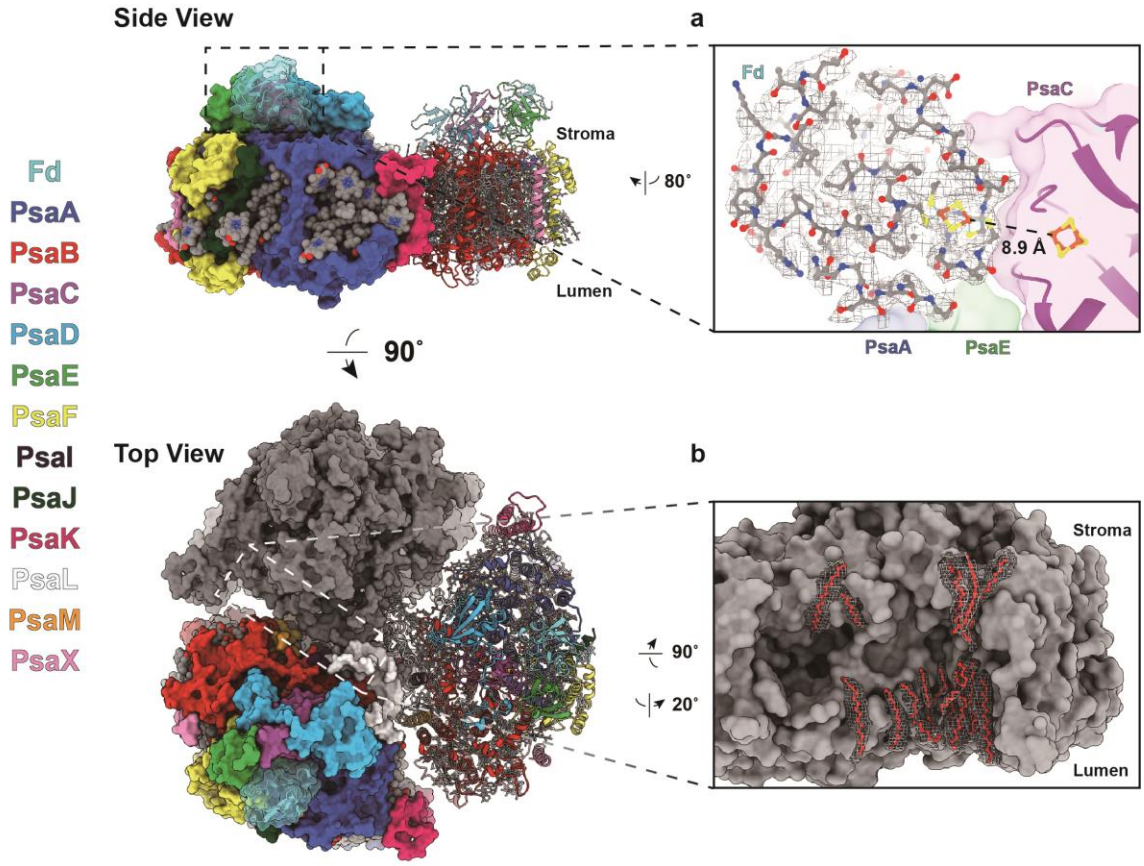

Figure 3-14 Overall architecture of PSI-GaFd complex. View from parallel to the thylakoid membrane ("side-view") and stromal side ("top-view") respectively. Complex model is in C3 symmetry, each symmetric element is represented in gray surface, surface colored by subunit chain (PsaA-blue, PsaB-red, PsaC-purple, PsaD-light blue, PsaE-green, PsaF-yellow, PsaI-dark purple, PsaJ-dark green, PsaK-pinkish red, PsaL-white, PsaM-orange, PsaX-pink, Fd-cyan) and colored cartoon style separately. Ligands are presented in sphere and stick style separately, which colored by element. **a.** A zoomed-in view of ferredoxin binding interface overlapped with density map. **b.** Lipids between PSI monomers overlapped with their density map.

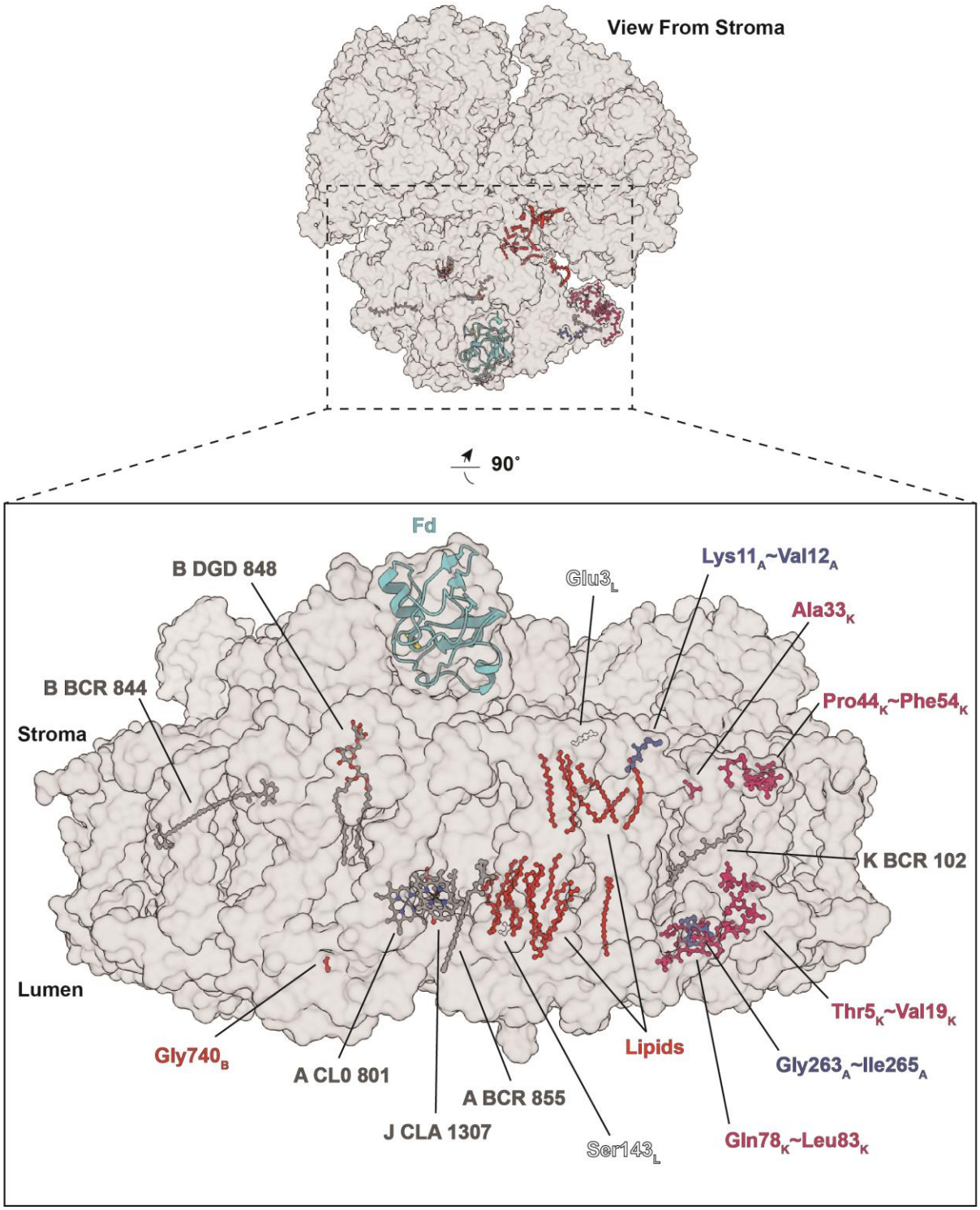

Figure 3-15 All newly added/ modified residues and ligands. Fd was also presented as cartoon with transparent surface overlapped. Amino acid residues were colored by subunits. Ligands were colored by elements. Lipids are colored in red.

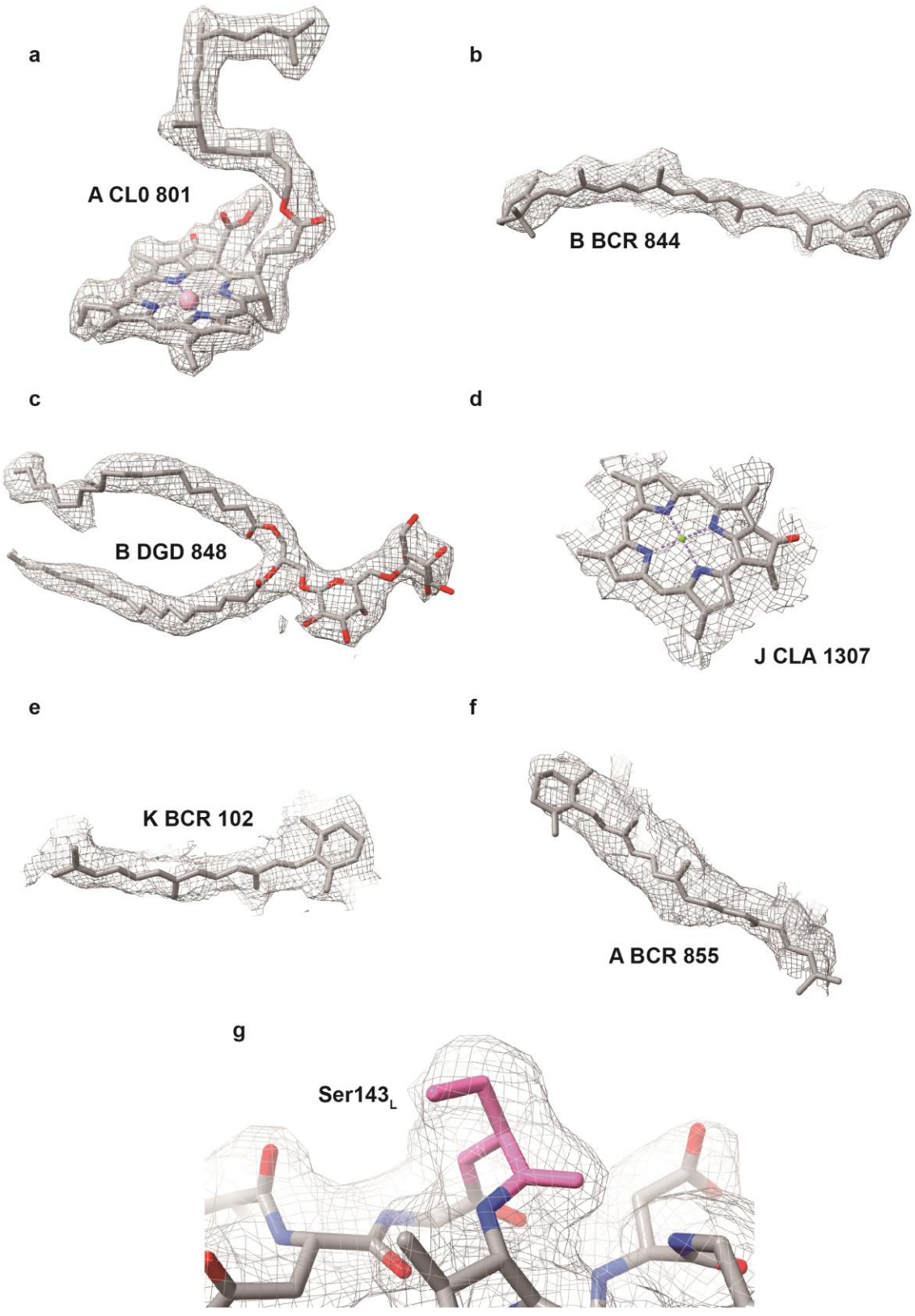
a
A CL0 801
b
B BCR 844
c
B DGD 848
d
J CLA 1307
e
K BCR 102
f
A BCR 855
g
Ser143L

Figure 3-16 Representative added/modified molecules. **a.** Chlorophyll A1011 was assigned as chlorophyll a isomer (PDB Ligands category CL0) based on density map. **b.** β-carotene B4009 was completely built with all atoms. **c.** Previous 1,2-Distearoyl-monogalactosyl-diglyceride (MGDG, PDB Ligands category LMG) B5008 was modified to Digalactosyldiacylglycerol (DGDG, PDB Ligands category DGD) based on newly detected extra density. **d.** Newly assigned chlorophyll J4017 overlapped with surrounding density. **e.** and **f.** presented newly assigned β-carotene K104 and A6001 with partly built atoms. **g.** The 143th amino acid residue (coloed in pink) in subunit PsaL was modified from leucine to serine based on Uniprot sequencing result and coresponded density map.

3.3.3 Electron transport chain

The electron transport chain (ETC) in PSI starts with P700, an opposing pair of chlorophyll a and chlorophyll a' situated perpendicular to the membrane plane as the site of light induced charge separation. Branch A and branch B of the ETC, both composed of two closely stacked chlorophyll a and one phylloquinone, end in equidistance to the 4Fe-4S iron-sulfur cluster F_X which is coordinated by both PsaA and PsaB. PsaC hosts the 4Fe-4S iron-sulfur clusters F_A and F_B, the two last components of the ETC, of which F_B is the final electron acceptor and the point of electron transfer to the docked soluble electron acceptors ferredoxin or flavodoxin.

The high local resolution of 1.8 Å in our PSI-Fd Coulomb density map together with suitable refinement restraints used to build our model enabled us to measure co-factor distances in the ETC with a high level of confidence. The observed edge-to-edge distances between phylloquinones and the three 4Fe-4S iron-sulfur clusters is in agreement with those previously determined in the 2.5 Å X-ray crystal structure 1JB0. Also, the distance between F_B and 2Fe-2S of Fd at 8.9 Å is short enough for efficient electron tunneling and matches that found in the PSI-IsiA-flavodoxin supercomplex. This distance is also equivalent to the mean of the three differing distances observed in the

PSI-Fd X-ray crystal structure. Interestingly, all these edge-to-edge co-factor distances are shorter than those reported for the higher plant PSI-Fd-Pc triple complex.

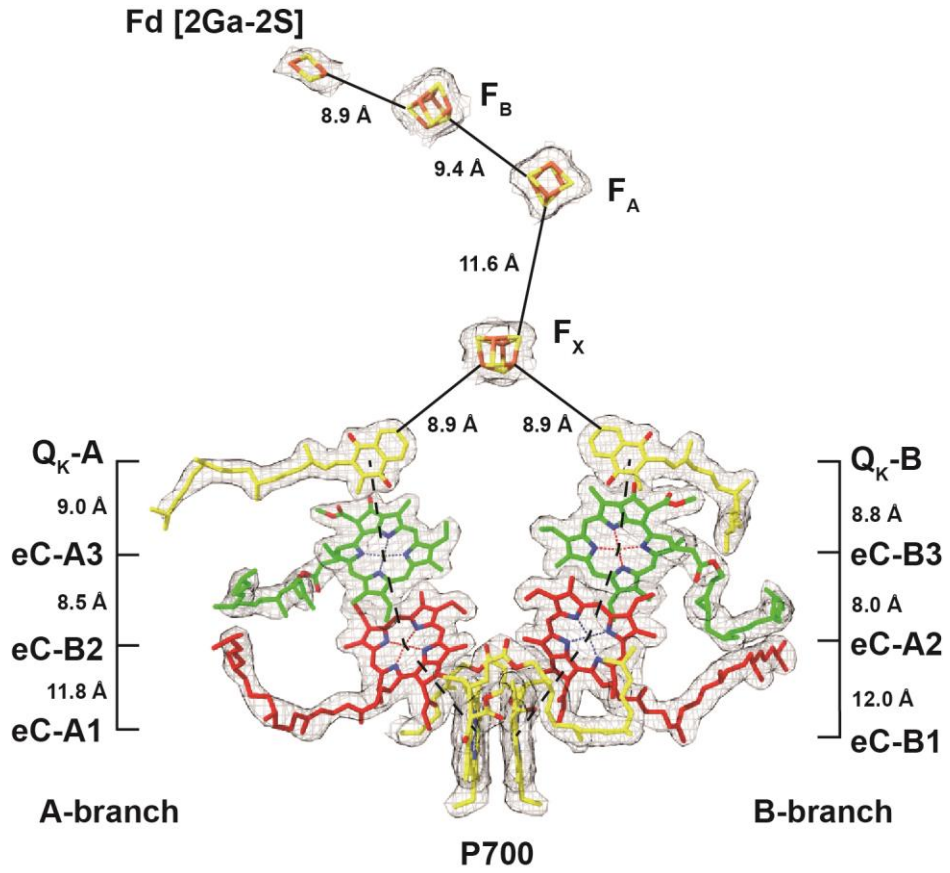

Figure 3-17 Core electron transfer chain (ETC) molecules in PSI-GaFd complex overlapped with Cryo-EM densities. Distances between molecules were measured in 2 ways: distance between Mg-Mg / Mg-phylloquinone center (dashed lines), and edge-to-edge distance between two molecules (solid lines).

3.3.4 The Cyt *c*$_6$-like density

The **Fig. 3-18** presented local resolution of density map in both top-view and side-view. In raw density map without any modification and masking, low density features were found when downscale the threshold of map density level from 0.007 to 0.002 (**Fig. 3-18b**). Densities presented almost identical features in maps with/without symmetry

applied, and not obtained distinguishable improvement after masked 3D classification/refinement were performed (Results not shown). The densities surrounding PSI trimer were inferred as detergent micelle with local average resolution of around 3 Å. Extra densities were also found at lumenal side of PSI trimer in C3 symmetry, which were inferred as potential Cyt c_6 binding site correspondingly.

The local resolution of this area approached 3 Å at PSI-proximal side, and over 4 Å at PSI-distal side. The **Fig. 3-18c** presented zoomed-in view of this area, and Cyt c_6 atomic model (PDB ID: 6TR1) determined by X-ray diffraction was docked for simulation. Although docked Cyt c_6 model was with similar size and volume as density feature, the limited resolution and high noisiness blocked reliable orientation determination. Docked Cyt c_6 was not included in the final model of complex, which was only presented in docking diagram since the unauthentic interactions with PsaB, PsaF and PsaX.

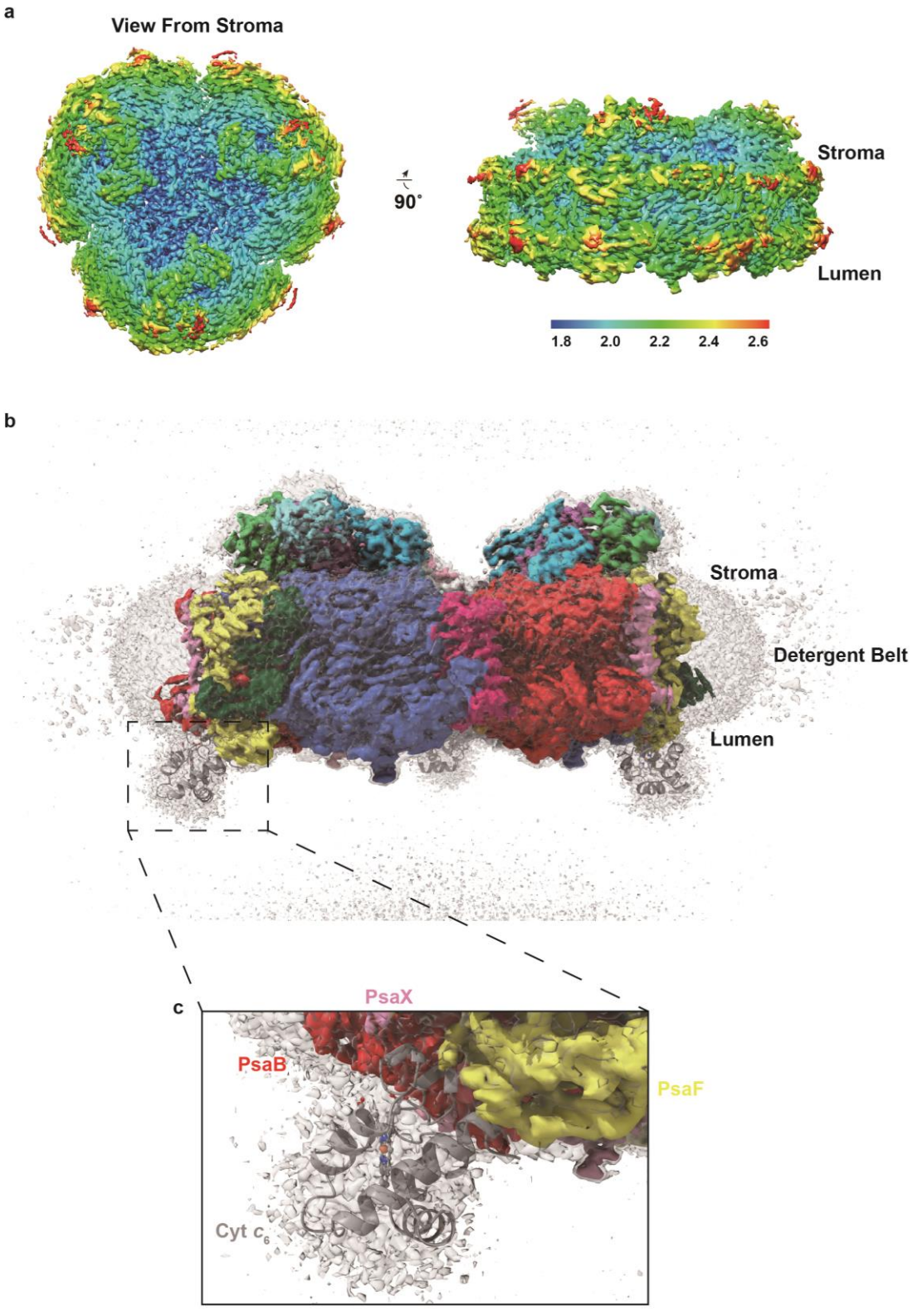
a
View From Stroma
90°
Stroma
Lumen
1.8
2.0
2.2
2.4
2.6
b
Stroma
Detergent Belt
Lumen
c
PsaX
PsaB
PsaF
Cyt c_6

Figure 3-18 Local resolution of Cryo-EM density map and Cyt c_6-like extra density. **a.** Density map surface colored by local resolution. **b.** Overlapped density map with different threshold level shows potential Cyt c_6-like density. Solid density colored by subunit (same as **Fig. 3-14**) with threshold level 0.007, transparent density with threshold level 0.002. Gray cartoon represents docking simulation result of Cyt c_6. Docking simulation details see Method part.

3.3.5 Masked 3D classification and auto-refinement

In order to optimize the signal/noise ratio of density map regarding electron transfer partners (Fd and Cyt c_6), masked 3D classifications and following refinements were applied based on the density map in C1 and C3 symmetry. The masks of focused binding partners were prepared as shown in **Fig. 3-13**, which were prepared by "segment map" tool (Segger v1.9.5) in UCSF Chimera 1.13.1.

For the Fd-masked classification and refinement, different parameters such as T values and class numbers were tested for proper clustering, whose results were presented in **Fig. 3-19** (C1 symmetry) and **Fig. 3-20** (C3 symmetry). Generally, the class with Fd into the mask occupied the major percentage according to the classification results. Total 214,876 particles were applied to the masked 3D classification in C1 symmetry and 111,545 particles in C3 symmetry. With the higher T values were set, the estimated resolution of target class (which means particles with Fd binding orderly) will be better, whereas the particle numbers in target class would decrease meanwhile. On the other hand, the particle number also play important role in the following refinement step, which means inadequate particle number would also hinder the map construction to high resolution. As a result, the balance between effective separation (particles with/without Fd binding) and enough particles matters to the final perfoemance of masked classification and refinement.

With similar protocol, Cyt c_6-masked classification and refinement were also performed as **Fig. 3-21** and **Fig. 3-22** showed. Different with the Fd, the classification

results looks more separated when 5 class number was set. In **Fig. 3-22**, all classes were occupied with particles, where as in the 5-class classification result of Fd (table in **Fig. 3-20**), only 2 or 3 classes were occupied with particles. Such difference of cluster distribution indicated the binding features of the two electron transfer proteins. For Fd, the binding characterization should be relatively sample and clear, whereas the binding of Cyt c_6 should be more flexible and unspecific, which maybe the reason of low local resolution.

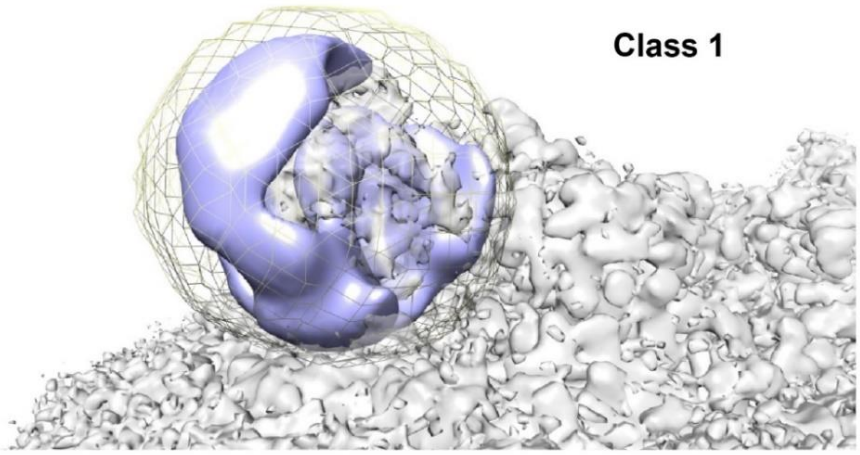

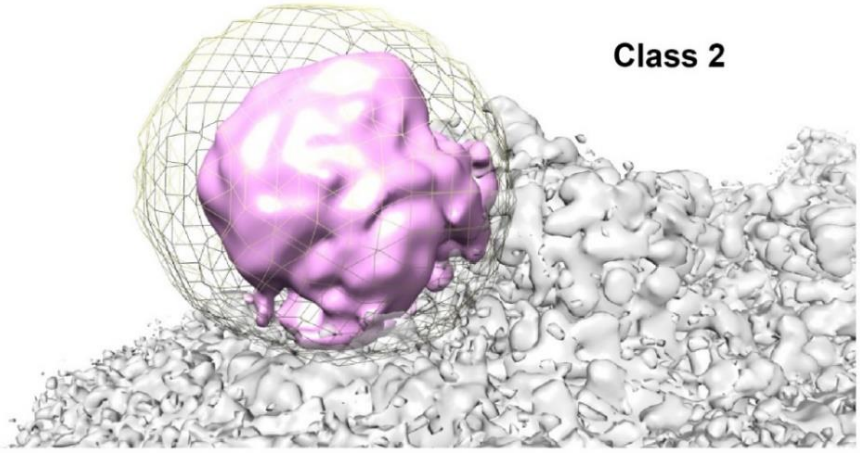

T Value	Class	Particles	Estimated Resolution
10	1	11367	0
	2	203509	7.42
20	1	37889	9.72
	2	176987	6.26
30	1	16311	10.44
	2	198565	5.64
40	1	171416	5.12
	2	43460	8.29
50	1	70988	7.42
	2	143888	4.62

Figure 3-19 Typical GaFd masked auto-refinement results (parameters in red box) of each class overlapped with density map in C1 symmetry. The form below listed the masked 3D classification distribution with different T value applied.

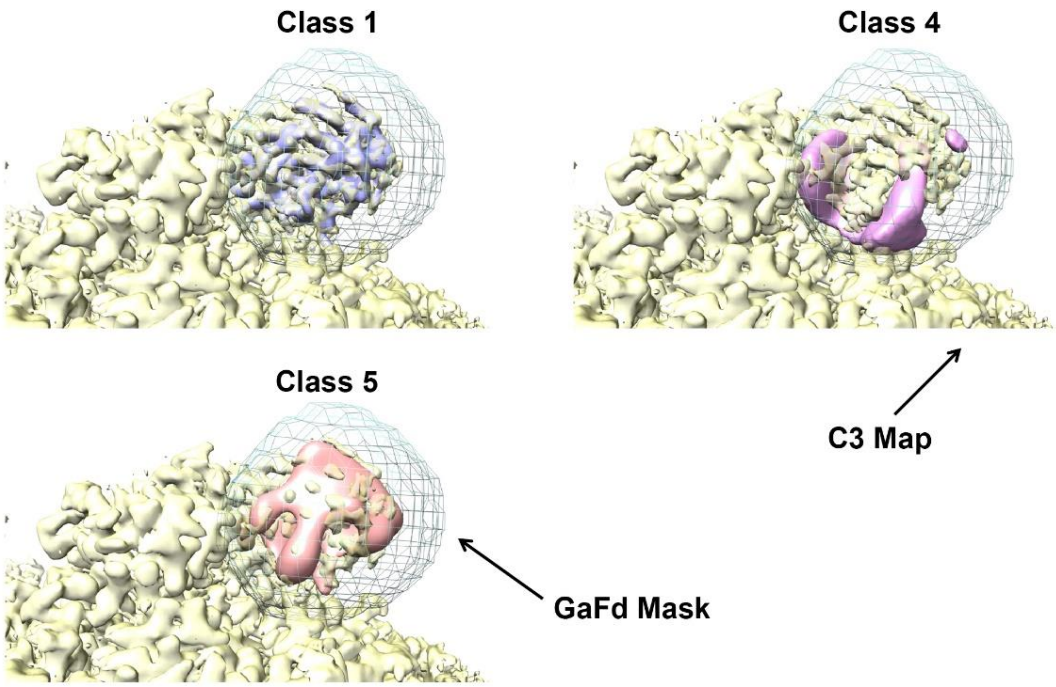

T Value	Valid class	Class	Particles	Estimated Resolution
10	3	1	12053	8.26
		2	2537	16.12
		4	96955	6.45
20	2	4	39841	5.46
		5	71704	6.32
30	3	1	1130	12.89
		2	43403	4.47
		3	67012	5.97
40	2	4	110153	4.03
		5	1392	8.71
50	3	1	18	322
		2	5449	6.2
		3	106078	3.93
60	3	1	105871	3.7
		4	3791	10.4
		5	1883	7.49
70	3	1	52075	3.7
		3	8	0
		5	59462	5.2

Figure 3-20 Typical GaFd masked auto-refinement results (parameters in red box) of each class overlapped with density map in C3 symmetry. The form below listed the masked 3D classification distribution with different T value applied.

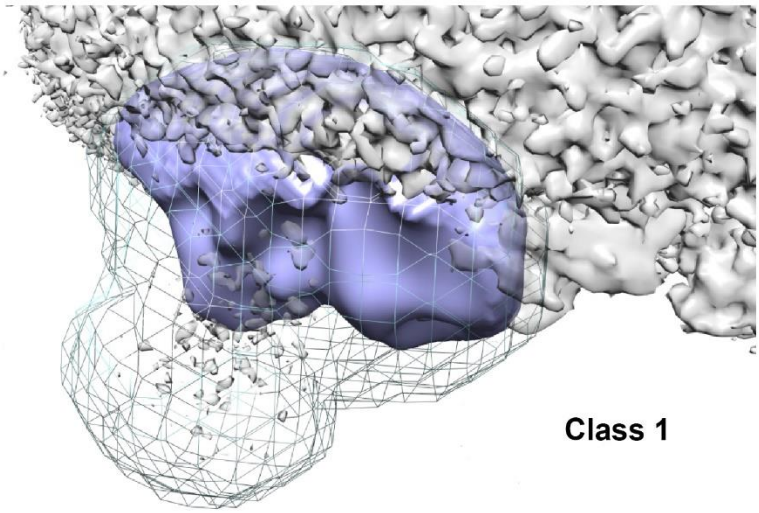

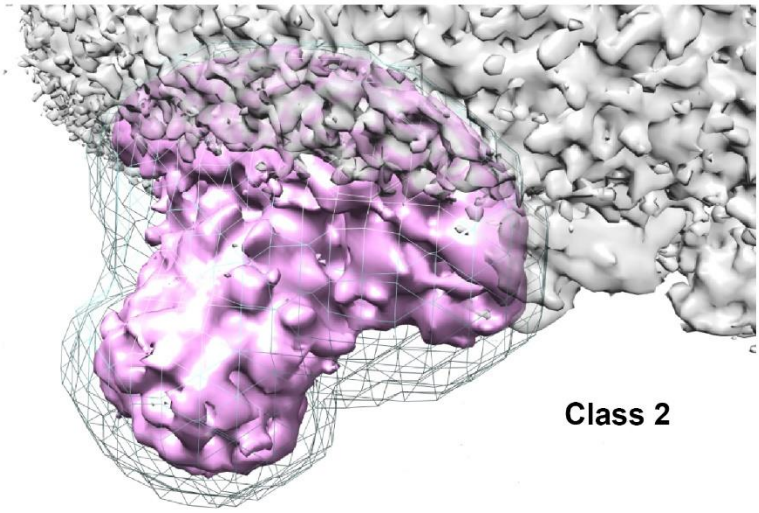

T Value	Class	Particles	Estimated Resolution
4	1	207554	7.83
	2	7322	18.8
10	1	204373	6.26
	2	10503	14.1
25	1	14397	11.75
	2	200479	4.55
50	1	31201	8.06
	2	183675	3.81

Figure 3-21 Typical Cyt c_6 masked auto-refinement results (parameters in red box) of each class overlapped with density map in C1 symmetry. The form below listed the masked 3D classification distribution with different T value applied.

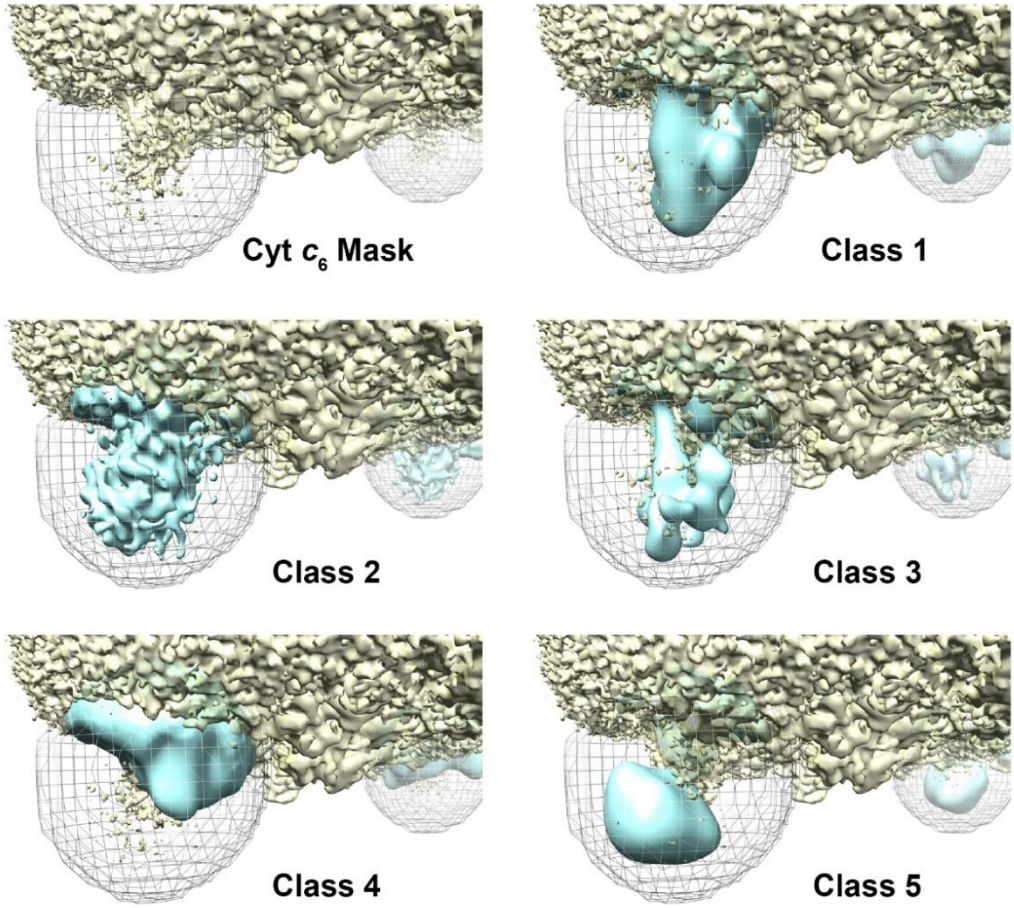

T Value	Class	Particles	Estimated Resolution	T Value	Class	Particles	Estimated Resolution
10	1	560	18.96	50	1	25802	4.54
	2	982	15.35		2	4247	6.85
	3	18187	8.95		3	14377	4.41
	4	6425	10.74		4	8249	7.16
	5	85391	4.88		5	58870	3.42
20	1	1863	12.4	60	1	969	10.4
	2	96075	3.88		2	44239	3.54
	3	4682	7.16		3	18926	5.75
	4	6637	10.07		4	46421	3.35
	5	2288	13.43		5	990	9.48
30	1	10805	7.67	70	1	10405	6.85
	2	41329	4.24		2	6863	6.2
	3	56621	3.7		3	27292	3.62
	4	1629	11.94		4	844	9.48
	5	1161	12.4		5	66141	3.22
40	1	68634	3.46				
	2	13131	7.16				
	3	1549	10.74				
	4	2719	9.21				
	5	25512	4.08				

Figure 3-22 Typical Cyt c_6 masked auto-refinement results (parameters in red box) of each class overlapped with density map in C3 symmetry. The form below listed the masked 3D classification distribution with different T value applied.

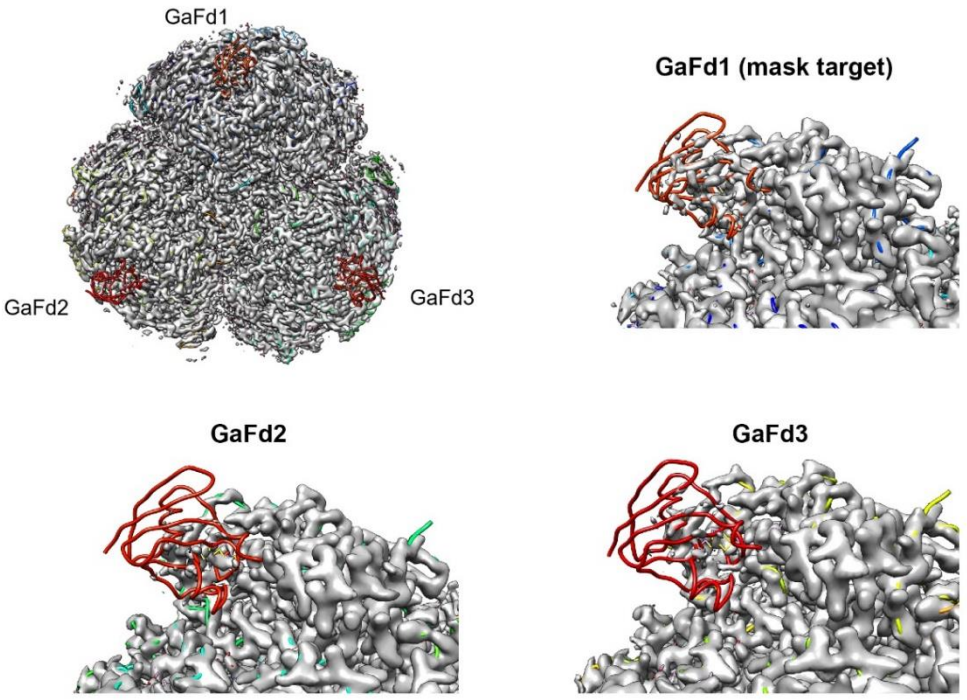

Lowpass filter	Class number	T value	Class	Particles	Resolution
5	2	10	1	150214	3.93
			2	26939	12.4
10	2	10	1	26911	12.4
			2	150242	3.98
5	5	3	1	4969	21.4
			2	14498	17.9
			3	2037	24.8
			4	154406	5.86
			5	1243	23
5	10	10	1	6231	16.12
			2	992	21.4
			3	150132	3.93
			4	636	23
			5	3104	17.91
			6	1348	18.9
			7	1411	17.9
			8	825	21.4
			9	452	23.02
			10	12022	15.35
0	10	4	9	153826	5.28
			other	23327	-
30	10	4	7	153986	5.28
			other	23167	-
30	10	10	10	149896	3.83
			other	27257	-

Figure 3-23 Density bias of each GaFd overlapped with structure of PSI:Fd complex model (PDB ID: 5aui, all three Fds were colored in red) at same threshold. The form below showed the results of single GaFd masked 3D classification results with different parameters (lowpass filter, class number and T values). Particles in the class in red box were applied for the density map construction.

As for the single Fd-masked classification and refinement result presented in Fig. 3-23, with more parameters (Lowpass filters and other class numbers) tested, one class with acceptable resolution and particle number was selected and extracted for the following polishing and map construction. The local resolution of Fd was not improved much when compared with previous map, however, the density level difference of masked Fd (GaFd1) to other two Fds (GaFd2 and GaFd3) became detectable as shown in **Fig. 3-23**. Such difference may be caused by the lower occupancy of other Fds in the particles, which might mean that not all PSI trimers are bound with three Fd. The characterization of Fd binding with PSI should be measured by other methods such as ITC measurements.

3.3.6 Interactions between PSI and Fd

Three PSI subunits (PsaA, PsaC, PsaE) take directly part in the binding of Fd. **Figure 3-25** presents the relative location of each interactive subunit in the PSI trimer complex. Zoomed in views of interaction between Fd with each subunit are presented in detail from the visual angle of dashed square. The interaction-involved amino acid residues and water molecules were determined by DIMPLOT program in LigPlot+ suite30. Based on the DIMPLOT analysis result, total 18 residues within PSI subunits(Arg36, Arg40, Thr60 in PsaA; Ile11, Gly12, Gln15, Arg18, Lys34, Ala35, Ala56, Pro58 in PsaC; Arg3, Ile37, Arg39, Ser53, Asn56, Thr57, Asn59 in PsaE) and 20 residues within Fd (Ser60, Asp61, Asp67, Ile70 with PsaA; Phe38, Ser39, Cys40, Ala44, Cys45, Thr47, Phe64, Tyr97 with PsaC; Glu23, Tyr24, Asp27, Glu31, Cys40, Arg41, Ala42, Ser63 with PsaE) were involved in the binding by electrostatic or hydrophobic interactions. In general, 4 residues (Glu23, Asp27, Phe38 and Thr47) in Fd were newly found related to the binding interaction, whereas 4 Fd interactive residues (Gln62, Asp66, Glu71 and Tyr81) described in previous co-crystallization structure20 were not found in model described here. Moreover, total 6 water molecules (HOH109 to Fd:PsaA, HOH103, HOH105,

HOH107 to Fd:PsaC, HOH104, HOH108 to Fd:PsaE) were closed to the binding surface, offering potential hydrogen bond linkage between PSI and Fd. **Figure 3-25 (a-f)** presented distribution of binding-related molecules within protein in ball-and-stick style. Electrostatistic distribution was also presented by colored surface (negative in red, positive in blue).

Two important PSI:Fd binding interfaces are shown in **Fig. 3-24**. A pair of cation-π interactions between Phe38 of Fd with Lys34 of PsaC and Arg41 of Fd were identified (**Fig. 3-24a**). Arg39 of PsaE, which interacts with Arg41 of Fd through hydrophobic interactions, makes additional interactions with Asp27 and Tyr24 of Fd. Residue Gln15 of PsaC forms the greatest number intermolecular interactions between PSI and Fd, and may be strategically situated within the vicinity of electron donating and accepting clusters (**Fig. 3-24b**). Gln15 of PsaC is engaged in hydrophobic interactions with Cys45 and Phe64 of Fd and also makes a hydrogen bond to Ala44. In addition, via a hydrogen bond to HOH205, Gln15 of PsaC is connected to the C-terminal Tyr97 of Fd. Tyr97 in turn makes a cation-π interaction to Arg18 of PsaC. Tyr97 of Fd exhibits a well-defined density, which is surprising given the known flexibility of the C-terminus (as shown in **Table 3-3**), indicating strong interactions between Fd Tyr97 and PsaC.

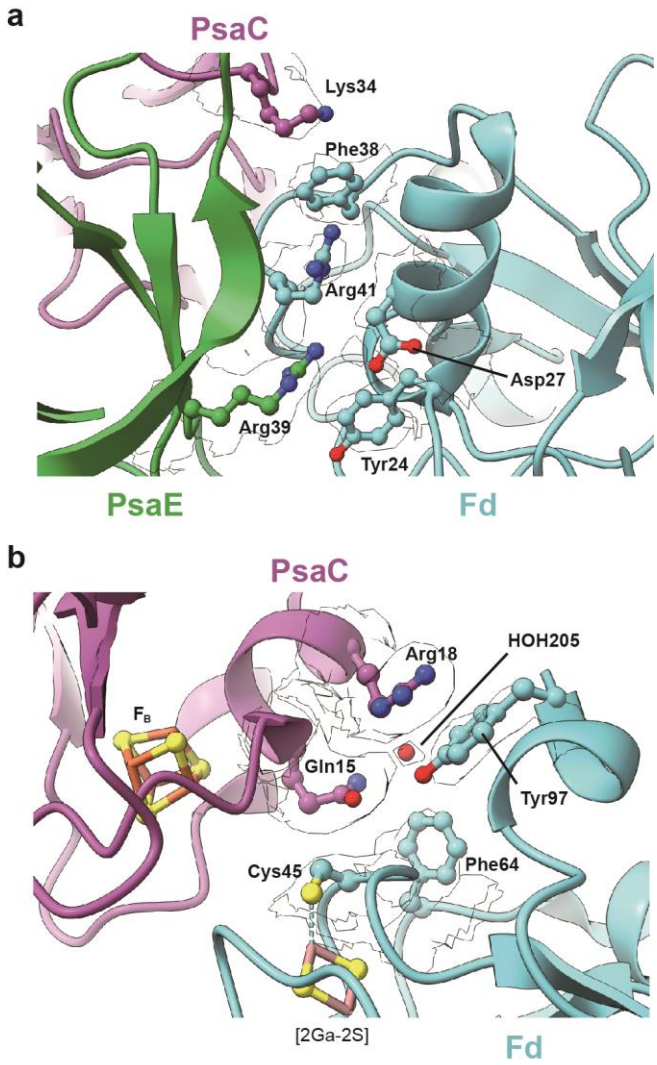

Figure 3-24. Key sites of Fd-PSI interaction. **a** Nexus of interactions that contribute to the binding affinity of PSI with Fd. Crucial PSI residues Lys34 of PsaC and Arg39 of PsaE and their respective Fd binding partners are highlighted. PsaC in purple ribbon, PsaE in green ribbon, Fd in cyan ribbon and their interacting residue side chain atoms in ball and stick with their corresponding density in silhouette. **b** Hub of interactions around Gln15 of PsaC and with Cys45, Phe64 and Tyr97 of Fd. These residues undergo a conformational change upon Fd reduction. PsaC in purple ribbon, Fd in cyan ribbon and interacting residues side chain atoms in ball and stick with their corresponding density in silhouette. Interfacial water 205 is shown as a red ball. Iron-sulfur cluster FB of PSI and the gallium-sulfur cluster of Fd is depicted in ball and stick format.

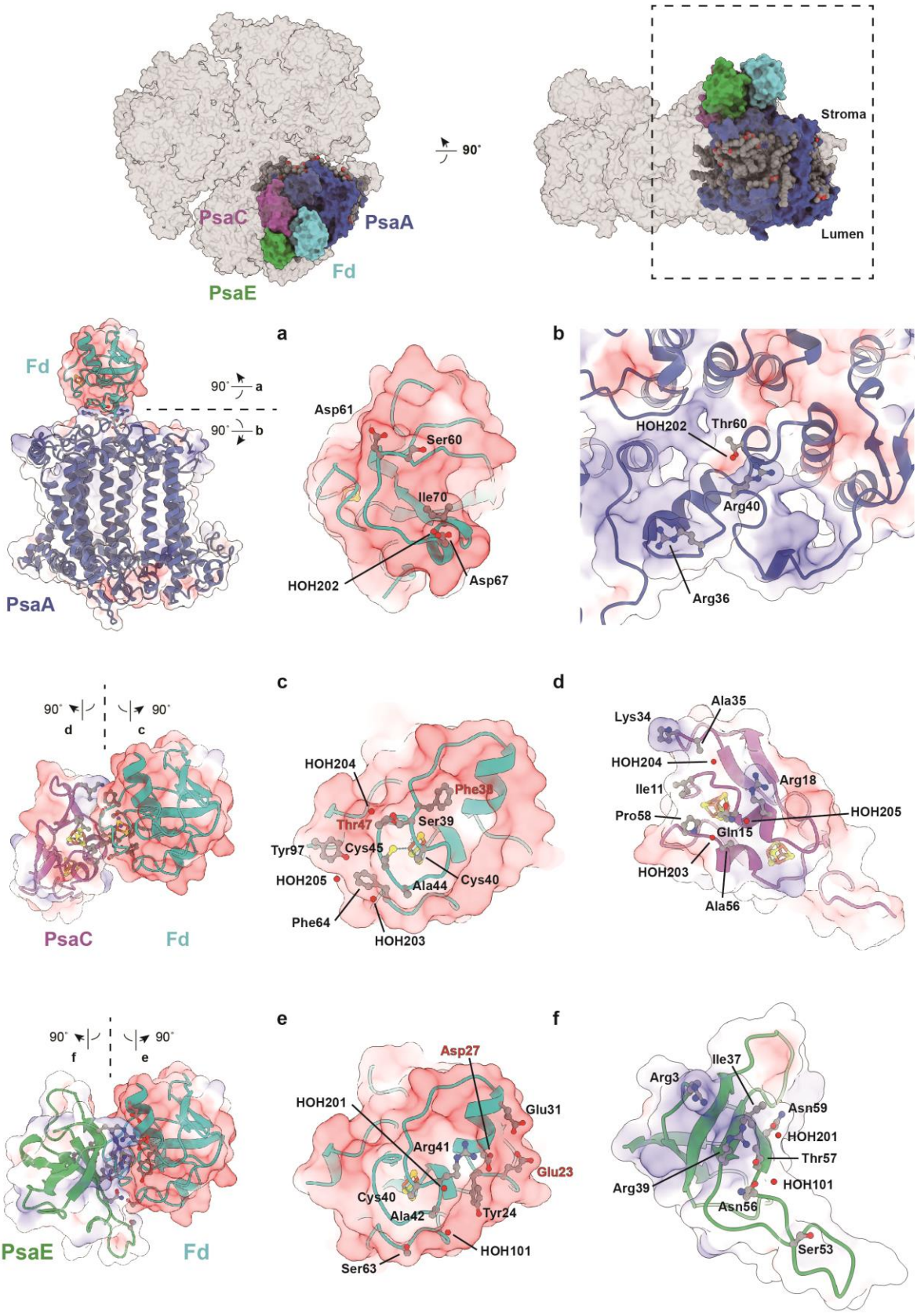
PsaC
PsaA
Fd
PsaE
90°
Stroma
Lumen
Fd
90° a
90° b
PsaA
a
Asp61
Ser60
Ile70
HOH202
Asp67
b
HOH202
Thr60
Arg40
Arg36
90° d
90° c
PsaC
Fd
c
HOH204
Phe38
Thr47
Ser39
Tyr97
Cys45
HOH205
Ala44
Cys40
Phe64
HOH203
d
Ala35
Lys34
HOH204
Arg18
Ile11
Pro58
HOH205
Gln15
HOH203
Ala56
90° f
90° e
PsaE
Fd
e
Asp27
HOH201
Glu31
Arg41
Glu23
Cys40
Ala42
Tyr24
HOH101
Ser63
f
Ile37
Arg3
Asn59
HOH201
Thr57
Arg39
HOH101
Asn56
Ser53

Figure 3-25 Ferredoxin (Fd) binding with PSI. Three PSI subunits (PsaA, PsaC, PsaE) involved in the binding interaction with Fd. **a-f.** Binding-relevant residues and water molecules of each protein. Proteins were colored same as **Fig. 3-14** in cartoon style. Protein surfaces were colored by electro statistic features (positive in blue, negative in red).

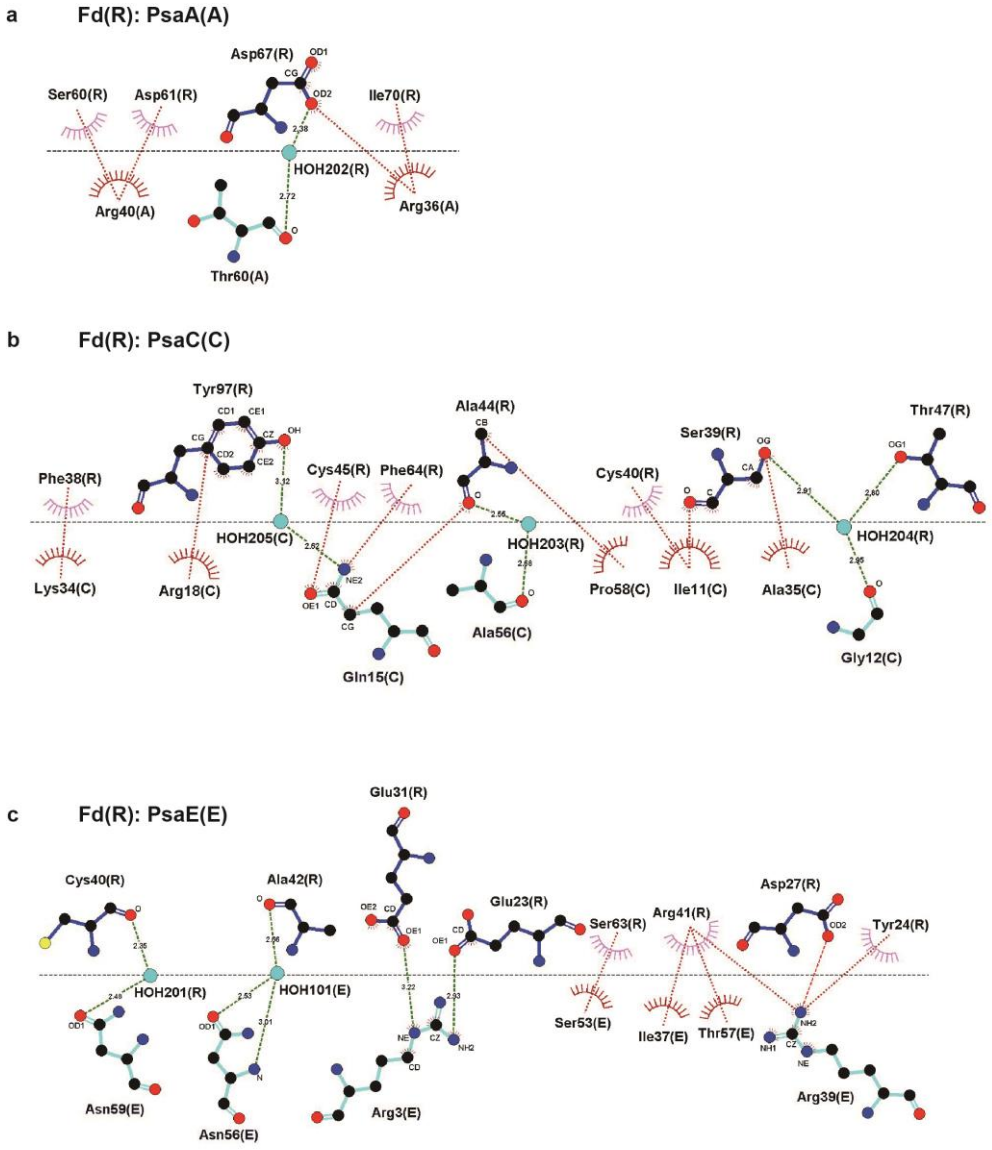

Figure 3-26 Protein-protein interface diagrams of Fd:PsaA, Fd:PsaC and Fd:PsaE derived from DIMPLOT in LigPlot+ suite. Green dashed lines represented potential hydrogen bonds. Red dashed lines showed all potential non-bonded contacts.

3.3.7 The ITC measurement

In order to obtain more thermodynamic details of interaction between Ga-substituted Fd and PSI trimer, Isothermal Titration Calorimetry (ITC) was performed to reveal the nature and features of complexation. Representative results of ITC thermogram and binding isotherm of interaction between Ga-substituted Fd and PSI trimer were shown in **Fig 3-27**. Thermodynamic parameters of ITC measurements (presented in **Table 3-2**) demonstrated that the binding stoichiometry value was approximately 3 (2.9 ± 0.2), indicating Fd was bound to each PSI monomer in ratio of 1:1 as Cryo-EM density map manifested. Meanwhile, the endothermic reactions of Fd to PSI and its titrating saturation indicated interprotein interactions were driven by uptaking heat. The Fd-PSI interactions showed energetically unfavorable positive ΔH (1.1 ± 0.1 kcal/mol) and favorable positive TΔS (9.5 ± 0.1 kcal/mol) value, revealing a purely entropy-driven complex formation. Strong interprotein affinity between GaFd and PSI was also observed based on measured K_d value of 758.0 ± 123.5 nM.

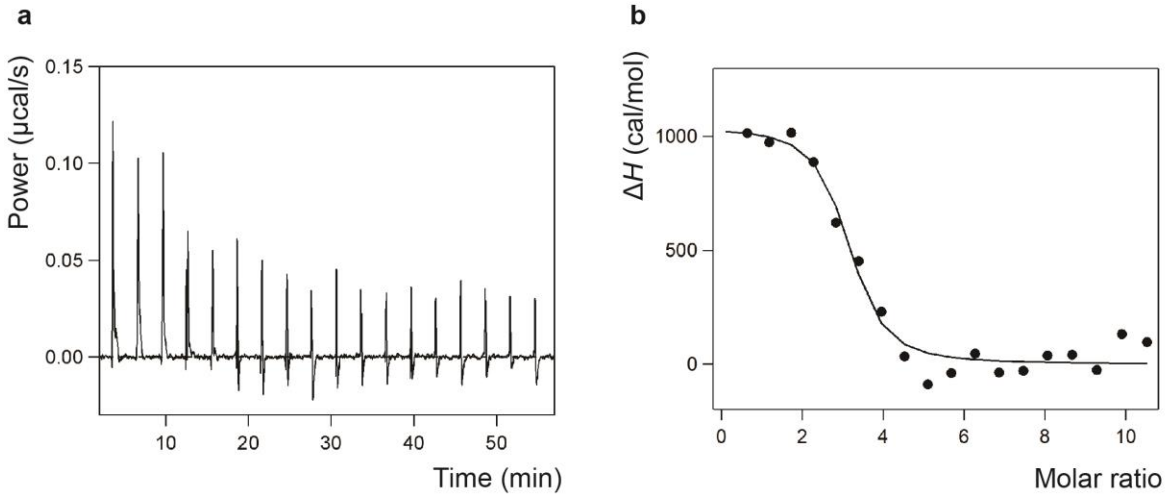

Figure 3-27 Representative results of ITC thermogram **(a)** and binding isotherm **(b)** of interaction between Ga-substituted Fd and PSI trimer.

	1st measurement	2nd measurement	3rd measurement	Mean ± S.E.M.
K_d (nM)	703	994	577	758.0 ± 123.5
Δ*G* (kcal/mol)	-8.4	-8.2	-8.5	-8.4 ± 0.1
Δ*H* (kcal/mol)	1.0	1.1	1.2	1.1 ± 0.1
-TΔS (kcal/mol)	-9.4	-9.3	-9.7	-9.5 ± 0.1
n	2.9	3.2	2.5	2.9 ± 0.2

Table 3-2 Thermodynamic parameters of the interaction between Ga-substituted Fd and PSI trimer. Three independent ITC experiments were performed at 25℃. Each set of the thermodynamic parameters obtained by fitting normalized ΔH in the binding isotherm are shown without fit errors. Mean and S.E.M. values were also presented, indicating the averaged value and the standard error of the mean, respectively. K_d: The dissociation constant; ΔG: The change in Gibbs free energy; ΔH: The change in enthalpy energy; ΔS: The change in entropy; n: The binding stoichiometry.

3.4 Discussion

In this Chapter, we described the high resolution Cryo-EM structure of cyanobacterial PSI in presence of oxidized Fd and reduced Cyt c_6. Our sample on the grid was prepared by simply mixing three proteins with no covalent cross-linking and being incubated in the dark before Cryo-EM grid preparation, which means the redox state of the complex was that just before the electron transfer from PSI to Fd originated from Cyt c_6. Furthermore, we used the Gallium-substituted Fd (GaFd), that was never reduced but structurally identical to the wild type oxidize Fd, to uniform the redox state of accepter side of PSI and eliminate a possibility of the unexpected redox reaction between Fd and PSI triggered by absorption of light. Despite extensive efforts to see the electron transfer complex of PSI:Cyt c_6, there was no X-ray or Cryo-EM structure of PSI:Cyt c_6 complex available before. In this analysis, we successfully found the Cyt c_6-like extra densities around the N-terminal part of PsaF (See **Fig. 3-18**). Surprisingly,

that density corresponding to Cyt c_6 was not close to the primary electron accepter of P700 in PSI (around 55 Å center-to-center distance from P700 to Cyt c_6-like density) but enough far from it to prevent the productive docking. Existence and positioning of the density was concrete as described in the result section, and this density blob was not present in the map of PSI-only Cryo-EM datasets (not published). Although the orientation of Cyt c_6 binding could not be determined due to lack of local resolution, it might be a secondary binding site for Cyt c_6 with a physiological meaning, which had obvious difference with the published PSI-Pc structure[90].

The recently reported Cryo-EM structure of PSI-Pc complex showed the productive binding of Pc close to P700 of PSI, in which Pc was positioned with a hydrophobic binding surface created by PsaA and PsaB, and the vacuolar plant specific extension of PsaF. Since cyanobacteria do not have an N-terminal extension of PsaF subunit for productive Pc/Cyt c_6 binding, it is impossible for Cyt c_6 to position similarly as Pc. Conversely, the newly found alternative binding of Cyt c_6 may protected PSI from over-reduction of PSI by increasing the affinity for Cyt c_6 far from the productive binding site. This is the first to see experimentally additional Cryo-EM densities in lumenal side of cyanobacterial PSI and would be a starting point of discussion about structural basis for mysterious Cyt c_6 docking, although many attempts such as covalent crosslinking of PSI and Cyt c_6 have been made[68]. Because the cyanobacterial PsaF was considered to be a trans-membrane signal transducer across the membrane by productive Fd binding as suggested in previous X-ray and this Cryo-EM structure (See **Fig. 3-29**), we would propose a possible function of the secondary binding site as follows.

Electron transfer kinetic analysis results from green algae and higher plants indicated bi-phasic features[104,105]: the fast electron transfer phase relevant to the reduction of P700, whereas the slow phase was responsible to the diffusion time of Pc/Cyt c_6 in the lumenal space to PSI centers. The structure basis of such kind of bi-phasic kinetics was highly responsible to the Lys-rich N-terminal of PsaF of vacuolar

plant. This protein region offered electrostatic interaction sites to electron donor protein, and played key role of guiding them into P700 reaction center[104]. The heterogeneous cross-linking result and kinetic features[106] indicated the existence of both activate and inactivate binding site. The cross-linking test performed in *Chlamydomonas reinhardtii* showed similar result[107]: almost all Cyt c_6 were bound with PsaF with a stoichiometric ratio of 1:1, and not bound with other subunits of PSI when PsaF was absent. Only 33% of Cyt c_6 performed fast electron transfer to P700, whereas other 67% inactive cross-linking indicated the existence of potential extra binding site. Such kind of binding site may be far from active site, but guarantee continuous fast electron transfer. However, not all cyanobacterial PsaF have the pre-binding structural basis as in green algae and higher plants, and the existence of fast phase in cyanobacteria was still with debate[106]. Recently, *in vivo* P700 reduction kinetic study derived from cyanobacterium *Synechocystis* sp. PCC6803 presented similar features as green algae and higher plants[108]. Above examples indicated electron donor (both Pc and Cyt c_6) could form pre-binding complex with PSI and realize fast electron donation after P700 was excited, which fit pretty well with our redox state of the complex before excitation of P700 and pre-binding of Cyt c_6 to PSI.

Then, why the local resolution of the density corresponding to Cyt c_6 was relatively low (around 4 Å) than those of other two proteins? The limited resolution may be caused by three possible reasons. One was that there is no need to be stable complex at the secondary binding site because the primary function of this pre-binding is just to anchor the Cyt c_6 molecules to reduce a chance forming a productive complex. Second reason was that Cyt c_6 may be quickly oxidized by PSI in presence of light, and the binding affinity of Cyt c_6 decreased upon oxidization as similarly as the case of oxidized Pc whose K_d value became six times larger than that observed for reduced Pc[105]. Such kind of “pre-escape” intermediate complex may result in the current “noisy” but still visible structural state. Another possibility was that, such kind of binding status occurred at only

small proportions of PSI, resulting in the limited occupancy at this pre-binding region, and in turn not enough signal for visualization by single particle averaging. Although we tried once to enhance the local signal by masked 3D refinement/classification as well as partial signal subtraction during data processing (result not shown), the visibility of this region was not improved remarkably. In the previous masked Cryo-EM investigation combined with cross-linking of PSI and Cyt c_6 from same cyanobacterium[68], no density was detected as Cyt c_6-related region in the luminal side. It becomes clear that the redox state of the acceptor side of PSI in the complex was crucial to see the electron donor protein in the luminal side.

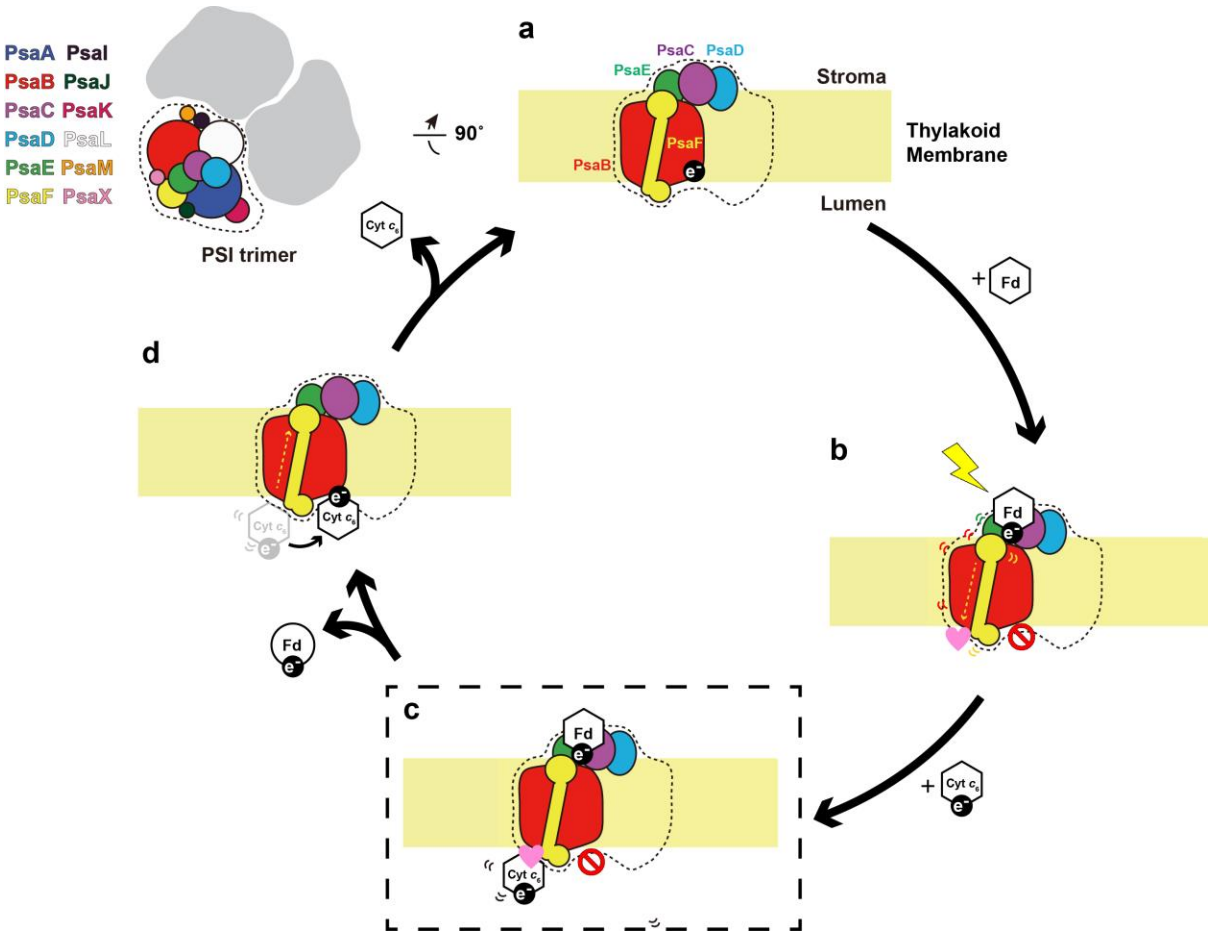

Figure 3-28 Schematic diagram of the proposed PSI electron pumping cycle. **a** Reduced Cyt c_6 and oxidized Fd are in a free unbound state. **b** Light induced charge separation across the membrane causes oxidized Fd to bind on the stromal side and opens up non-productive docking sites for Cyt c_6 on the luminal side. The pink heart shaped symbol represents an activated binding site and the 'closed' traffic sign represents a closed reaction center. **c** Cyt c_6 is bound to luminal non-productive docking sites while permanently oxidized Ga-Fd remains bound at the stromal side with the dashed line frame indicating the structure determined in this study. **d** The excited electron has left PSI with its soluble carrier Fd and the reduced Cyt c_6 has moved to the productive P700* proximal binding site for electron transfer and subsequent detachment from PSI.

Our Cryo-EM structure of PSI:Fd complex was described based on the density map with a strict three-fold rotational symmetry at an overall resolution of 1.97 Å. The better resolution than recently reported other PSI structures may be benefited from four major aspects: the protein samples with high purity and homogeneity, strictly controlled redox state of the transient electron transfer complex, optimized membrane protein complex preparation by GraDeR[94] method, and highly advanced microscope equipment (JEOL CryoARM300 with a cold field emission gun and Gatan K3 Summit detector). One noteworthy finding from higher resolution structure than other published structures was several stick-shaped densities between each PSI protomer (**Fig. 3-14b**), indicating the stable and specific packing of lipid tails. In the previous X-ray structure at 2.5 Å, three phospholipids and one galactolipid lipids were seen only inside of PsaA and PsaB subunits although thylakoid membrane contained various kid of lipids including but not limited to PG, MGDG, DGDG and SQDG[109]. Even excluding the ambiguous densities not easily distinguished from phytol tails of chlorophyll and densities with less convincing direction and too short length, still seventeen fatty acid tails were newly identified in our structure. Our newly found inter-protomer lipids were not determined by type because the densities of head groups were missing, which indicating that their head groups are mobile and flexible. Visible fatty acid tails were tightly attached to hydrophobic amino acid residues and antenna ligands (chlorophylls and β-carotenes) implying their potential function of stabilizing the trimerization of PSI. Our finding may fill the inconsistency between the numbers of lipid determined by structural and biochemical analyses[92].

Fd part of the complex was modeled based on density map at local resolution near 2.4 Å. A density of metal center, the [2Ga-2S] cluster in our case, and those of amino acid side chains were clearly visible and well modeled. A crystal structure of wild-type Fd from *T. elongatus* BP-1 (PDB ID: 5AUI) was a starting model for fitting and refinement[80]. Comparing to the previous X-ray analysis of PSI:Fd_{ox} complex at 4.2 Å[82], some differences in assignment of interacting residues were found, which was described in

Result part (**Fig. 3-25**). These differences in interpretation of interacting residues between Fd and PSI would happen because resolution has been improved so much; previous one was based on the distance between Cα-carbons while the new analysis include the side chains. In the current structure, the PsaD subunit was not involved in the interaction with Fd, which was against the result by the site-directed mutagenesis[110] but consistent with our previous X-ray analysis[82]. Structural changes upon complex formation were visualized (**Fig. 3-29**). When our Cryo-EM structure of PSI protomer was superposed with X-ray structures of PSI (PDB ID: 1JB0) based on the PsaA subunit, displacements of α-carbon atoms beyond 0.7 Å appeared also not only in the stroma side but also in luminal side. Even the structure of Cyt c_6 was not visualized in the luminal side, the PsaB and PsaF were structurally perturbed upon binding of Fd to be suitable for Cyt c_6 binding. This may be a signal to activate the non-productive secondary binding site for Cyt c_6.

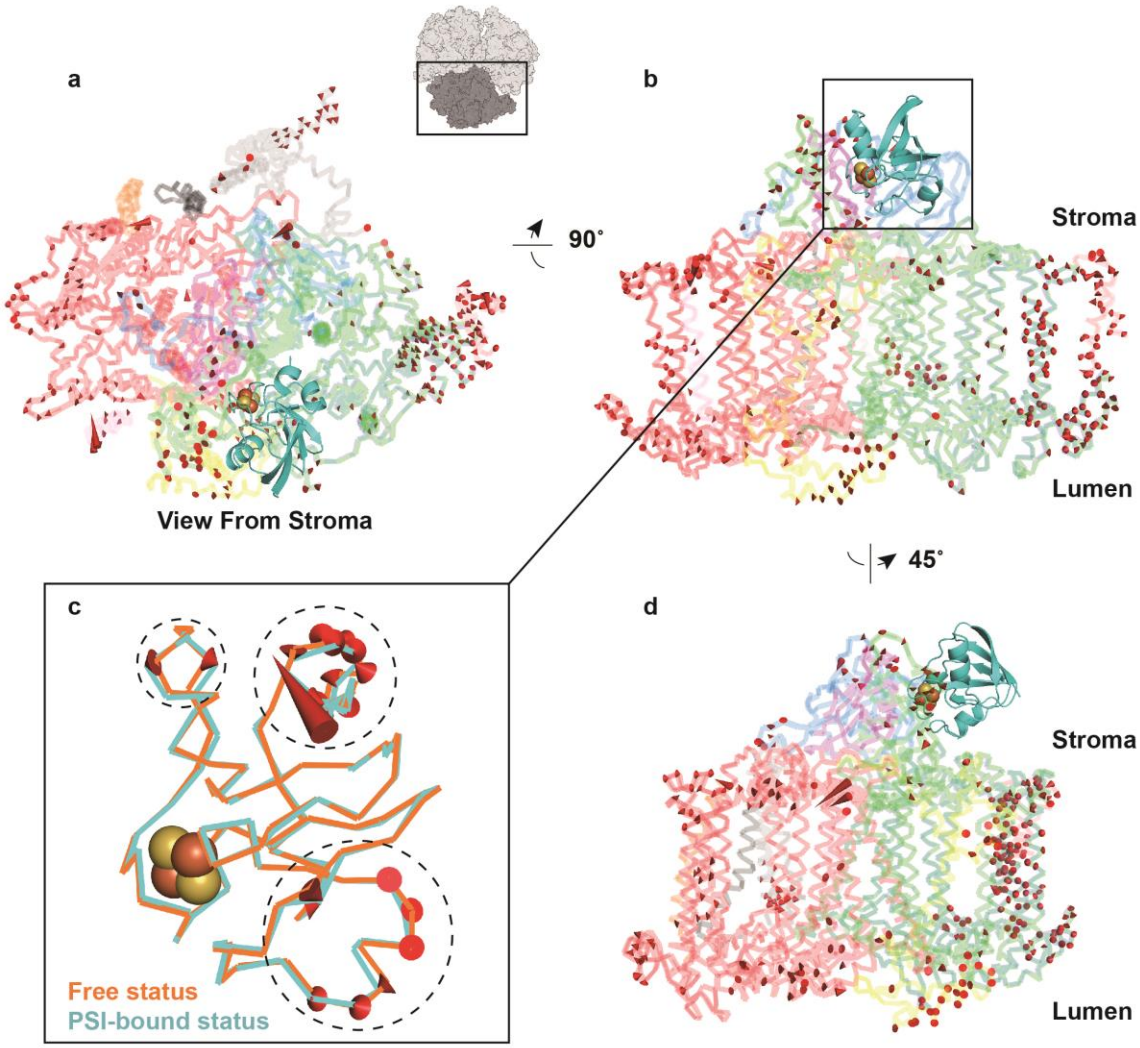

Figure 3-29 Structural comparison between binding and free status of PSI (**a**, **b** and **d** from three views) and Fd (**c**). Atomic model of free PSI trimer (in monomer form, PDB ID: 1JB0) and free Fd (PDB ID: 1AUI) were superposed based onα-carbon of core coordinates (PsaA and PsaB for PSI; 30-80 amino acids for Fd). Red arrows show displacements beyond 1 Å.

One surprise for us is that six water molecules mediated hydrogen bonds between Fd and PSI (**Fig. 3-26**). Before complex formation, each of Fd and the stroma subunits of PSI must be hydrated by solvent. After forming the specific e-transfer complex between Fd and PSI, hydrated water molecules except for remaining six waters looked excluded

from the interface. To conform the thermodynamic insights of complex formation including hydrated water molecules, the isothermal titration calorimetry (ITC) measurement was performed. Based on the analysis results of thermodynamic parameters, Fd-PSI complex formation was Fd-FNR and Fd-GmHO type ($\Delta H>0$ and $\Delta S>0$) but not the Fd-SiR type ($\Delta H<0$ and $\Delta S>0$). The Fd may use entropy in binding to its partner protein (in this case, PSI). Attractive electrostatic interactions, polar interactions, and Van der Waals' force-driven interactions may contribute to negative ΔH ($\Delta H<0$), however, detachment of water bound to interfaces for complexation will cost thermodynamically ΔH, and thereby producing a positive value of the net ΔH ($\Delta H>0$), as observed in the Fd-FNR complex formation. On the other hand, dehydration of water molecules and increases in conformational entropy would increase the entropy change. Additionally, strong interprotein affinity between GaFd and PSI was detected with K_d value of approximately 0.8 mM, which approximated the affinity of native Fd to PSI measured by flash-absorption spectroscopy. Last but not least, the binding stoichiometry (n value) of approximately 3 suggested that one GaFd binds to one PSI monomer in solution, which was consistent as the Cryo-EM density map and atomic model presented.

In this chapter, we described the Cryo-EM single particle analysis result of cyanobacterial photosystem I complex in presence of Cyt c_6 and GaFd. The proteins were simply mixed without covalent cross-linking, and incubated in dark before Cryo-EM grid making. The major architecture of PSI is in symmetry of C3, so C3 symmetry was applied to Cryo-EM density map during auto-refinement, which leaded to a higher overall resolution (2.06 Å in C1 map, and 1.97 Å in C3 map). The better resolution benefited from three major aspects: the protein samples with high purity and homogeneity, optimized membrane protein complex preparation method GraDeR[94], and highly advanced microscope equipment (JEOL CryoARM300 with a field emission gun and Gatan K3 Summit detector).

Density map in C3 symmetry was used for modeling since some ligands presented more traceable shape in C3 map. Photosystem I trimer crystal structure derived from *Synechococcus elongatus* (PDB ID: 1JB0)[36] at resolution of 2.5 Å was used as starting model for modeling building and comparison. Total 40 amino acids distributed in 4 subunits (5 in PsaA, 1 in PsaB, 33 in PsaK and 1 in PsaL) and 3 ligands (J4017, K104, A6001) were newly deployed in new model based on visible densities. Representative molecules overlapped with density map were presented in **Fig. 3-16**. Some previous partially-modeled ligands were completed (such as B4009 in **Fig. 3-16b**). One of chlorophyll in special electron transfer chlorophyll pair P700 (A1011) was remodeled as chlorophyll A isomer (PDB chemical components ID: CL0, **Fig. 3-16a**). The 143th amino acid residue in subunit PsaL was modified from Leucine to Serine based on Uniprot sequencing result (UniProtKB - Q8DGB4) and corresponding density map (**Fig. 3-16g**).

One noteworthy thing was that several stick-shaped densities were found inserting between each PSI monomer, indicating the stable packing of lipids. Before our model described in this article, only lipids embedded inside of PSI were assigned in PsaA and PsaB (including 3 phospholipids and 1 galactolipid). Thylakoid lipidome contained various lipids including but not limited to PG (phosphatidylglycerol), MGDG (monogalactosyldiacylglycerol), DGDG (digalactosyldiacylglycerol) and SQDG (sulfoquinovosyldiacylglycerol)[109]. Inter-monomer lipids were not determined by type since the densities of head groups were missing, which indicating their relative flexible movements outside of the thylakoid membrane. After excluding the densities which easily confused with chlorophyll phytol chains and densities with less convincing direction and too short length, still 17 fatty acid molecules between each PSI monomer were kept in our model. The visible fatty acid chains held close distance with hydrophobic amino acid residues and antenna ligands (chlorophylls and β-carotenes), indicating the potential function for stabilization of PSI trimerizaiton.

Ferredoxin was modeled based on density map at local resolution around 2.4 Å. Density of Fd redox center [2Fe-2S] (in our case, [2Ga-2S]) can be clearly visible and modeled. Homologous crystal structure of Fd (PDB ID: 5AUI) was used as starting model for fitting and refinement. In our model, Ga-substituted Fds (GaFd) were prepared as non-functional electron acceptor of PSI, since [2Ga-2S] redox center could not be reduced by terminal electron transfer partner F_x in PSI, whereas the structure of GaFd was almost identical to native Fd[80,81]. So the redox status of the structure was definite and clear, namely protein complex of PSI binding with pre-reduced Fd. To investigate the binding details between Fd and PSI, DIMPLOT program[111] was performed for quantitative analysis based on the refined complex model. Some differences was found when compared with previous PSI-Fd complex crystal structure[82], which had been described in Result part.

Structural changes were visualized by PyMol script modevectors.py. Model of PSI trimer part (shown as monomer since both models are in C3 symmetry) was superposed with 1JB0 model in simplified α-carbon form. Superposition was performed based on the overlapping of PSI core subunit PsaA, which was proposed as immobile center during electron transfer. Ferredoxin structural change comparison was also performed by superposing Fd part with previous Fd crystal structure (PDB ID: 5AUI, resolution 1.5 Å). Displacements of α-carbon beyond 0.7 Å were shown by red arrows in **Fig. 3-29**.

Author	Publish year	Protein	Organism	Mutation site (Corresponding residue in 7FIX)	Method	Potential influence
Jonathan Hanley et al	1996	PSI PsaD	Synechocystis 6803	H97 (H95), K106 (K104), R111 (R109)	Flash-absorption spectroscopy	Fd binding affinity with PSI
Nicolas Fischer et al	1998	PSI PsaC	C. reinhardtii	**K35 (K34)**	Flash-absorption spectroscopy Electron paramagnetic resonance spectroscopy	Fd binding affinity with PSI
Tetsuyuki Akashi et al	1999	Fd	Z. mays	E93	Cyclic voltammetry	Fd redox potential
Tetsuyuki Akashi et al	1999	Fd	Z. mays	D66, **D67**	Affinity chromatography	Fd interaction with FNR and SiR
Nicolas Fischer et al	1999	PSI PsaC	C. reinhardtii	D9 (D8), **I12 (I11)**, T15 (T14), **Q16 (Q15)**	Flash-absorption spectroscopy Electron paramagnetic resonance spectroscopy	Fd binding affinity with PSI
Patrick Barth et al	1999	PSI PsaE	Synechocystis 6803	**R39**	Flash-absorption spectroscopy	Fd binding affinity with PSI
Bernard Lagoutte et al	2001	PSI PsaD	Synechocystis 6803	R111 (R109)	NADP+ Photo-reduction Assay Flash-absorption spectroscopy	Fd binding affinity with PSI
Herve Bottin et al	2001	PSI PsaD	Synechocystis 6803	D100 (D98), E105 (E103), E109 (K107)	Flash-absorption spectroscopy	Fd binding affinity with PSI
Pierre Setif et al	2002	PSI PsaC	T. elongatus	**K34**, G36	Flash-absorption spectroscopy	Fd binding affinity with PSI
Hisako Kubota-Kawai et al	2018	Fd	T. elongatus	**Y24, E31, D61, D67,** E71, Y81, E93, **Y97**	Flash-absorption spectroscopy	Fd binding affinity with PSI

Table 3-3 Summary of site-mutation tests on PSI subunits or Fds and their influences. Mutation sites colored in red are Fd-binding related residues found in the structure described in this chapter.

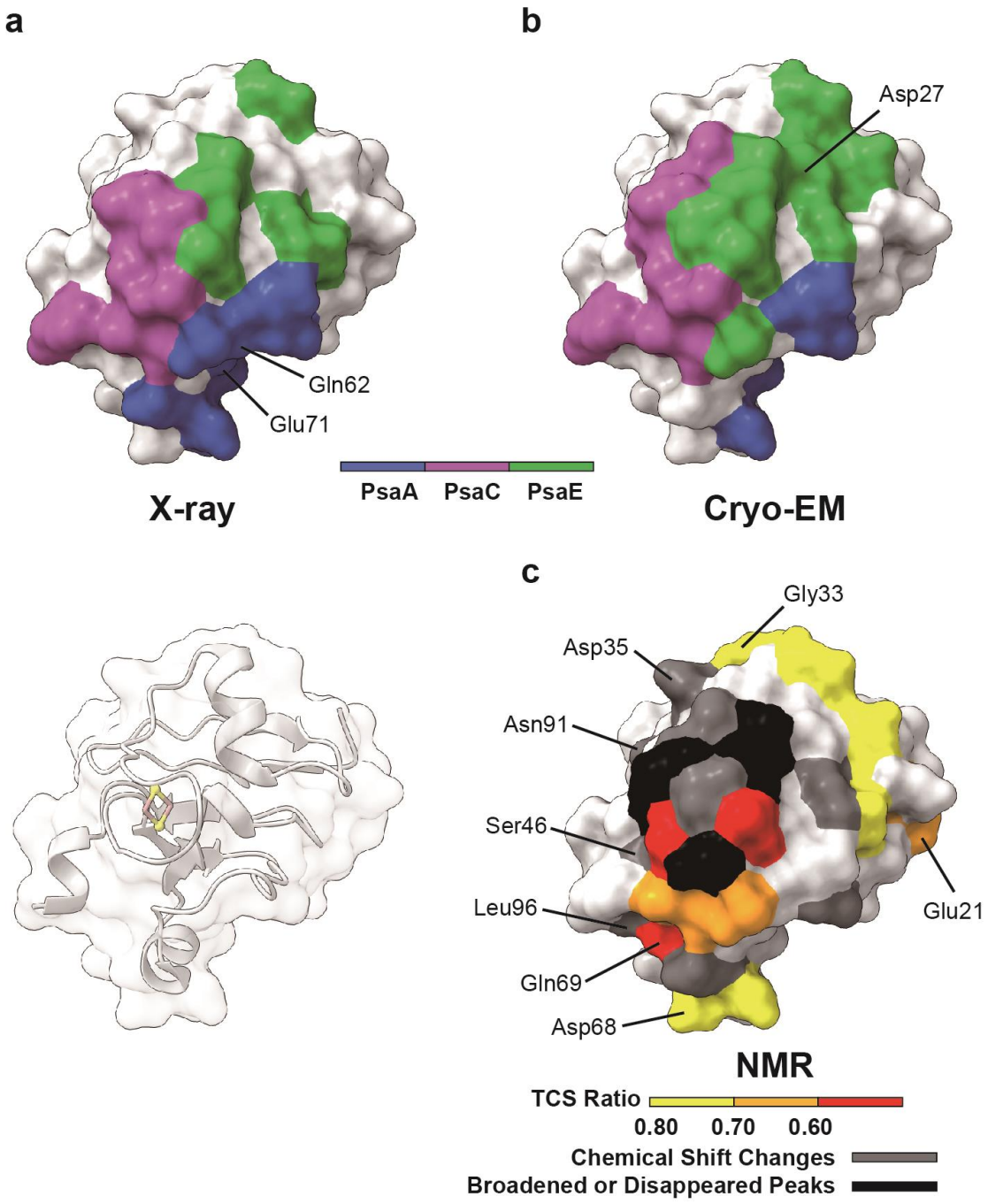

Figure 3-30 Bonding-related residues of Ferredoxin detected by X-ray, Cryo-EM and NMR.

The Cyt c_6-like extra densities in our structure were found around the N-terminal of PsaF (See **Fig. 3-18**). The detailed binding orientation of Cyt c_6 could not be determined as the result of limited local resolution. This density blob was not present in the density map of PSI-only Cryo-EM datasets (not published), so it was treated as potential Cyt c_6 binding site although far from primary electron transfer acceptor P700 in PSI trimer. This is the first time that additional Cryo-EM densities around cyanobacterial PSI in lumenal side are being observed, although many previous attempts, such as covalent crosslinking of PSI and Cyt c_6 have been made[68]. Cryo-EM structure of PSI-Pc-Fd triple complex[89] revealed recently showed plastocyanin different binding mode, in which plastocyanin was closely binding to PSI with a hydrophobic binding surface created by PsaA and PsaB.

Electron transfer kinetic analysis results from green algae and higher plants indicated bi-phasic features[105,107]: the fast electron transfer phase relevant to the reduction of P700, whereas the slow phase was responsible to the diffusion time of Pc/ Cyt c_6 in the lumenal space to PSI centers. The structural basis of such kind of bi-phasic reaction was assigned to the Lys-rich N-terminal of PsaF. This protein region offered electrostatic interaction sites to electron donor protein, and played key role of guiding them into P700 reaction center[104]. The heterogeneous cross-linking result and kinetic features[112] indicated the existence of both activate and inactivate binding site. The cross-linking test performed in *Chlamydomonas reinhardtii* showed similar result[107]: almost all Cyt c_6 were bound with PsaF with a stoichiometric ratio of 1:1, and not bound with other subunits of PSI when PsaF was absent. Only 33% of Cyt c_6 performed fast electron transfer to P700, whereas other 67% inactive cross-linking indicated the existence of potential extra binding site. Such kind of binding site may be far from active site, but guarantee continuous fast electron transfer. However, not all cyanobacterial PsaF have the pre-binding structural basis as in green algae and higher plants, and the existence of fast phase in cyanobacteria was still with debate[106]. Recently, in vivo P700

reduction kinetic study derived from cyanobacteria Synechocystis sp. PCC6803 presented similar features as green algae and higher plants[108]. Around 60% of PSI reaction centers were with electron donor bonded, which caused fast re-reduction after charge separation event. This result indicated electron donor (both Pc and Cyt c_6) could form pre-binding complex with PSI, and realize fast electron donation after P700 was excited.

Another notable thing is, there were 23 residues at N-terminal of PsaF that were not able to be modeled (in neither 1JB0 nor our model). Since we gene modified N-terminal of PsaF by adding 10x histidine tag for purification of PSI, the successful purification by nickel-NTA column chromatography indicated this region was kept intact in the final protein sample. This region contained two positively charged residues (2R, 3R), and this number will increased to 12 when taking the His-tag into account. The increasing of positively charged residues may offer extra binding sites to negatively charged Cyt c_6, just similar as pre-binding complex forming in green algae and higher plants. From this aspect, N-terminal with his-tag may have higher affinity than wildtype, and accidentally occurred the similar pre-binding mechanism in eukaryotic phototrophs. However, potential influence caused by adding of his-tag on the relevant electron transfer kinetics was not clear yet. Therefore we did not include Cyt c_6 into atomic model deposited to PDB, only present possible docking region in **Fig. 3-18c**.

Although the protein mixture was incubated in cold and dark environment, we did not avoid exposure to light during cryo-grid preparation. This experimental set-up should imply that fast charge separation driven by photon forced P700 to continuously be in the excited state (P700*) and the transferred electron to be quenched since GaFd could not accept it. However, P700* as a strongly activated site will oxidize Cyt c_6 in short time. The possibility of all Cyt c_6 were oxidized could not be excluded when take high turnover rate of PSI to Cyt c_6. In the density map, the density region was far from P700 activate site

(around 55 Å center-to-center distance from P700 to Cyt c_6-like density), which had obvious difference with resent resolved PSI-Pc binding region[89].

Even though masked 3D classification and auto-refinement was performed to the area covering Cyt c_6-like densities, the relatively low local resolution (worse than 4 Å) made it hard to perform accurate orientation. The limited resolution was caused by two possible reasons. First, that Cyt c_6 is quickly oxidized by PSI in the presence of light, and that oxidized Cyt c_6 prefers to detach from PSI for binding of the next reduced Cyt c_6. Such kind of “pre-escape” intermediate complex may lack stable interaction, or interactions might be not even specific, resulting in the current “noisy” but still visible density. As a side evidence, the dissociation constant of oxidized Pc is about six times larger than that observed for reduced Pc[105]. Even in case of Cyt c_6 not being oxidized, the affinity of pre-binding with PSI is also weak when compared with Pc[108], which results in diminished visibility. A second possibility is that, such kind of binding status occurs in only a small proportion of PSI, resulting in the limited occupancy rate at this region, and in turn not enough signal during data processing. Although we tried to enhance the local signal by masked 3D refinement/classification as well as partial signal subtraction during image processing (result not shown), the visibility of this region was not improved remarkably. In a previous study, single particle Cryo-EM was combined with masked masked 3D refinement and cross-linking of PSI and Cyt c_6 from same species[68]. However, no density was detected at Cyt c_6-related region. Here we made a preliminary description of this intermediate complex, although more detailed information could not be determined based on our Cryo-EM density map. Also, the redox status of Cyt c_6 in the complex will have to be revealed by further kinetic measurements.

Chapter IV. Purification of PSI surrounding with IsiA antenna ring

4.1 Introduction

4.1.1 The survival dilemma of cyanobacteria caused by iron deficiency

Cyanobacteria are major contributors of our biosphere who made comprehensive influence to the present geochemical status of the Earth, effectively shaping our planets environment. On the other hand, changeable environmental parameters also affect the cellular homeostasis of organisms including cyanobacteria. To adapt to abiotic stresses, cyanobacteria applied various strategies such as production of stress-induced proteins, differential regulation of specific genes and metabolic pathways shifting[113,114]. In general, numerous factors including extreme temperature, drought, pesticides, salinity, heavy metals, metalloid and ultraviolet (UV) radiation could affect cyanobacterial cell growth and metabolism[115–119].

Iron is an essential metal element in most organisms, which mainly exists in its ferrous (Fe^{2+}) or ferric (Fe^{3+}) form in nature. With the reason of Ferric iron's lower solubility at current oxygen-rich natural environment, the bio-availability of iron decreased a lot from anaerobic to aerobic environment. The Great Oxygenation Event (GOE) was thought as the main reason for the increased difficulty in obtaining iron. Many life forms had to adjust their survival strategies in order to adapt to a new environment deficient in iron. In cyanobacteria, numerous enzymes involved in nitrogen metabolism, photosynthesis and respiration contain iron[120], which is one of the reasons why cyanobacteria require more iron than heterotrophic organism for surviving. Iron also serves as a cofactor of mobile electron transfer carriers such as ferredoxin[121], as a result, the iron requirement of cyanobacteria is at least tenfold of that of non-photosynthetic bacteria of similar size[122].

In fact, iron deficiency is one of the major limiting factors for oceanic primary productivity[123], even though iron is the fourth most abundant element in the earth's crust. The dissociative concentration range of iron was from 10^{-9} to 10^{-18} M in which most

cyanobacteria live, however, at least 10^{-8} M iron could enable basic survival and growth, and at least 10^{-7} to 10^{-5} M is required for optimal growth[120]. Some nitrogen-fixing cyanobacteria have larger iron requirement than others, since most of the nitrogen fixation-involved enzymes need iron as cofactors[124].

Even though iron played important role in cyanobacterial physiology, excess intracellular iron would also cause adverse effect by producing reactive oxygen species (ROS) through the Fenton Reaction[125]. Meanwhile, iron deficiency would also cause similar damage which was termed as oxidative stress[126]. Therefore, rigorous adjustment of iron uptake and metabolism is compulsory to ensure appropriate iron supply and concentration[127,128].

4.1.2 Cyanobacterial coping strategies under iron-limited conditions

Various strategies were formulated for stabilization of this indispensable element in cyanobacteria. Comprehensive changes happened at gene transcription level, which lead to rearrangement of photosynthesis mechanism and the appearance of iron absorbing induction[129]. The transcription of many related gene, such as siderophore (small, high-affinity iron chelating compounds secreted by microorganisms) biosynthesis involved enzymes, TonB-dependent outer membrane transporters, periplasmic ferric-binding proteins and ATP-binding permeases, were depended on the bio-availability of iron[127,130,131].

The global modulation of iron stability was controlled by transcriptional regulatory factor named Fur, which was short for Ferric uptake regulator[132,133]. In general, Fur served as repressor of transcription and sensed endocellular iron concentration and regulated transcription according to the iron bio-availability[120]. The Fur regulation not only controls iron uptake and the expression of storage system, but also commands comprehensive gene and operon. Such connection could combine iron bio-availability to cyanobacterial physiological process[126,133–135].

The typical strategy of overcoming iron starvation for cyanobacteria included two approaches, the up-regulation of iron acquisition systems and the cutting down or substitution of related molecules. In terms of physiology, the response types can be classified into three types: the retrenchment, compensation and acquisition[136]. The retrenchment included reduction of cell size, loss of phycobilisomes (light harvesting antennae of Photosystem II), ultrastructural changes and pigment changes. The compensation was performed by flavodoxin synthesis, which playing ferredoxin role, and the expression of isiA gene. As for the acquisition, cyanobacteria induce iron acquisition systems in the case of iron stress conditions. The adaption of iron deficiency also requires many gene modifications of other metabolic pathways, some of which have no direct connection to iron metabolism, such as respiration, photosynthesis, nitrogen metabolism, tricarboxylic acid cycle, glycolysis, antioxidant defense as well as amino acid and toxin synthesis[127,137]. The iron stress threshold is also considered as an influence factor to various cyanobacterial responses, which could be described as moderate, severe or extreme.

As described above, the photosynthetic electron transfer chain would be rearranged by influence of iron starvation. Many photosynthetic proteins contain iron as cofactors, which is also essential for catalyzing the synthesis reactions of chlorophyll. To some extent, iron deficiency is equal to the decrease of linear photosynthetic electron transfer and the strengthening of respiratory electron transfer[138]. Moreover, the connection between oxidative stress and iron deficiency had been elaborated, which would cause adverse effect to photosystems[126,139]. Some genes involved to photosynthesis and anti-oxidation were regulated by iron bio-availability, which had been determined in previous researches[127,133,140].

4.1.3 The *isiA* and *isiB* gene

In all known iron-induced genes, the products of isiAB gene played key roles in the

adaptability of the photosynthetic molecular machine to realize better performance at low iron concentration[132]. In some cyanobacteria, the isiAB operon is transcriptionally regulated to be expressed in case of iron stressed condition, and dicistronic form of isiAB transcripts were not as abundant as the monocistronic isiA transcripts[141]. The chlorophyll bound product of isiA was first described in *Anacystis nidulans*[142]. The character of its conferring adaptation to photosynthetic molecules was also found in case of iron deficiency. Because of its high homology with the CP43 protein in Photosystem II, this protein was initially termed as CP43' [141] and treated as part of additional light capture complexes[143]. However, further investigations revealed several roles of IsiA and are proposed and summarized[144] as:

(1) IsiA serves as a chlorophyll storage protein for subsequent quick iron recovery[145].

(2) IsiA acts as an excitation energy dissipater to protect PSI and PSII from optical damages[146].

(3) IsiA functions as extra antennas for light-harvesting in both PSI and PSII[143,147].

(4) IsiA replaces CP43 in PSII and performed cyclic electron transfer between PSII and Cyt b_6f[148,149].

Notably, not all cyanobacteria contain the isiA gene, and no isiA homologs were found in higher plants. The fact of isiA gene presenting in iron-limited, high-nutrient and low-chlorophyll regions indicates that the existence of this gene could be treated as a biomarker for iron limitation in oceanic environments[150].

Besides isiA, the isiB gene encodes a small FMN-flavoprotein called Flavodoxin (Fld). The transcription of Fld gene is independent from the isiA, and located in a different locus in some filamentous cyanobacteria[151]. Fld serves as reducing power by cyanobacteria and, as a result, enables the stable utilization of light energy during iron starvation. In case of iron deficiency, the synthesis of the Fd (which contains an iron-sulfur cluster) is repressed[152]. Meanwhile, Fld is induced as substitutes and replaced Fd for electron transfer in various reaction pathways in which Fd participated, but these pathways not

included electron transfer chain of nitrogenase in heterocyst[153–156]. The importance of Fld to cyanobacterial iron deficiency adaption is indispensable and consequently cyanobacteria lacking Fld synthesis ability are particularly affected[152]. Even though Fd and Fld are isofunctional proteins, interestingly no distinguishable similarity in primary, secondary or tertiary structures was detected. These two proteins could interact effectively with the identical electron transfer partners and presented similar kinetics constants although Fld appears to be slightly less efficient when compared with Fd[155,156].

4.1.4 The IsiA antenna ring of PSI

Some kinds of cyanobacteria such as *Synechocystis* sp. can form a membrane-embedded antenna ring around the trimeric PSI complex under the condition of iron deficiency, whose observation was firstly reported in 2001[157,158] (Shown in **Fig. 4-1**). The major component of the antenna ring is CP43', which is encoded by the "iron-stress-induced" gene isiA, showing significant homology with one of the membrane-embedded chlorophyll a-binding antenna protein (CP43). Low-resolution projection map of the CP43'-PSI complex have been plotted based on the electron micrographs of the supercomplex[159], which fitted well by docking the independent X-ray structure of PSI trimer with eighteen CP43 proteins. However, the mechanism of efficient energy transfer from CP43' to PSI has been impeded by lack of more detailed structural information, especially the relative positions of light capturing pigments within the complex such as chlorophylls or carotenoids. Although the low-resolution electron microscopic 2D projection map is available, the high-resolution structure through protein crystallography are important for studies of structure-function relationship in order to analyze the mechanism of energy transfer within the CP43'-PSI supercomplex.

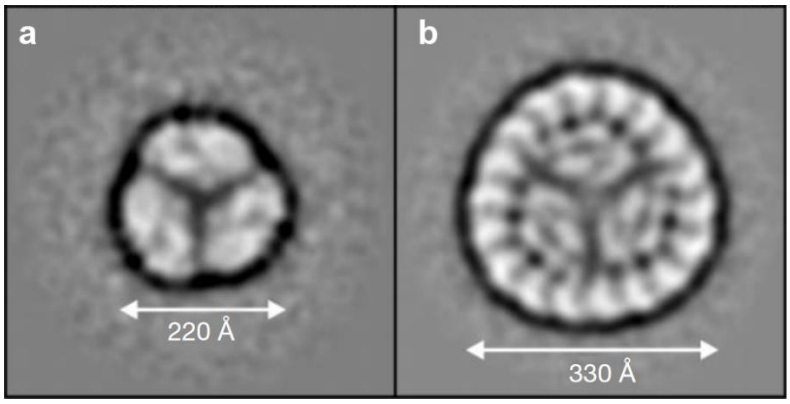

Figure 4-1 The image-processed top views of negatively stained PSI trimers (a) and CP43'-PSI complexes (b)[158].

4.1.5 Research motivation and target

In this chapter, in order to analyze the influence of iron limited cultivation condition to the cyanobacterial PSI, thermophilic cyanobacteria *Thermosynechococcus elongatus* (*T. elongatus*) BP-1 was cultured in Iron-deficient growth environment. We tried to purify the supercomplex of PSI together with additional IsiA antenna rings using comprehensive strategies and extensive optimization.

4.2 Materials and Methods

4.2.1 Cell cultivation

To create Iron-deficient growth environment for cyanobacteria cells, the composition of the standard cyanobacterial cultivation medium BG11 was modified as described below and listed in **Table 4-1**. Ammonium ferric citrate, whose chemical formula as $(NH_4)_5[Fe(C_6H_4O_7)_2]$, was omitted to induce the expression of IsiA. Initial trials of cultivation were performed with the strategy of keeping iron-deficient status throughout all processes. The color of culture solution turned to be yellow from dark green at late stage of large scale cultivation as **Fig. 4-2** presented. Almost identical results appeared if cells were kept culturing in 100 mL flasks for long time (>14 days). Following thylakoid membrane extraction and protein purification failed when using cells harvested from

yellow culture solutions, which indicated long-term iron-deficient cultivation was not suitable for this cyanobacterial strain.

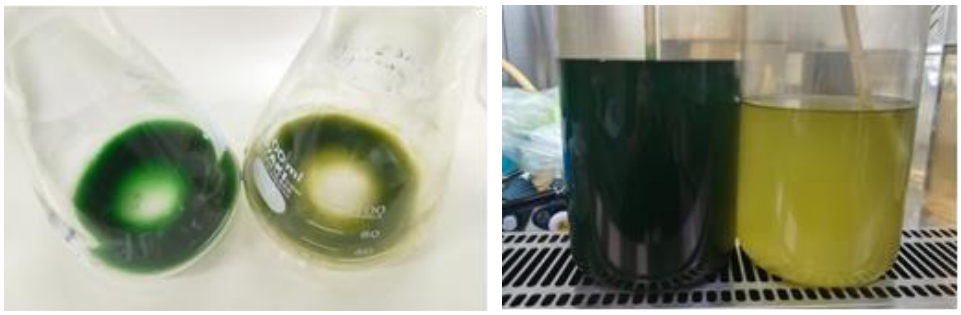

Figure 4-2 Compare of culture solution in normal BG11 medium (left flask/bottle) and long-term (>2 weeks) iron-deficient cultivation (right flask/ bottle).

Cell cultivation strategy was optimized by using normal BG11 medium which containing soluble iron for cell-growing stage of cultivation from solid cultivation to middle stage of liquid cultivation. After cultivation in middle stage with normal BG11 medium, cells were separated from culture solution by centrifugation (2000 g, 2 min at 20 ℃) and washed by sterilized Iron-free BG11 medium two times. Cells after medium exchanging were seeded into 2 L cultivation bottles containing Iron-free BG11 medium. Cultivation was performed under continuous illumination at 30 μM photons m^{-2} s^{-1} at 50 ℃ with 2% (v/v) CO_2 aerated in air.

The complete cultivation procedure is depicted in **Fig. 4-3** for easier understanding. In general, solid culture was performed in plates containing solid BG11 medium (with 15 g/L Agar powder in medium) for around one week. After solid cultivation, cells were washed off by liquid BG11 medium and seeded into 100 mL flasks containing 50 mL BG11 medium. For the whole culture process, temperature was stabilized at 50℃ and by illumination was realized by incubator (Panasonic MLR-352). During early and middle stage of liquid cultivation, rotary shaker (TAITEC NR-2) was used to prevent cell

precipitation and aggregation with a shaking speed of 120 rpm. Magnetic stirring was performed during late stage of liquid cultivation in 2 L bottles by NISSIN SLQW SW600 N-1 stirrer. The continious bubbling of 2% CO_2 was offered to culture bottles by a MVP-751 pump from Asahi Techno Glass and a Hitachi oil free Bebicon compressor.

SOLUTION NAME	INGREDIENT	AMOUNT (g/L)
Stock 1 (100x)	Citric acid ($C_6H_8O_7 \cdot H_2O$)	1.312
	EDTA·Na_2	0.2
Stock 2 (1000x)	$MgSO_4 \cdot 7H_2O$	150
Stock 3 (100x)	$NaNO_3$	300
	K_2HPO_4	7.8
Stock 4 (1000x)	$CaCl_2 \cdot 2H_2O$	76
Stock 5 (1000x)	Na_2CO_3	40
Stock 6 (1000x)	H_3BO_3	5.72
	$MnCl_2 \cdot 4H_2O$	3.62
	$ZnSO_4 \cdot 7H_2O$	0.44
	$Na_2MoO_4 \cdot 2H_2O$	0.78
	$CuSO_4 \cdot 5H_2O$	0.16
	$Co(NO_3)_2 \cdot 6H_2O$	0.1
Stock 7 (100x)	HEPES（pH 7.5）	190

Table 4-1 Modified BG11 medium stock solutions for cultivation

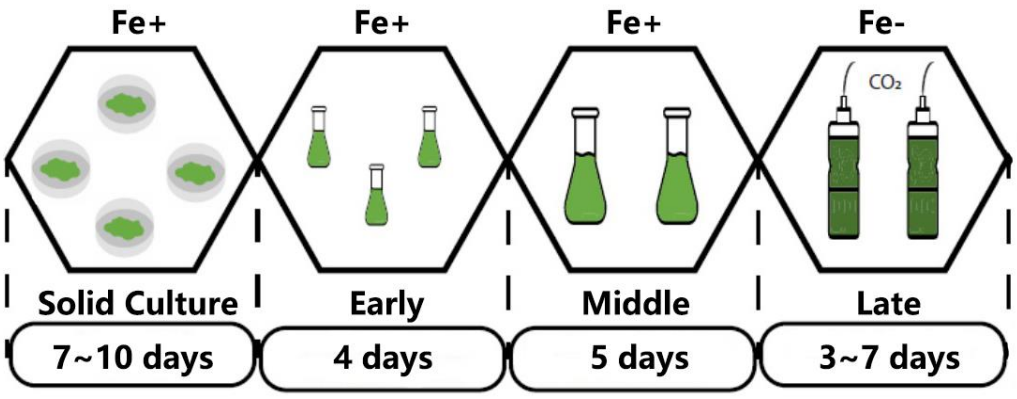

Figure 4-3 Optimized cultivation strategy in Iron-deficient condition

4.2.2 Cell disruption

Beads-Beating (BB), Osmotic Shock (OS) and Parr Bomb (PB) were performed for cell disruption test according to previous protocols. Performance was evaluated in aspect of membrane protein sample yield and quality. After cell disruption, insoluble cell contents containing thylakoid membranes were separated by ultracentrifugation (40,000 g, 30 min at 4℃, P50AT2 rotor, HITACHI himac CP80WX). Precipitant was collected and dissolved in buffer containing 20 mM MES (pH 6.5), 20 mM $CaCl_2$, 20 mM $MgCl_2$ and 2% (w/v) glycerol. As a result, Osmotic Shock was selected as optimal cell disruption method since best yield and mild thylakoid membrane treatment.

As for OS, minor modifications were performed in order to realize better yield and mild treatment. Cyanobacteria cells were collected from cultivation bottles after 7 days iron-deficient stress incubation by centrifugation (5000 g, 5 min at 4 ℃), and re-suspended in buffer containing 20 mM MES (pH 6.5), 20 mM $CaCl_2$ and 20 mM $MgCl_2$. Then centrifugation was performed again same as first step, and re-suspended cells in buffer containing 20 mM MES (pH 6.5), 20 mM $CaCl_2$, 20 mM $MgCl_2$, 0.5 M Mannitol, 1 mM EDTA·2Na and 2 g/L Lysozyme. The ratio of cells wet weight and Lysozyme buffer is 1g : 100 mL. After re-suspension, the mixture was incubated in a dark environment in a water bath for 1 hour at a temperature of 38℃. Gently shaking was performed during incubation to avoid agglomeration. Centrifugation was performed to separate cells from Lysozyme buffer after incubation, and cells was re-suspended into pre-cooled hypertonic buffer containing 20 mM MES (pH 6.5), 10 mM $MgCl_2$, 25% Glycerol, 1 mM Benzamidine and 1 mM α-aminocaproic acid. The volume of hypertonic buffer applied was one fifth of Lysozyme buffer. After gentle homogenization by a glass homogenizer, mixture was shock frozen by liquid nitrogen. Frozen cells could continue disruption as followed, or stock in -80℃ refrigerator.

After melting at room temperature, mixture of cells with hypertonic buffer was poured into huge container (in case of 50 mL buffer, at least 2 L container should be applied) and

flooded into pre-cooled hypotonic buffer containing 20 mM MES (pH 6.5), 10 mM $MgCl_2$, 1 mM Benzamidine and 1 mM α-aminocaproic acid. The amount of hypotonic buffer is at least 30 times of hypertonic buffer.

4.2.3 Purification of PSI-IsiA supercomplex

At first, Ni-NTA Sepharose (Qiagen) column was applied for purification of PSI-IsiA supercomplex with the reason of PsaF subunit in PSI was with 10x his tag at N-terminal. Purification procedure was identical as described in section 2 for PSI trimer purification. After elution by buffer containing 100 mM Imidazole, protein sample was polished by Sucrose Density Gradient (SDG) centrifugation as **Fig. 4-4** presented. The SDG was performed identically as described at section 2 in detail. Several bands spread in 3 identical gradient tubes, while lower part (from B2 to B3 in figure) was hard to be separated. Two strategy was applied for checking the difference of this portion, which were stepped fraction (B1, B2 and B3) and continuous fraction (extracting successively from bottom to top with number as 1 to 21).

4.2.4 Optimization of PSI-IsiA supercomplex purification

Cultivation optimization trials were performed for determination of optimal cultivation condition. Many factors had potential influence on induction of IsiA expression and combining form of supercomplex including iron deficiency time and culture brightness. Cultivation was performed with different iron deficiency time (3 days, 5 days and 7 days) and brightness (10 and 30 μM photons m^{-2} s^{-1}). The effect of cultivation condition is described in detail in the discussion.

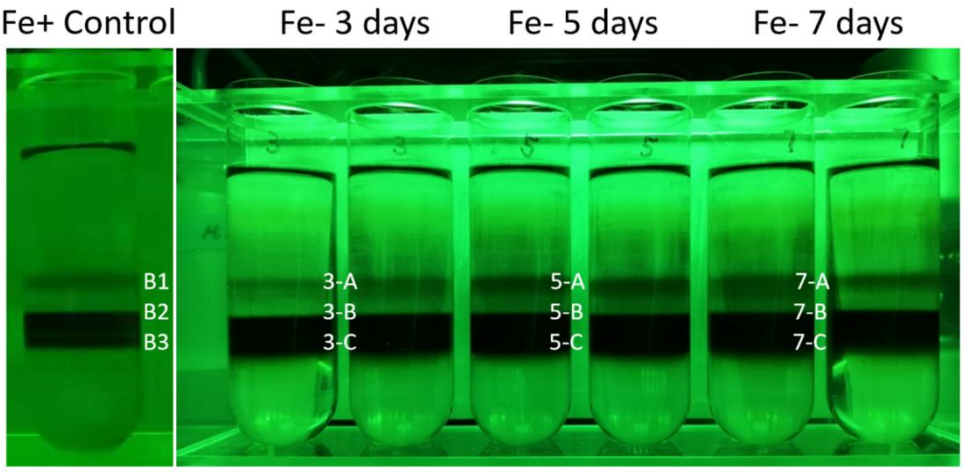

Figure 4-4 Compare of density gradient centrifugation results

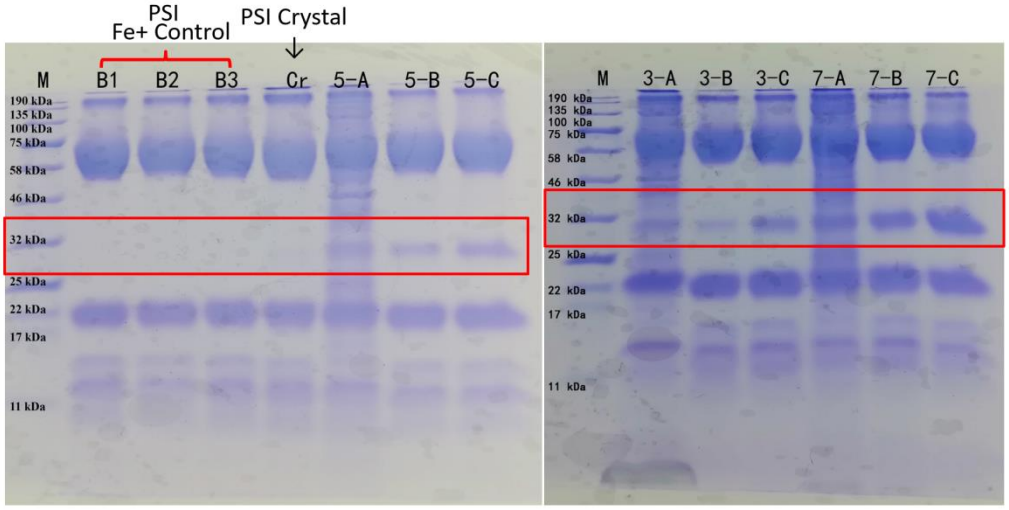

Figure 4-5 SDS-PAGE result of SDG bounds of samples purified from cells by Fe+/Fe- cultivation

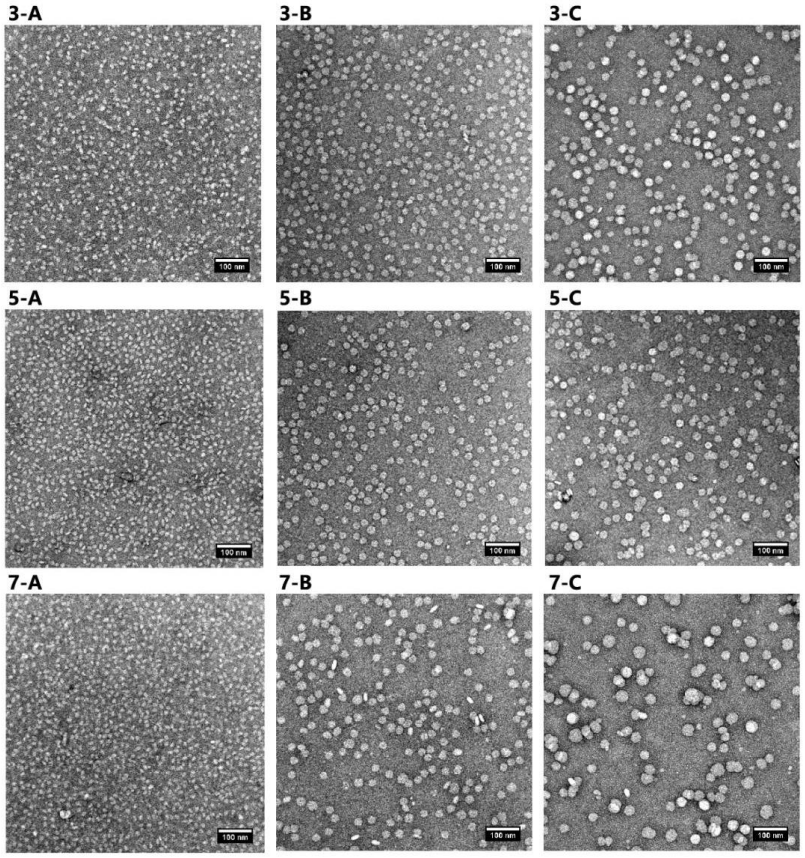

Figure 4-6 Negative staining results of each bounds from samples with different iron-deficient cultivation time

Purification method was optimized to improve the purity and homogeneity of supercomplex sample. Various purification strategies were performed to find the optimal purification procedure. Ni-NTA column was found not proper for supercomplex purification, since antenna IsiA proteins would be washed off from PSI trimer during purification based on compare the negative staining result of protein sample with/without Ni-NTA purification (**Fig. 4-7; 4-8**). In the subsequent purification trials, Ni-NTA purification step was therefore omitted even though it can separate PSI (including PSI-IsiA supercomplex) from other contaminant proteins effectively.

Figure 4-7 SDG result of samples with (left) /without (right) Ni-NTA purification

Gel filtration was applied to test its performance of purification. Size exclusion chromatography as performed by using HiLoad™ 16/600 Superose™ 6 PG, flow rate 0.5 ml/min and pre-equilibrated with buffer identical to protein sample. Negative staining results of typical fractions were presented in subsequent result section.

Density gradient centrifugation was applied to separate proteins into different bounds as **Fig. 4-9** showed. Meanwhile, trehalose and glycerol were also selected as alternative density gradient of sucrose for performance tests, which were reported as potential candidates in PSI-related supercomplex purification previously. Second round of density gradient centrifugation was performed to polish the extracted fractions from each tube (marked by red arrows). Protein samples extracted from second round density gradient (marked by yellow arrows) were checked by negative staining EM.

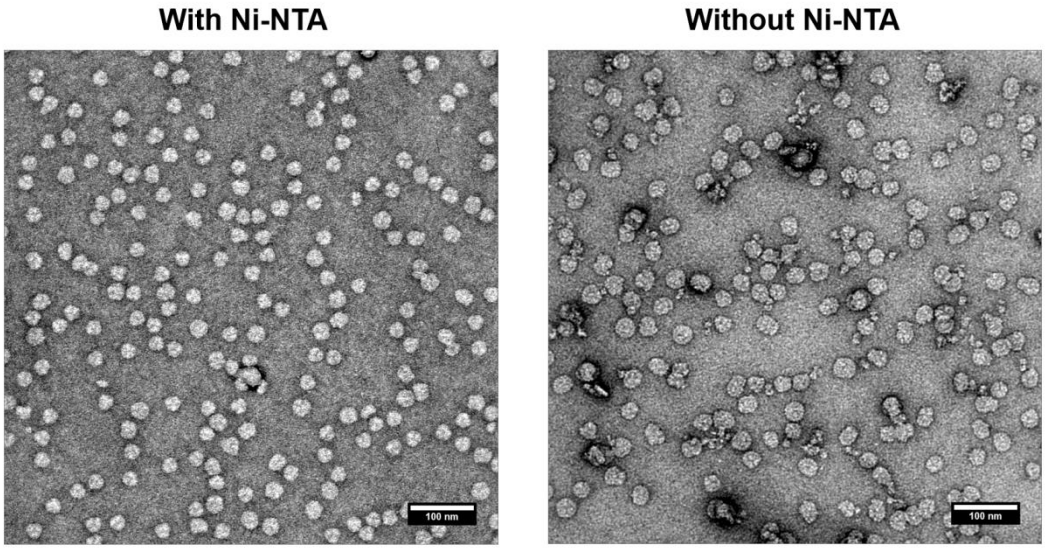

Figure 4-8 Negative staining results of PSI-IsiA supercomplex purification with/without Ni-NTA

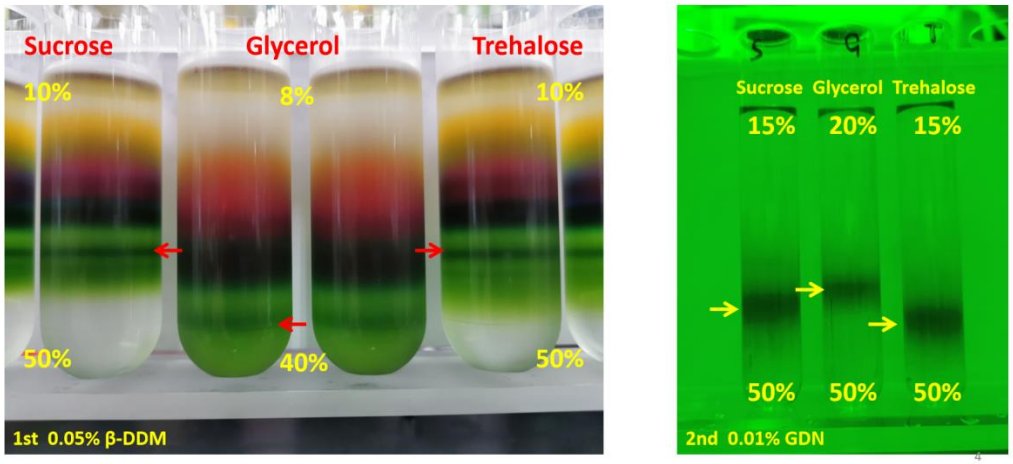

Figure 4-9 Density gradient centrifugation result in different mediums.

Some other aspects of purification details such as buffer optimization and concentration method optimization were also performed during each trial. The finalized optimal buffer contained 20 mM Tricine-NaOH (pH 7.5), 50 mM NaCl and 0.05% β-DDM. PEG precipitation was used to be applied for protein concentrating, whereas negative staining result of samples after PEG precipitation was not satisfying (**Fig. 4-10**).

Dimer-like aggregates (in red circles) appeared after PEG precipitation, and antenna IsiA protein detached from PSI trimer, which hindered the sample quality. Amicon15 ultrafiltration tubes (100 kDa MWCO) was used for ultrafiltration concentrating, and behaved well during PSI-IsiA purification at centrifugation speed of 3,000 g and 4℃, which was also be applied for buffer exchanging.

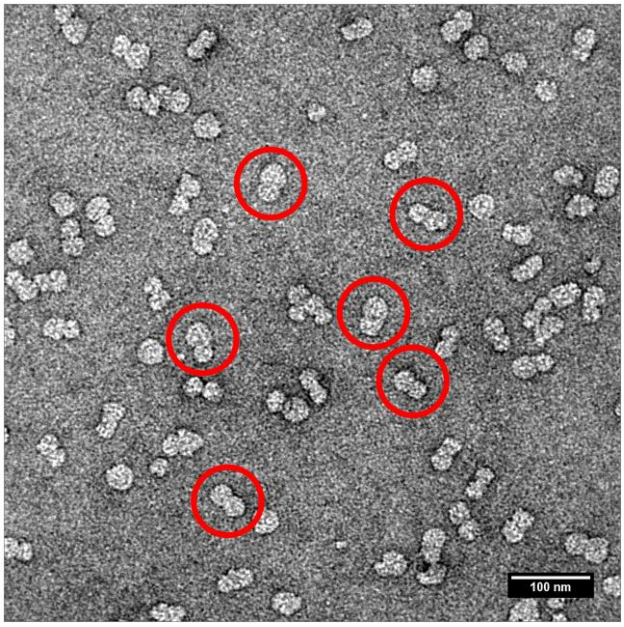

Figure 4-10 Negative staining result of PSI-IsiA samples after PEG precipitation

Detergent screening was also performed to find optimal solubilization condition. The n-Dodecyl-β-D-maltoside (β-DDM), lauryl maltose neopentyl glycol (LMNG) and glyco-diosgenin (GDN) were tested at proper concentration according to their critical micelle concentration (CMC), which were listed in **Table 4-2**.

Detergent	CMC	Purification	Negative staining	Cryo-EM
β-DDM	0.0087%	0.05%	0.02%	0.02%
GDN	0.0021%	0.01%	0.005%	0.005%
LMNG	0.001%	0.005%	0.002%	0.002%

Table 4-2 Detergent concentration in different working environments

4.2.5 Negative stain EM and SDS-PAGE

All bands from stepped fraction and typical fractions (3, 6, 9, 12, 15, 18 which marked by red arrows) were checked by SDS-PAGE and Negative staining EM. Negative stain EM was applied for morphological observation of protein complex particles. Staining and checking method were identical as described in detail at section 2. For PSI-IsiA supercomplex, Negative stain EM could obtain distinguishable information about antenna binding according to previous report about antenna binding polymorphism. SDS-PAGE was also performed identically as described at section 2 with the order of checking components distribution difference of each fraction/ band.

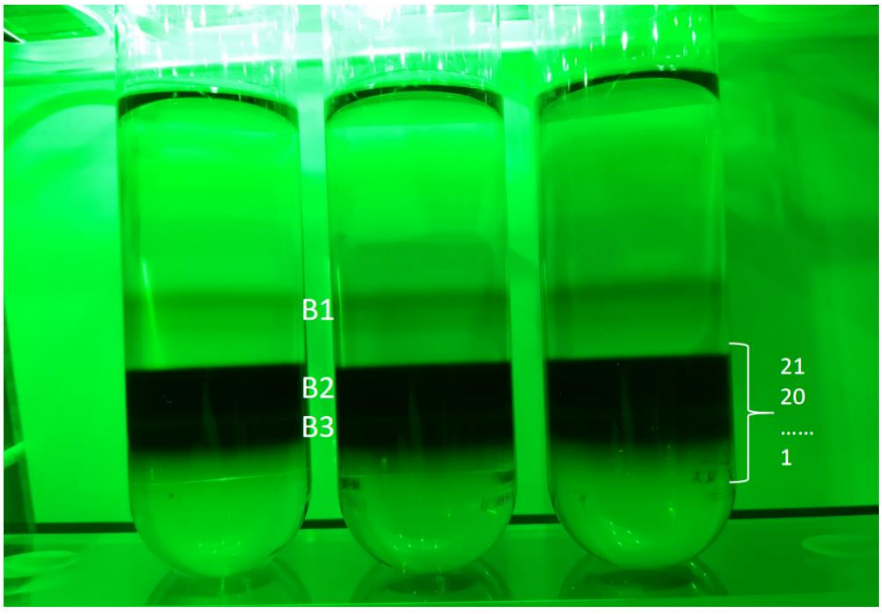

Figure 4-11 SDG result of PSI-IsiA sample after Ni-NTA column purification.

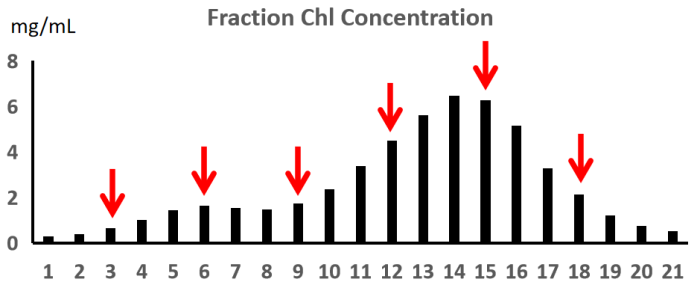

Figure 4-12 Chlorophyll concentration of each fraction extracted from gradient.

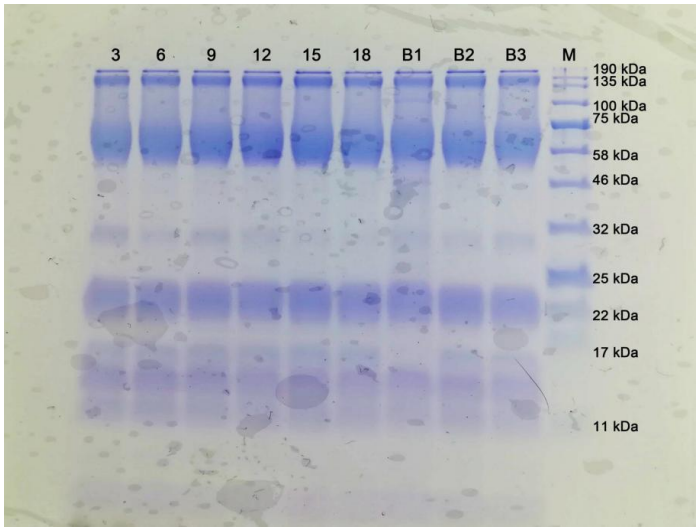

Figure 4-13 SDS-PAGE of stepped bands and typical fractions

4.2.6 Cryo-grids preparation and checking

Purified PSI-IsiA supercomplex sample was exchanged to buffer containing 75 mM NaCl, 30 mM Tricine-NaOH (pH8.0) and 0.005% GDN. A total 2.6 μL of sample at a chlorophyll concentration of 10 mg/mL was applied to a glow-discharged (JEC-3000 FC, 30 s, carbon support film facing up) Quantifoil cryo-EM grid (R 1.2/1.3 Cu 300 mesh) and plunge frozen in liquid ethane using a Vitrobot Mark IV (Thermo Fisher Scientific) fitted with Whatman #1 filter paper for blotting at 4 ℃ and 100% humidity for 3.5 s at blot force 0. Frozen grids were transferred to liquid nitrogen for storage, and checking was performed using a Talos Arctica (Thermo Fisher Scientific) transmission cryo electron microscope operated at 200 kV.

4.3 Results

4.3.1 Iron-deficiency cultivation results

Cultivation of BP-1 in medium lack of iron source (Fe-, here means ammonium ferric citrate in BG11 medium was removed) was performed after normal cultivation in flasks. Iron-deficient cultivation time was set as 3 days, 5 days and 7 days, respectively. For initial test, cells from 5 days iron free cultivation was used for checking purification performance.

After cultivation cells were disrupted and purified as described in the Method section, and Ni-NTA column was used for purification since the PSI contained His-tagged PsaF subunit. After Ni-NTA purification, protein sample was further polished by Sucrose Density Gradient (SDG) centrifugation. **Figure 4-11** presented result of SDG, and different strategy was applied for extraction since the lower part of protein bound (B2~B3) was continuous and obscure. The protein samples from lest two SDG tubes were separated and extracted by stages as B1, B2 and B3, and continuously extracted from bottom (number 1) to the top of sample (number 21) from right SDG tube as marked in **Fig. 4-11**. The chlorophyll concentration of each fraction from 1 to 21 was measured and visualized in **Fig. 4-12**. Fractions marked out by red arrows were applied to mark out the fractions for SDS-PAGE checking in **Fig. 4-13**, and B1, B2 and B3 samples were also checked by SDS-PAGE.

After initial testing, BP-1 cells from different iron-deficient cultivation time (Fe- 3days, 5days and 7 days) were disrupted and purified identically as initial test. The SDG was performed (2 tubes for each sample) and result are presented in **Fig. 4-4**. No obvious difference could be observed, and the band distribution pattern as quite similar as sample from normal cultivation (Fe+ control at left of figure). Each band was extracted by stages into band A (3-A, 5-A, 7-A and B1 in Fe+ control), B (3-B, 5-B, 7-B and B2 in Fe+ control) and C (3-C, 5-C, 7-C and B3 in Fe+ control). After extraction, protein samples were checked by SDS-PAGE as presented in **Fig. 4-5**. The “Cr” sample in the figure was

solubilized PSI crystals, which as an evidence that all subunits were present in PSI trimer crystals.

The SDS-PAGE result showed obvious difference that an extra band (marked by red box) at molecular weight area about 32 kDa, which indicated the expression and attachment of IsiA antenna protein. The N-terminal amino acid sequencing result of it showed high homology of this band to the IsiA gene (**Fig. 4-14**), which was treated as an evidence that this band was IsiA protein.

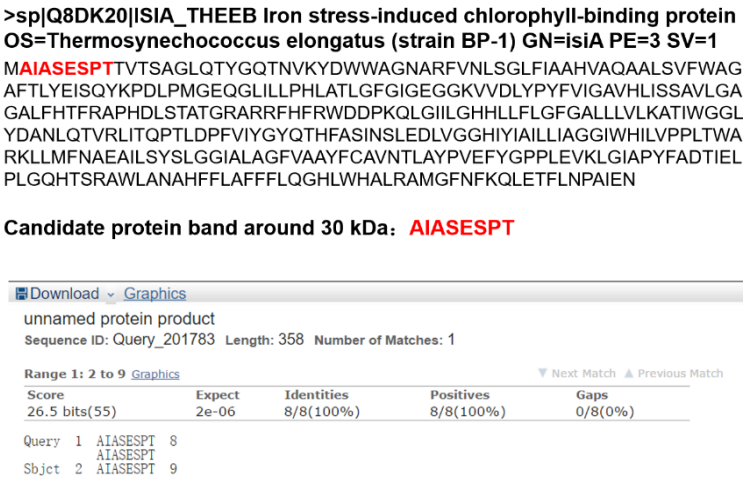

Figure 4-14 N-terminal sequencing result of IsiA-like bound from SDS-PAGE

Negative staining EM was performed to each band of protein sample, which was presented in **Fig. 4-6** at same magnification (40k). There was not dramatic difference in band A and B, but particle diameter showed distinguishable change in band C, especially in sample 7-C. The increasing of protein complex diameter indicated the attaching of IsiA antenna surrounding the PSI trimer, which consistent with the increasing amount of IsiA in SDS-PAGE band.

Since there were still numerous contaminant proteins after SDG based on negative staining result, further polishing was required to obtain PSI-IsiA supercomplex sample in high purity. Several types of chromatography methods were applied to test purification

performance including size exclusion chromatography (Gel filtration, such as HiLoad 16/600 Superose 6 PG and HiLoad® 16/600 Superdex® 75 pg) and ion-exchange chromatography (HiTrap® DEAE Fast Flow and HiTrap® Q Fast Flow). **Figure 4-15** presented the chromatogram of typical size exclusion chromatography result, only single peak could be detected during elution. Fractions from different part of the single peak were checked by negative staining as presented in **Fig. 4-16**. Both size exclusion chromatography columns presented similar results, and no fraction with homogeneous PSI-IsiA complexes was obtained by this method.

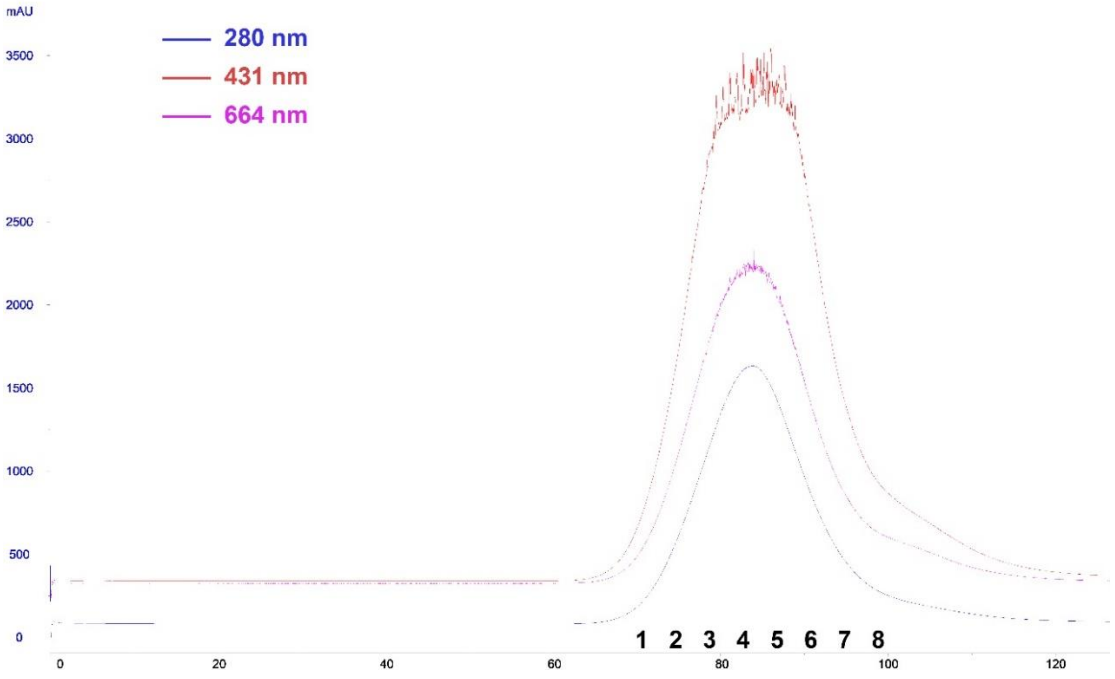

Figure 4-15 Gel filtration chromatogram. Fractions were marked at where number located.

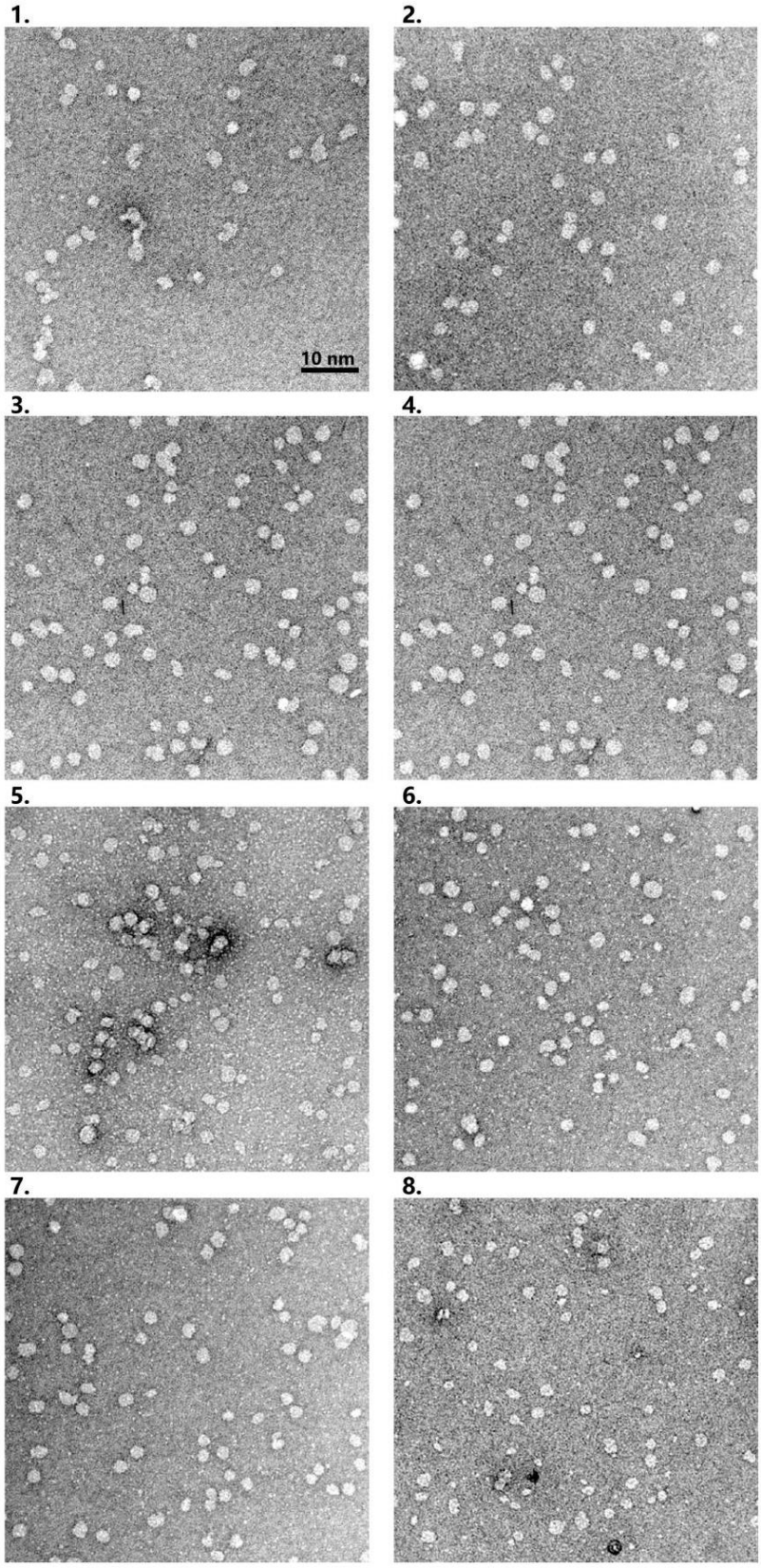

Figure 4-16 Negative staining results of fractions after gel filtration

4.3.2 Chromatography purification results

Anion exchange chromatography (HiTrap® Q Fast Flow) was performed in buffer containing 20 mM MES (pH 6.5), 0.05% β-DDM and linear gradient of $MgSO_4$ starting from 10 mM to 250 mM as **Fig. 4-17** showed. The flowing through fractions (Q1 and Q2) and elution fractions (Q3, Q4 and Q5) were checked by SDS-PAGE (**Fig. 4-18**) and negative staining EM (**Fig. 4-19**).

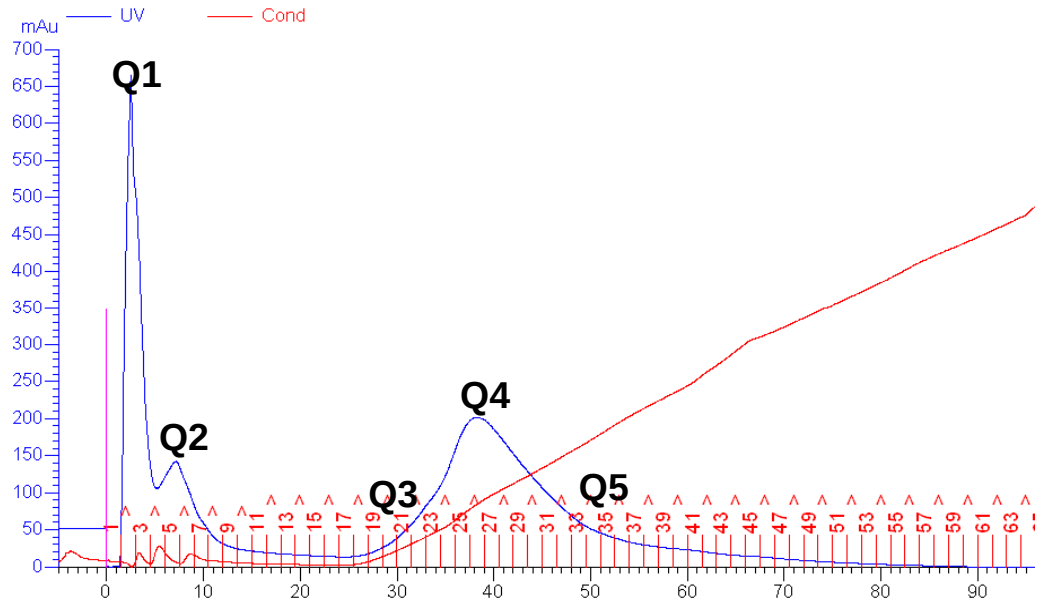

Figure 4-17 Anion exchange chromatogram (Q column). Fractions were marked at where tags (Q1-Q5) located.

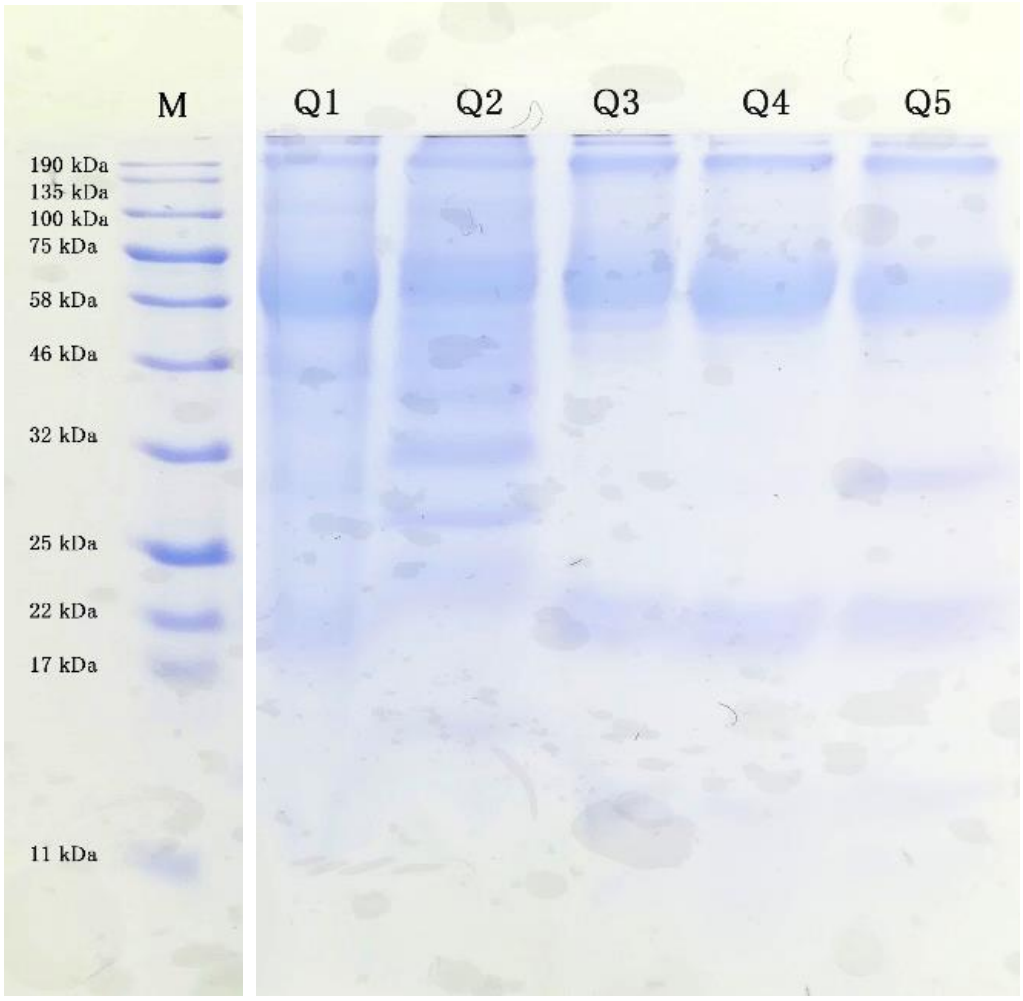

Figure 4-18 SDS-PAGE results of each fraction from Q column

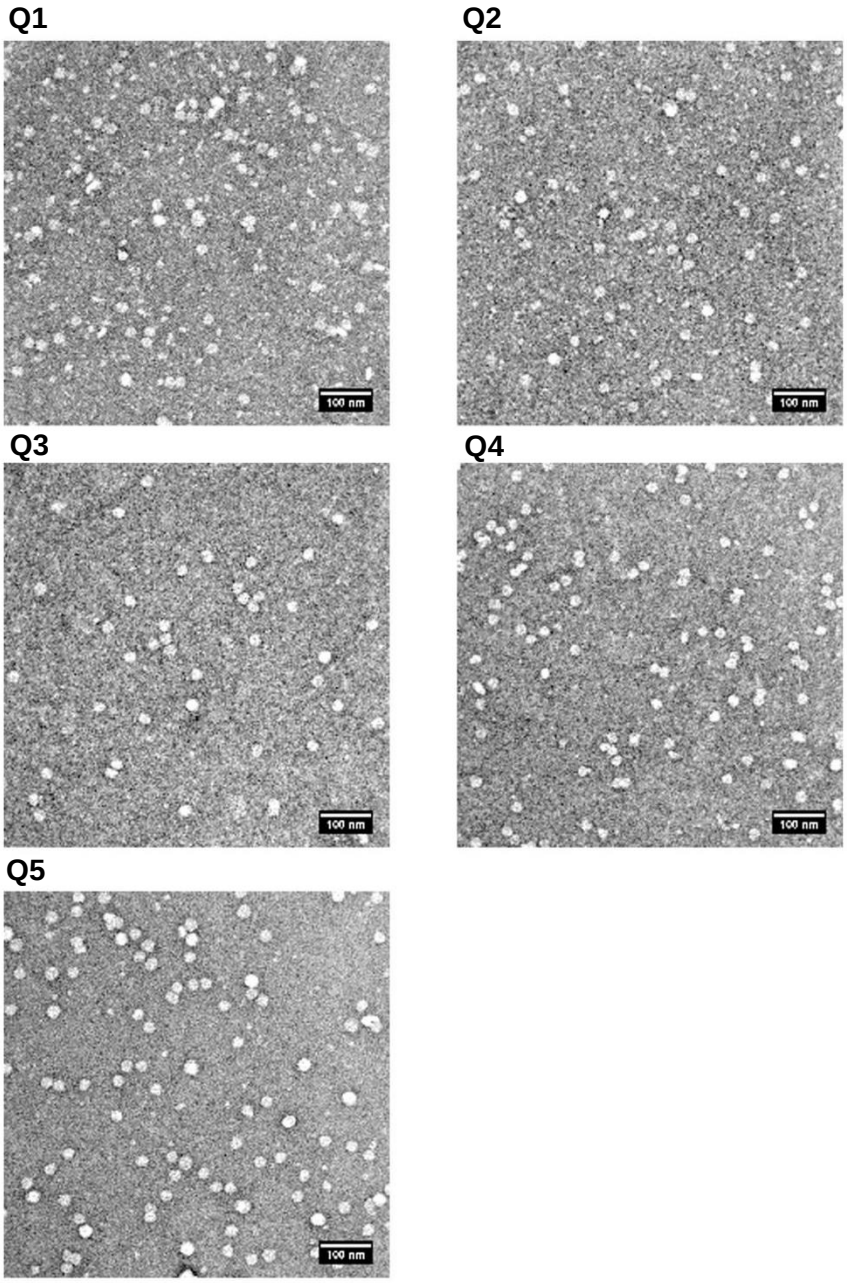

Figure 4-19 Negative staining results of fractions from Q-column purification

Weak anion exchange chromatography (HiTrap® DEAE Fast Flow) was also performed for purification performance checking. The buffer contained 20 mM MES (pH 6.5), 10 mM $MgSO_4$, 0.05% β-DDM and stepped gradient of NaCl starting from 0 to 100, 150, 200, 250 and 300 mM for elution as shown in **Fig. 4-20**. No detectable flowing through fraction was observed, and fractions from each elution step were collected and

checked by negative staining (**Fig. 4-21**). In general, no obvious polishing effect was observed based on negative staining result, although most IsiA antenna proteins were still attached to PSI trimers.

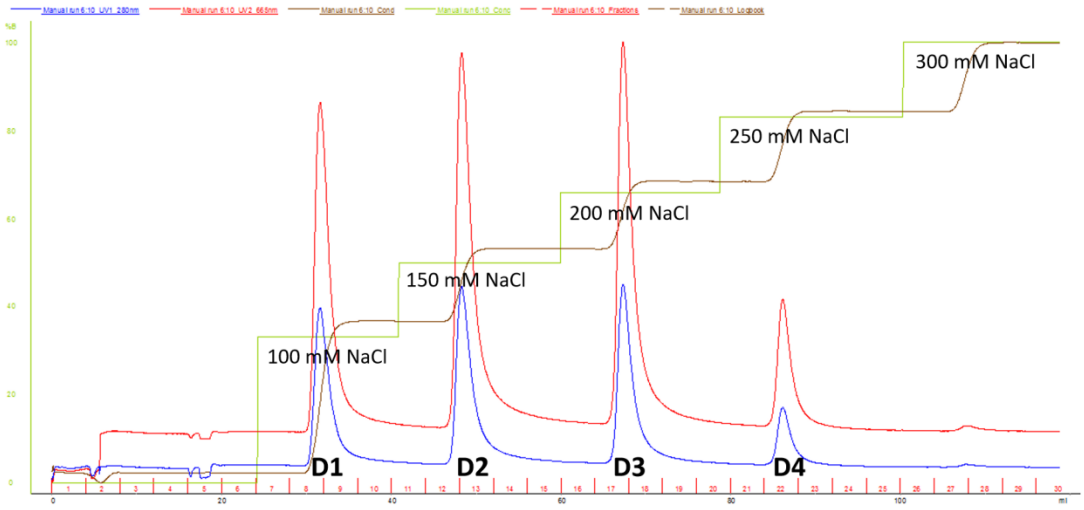

Figure 4-20 DEAE column chromatogram. Fractions marked at where tags located.

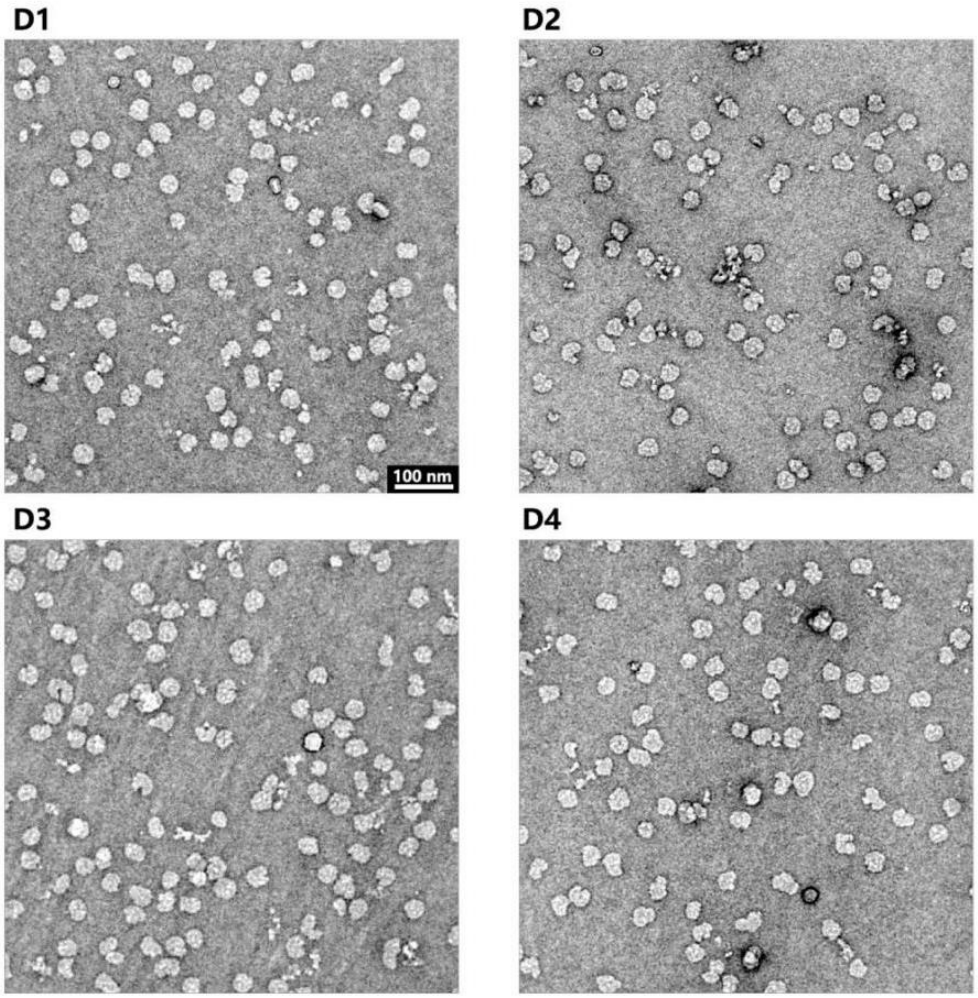

Figure 4-21 Negative staining results of fractions from DEAE column purification.

Since the adverse effect of Ni-NTA affinity chromatography was detected during purification tests (see **Fig. 4-8** and **Fig. 4-9**). Other purification methods without Ni-NTA column was explored including two-rounds SDG. The second round SDG used sample extracted from corresponding region of first round SDG tube which containing PSI-IsiA supercomplex. Mild detergent exchange could be also realized during second round SDG, which used gradient buffer containing other detergent (in this case 0.005% GDN, which was found to be more proper to solubilize supercomplexes in other tests). Most contaminants could be removed after the second round of SDG, and negative staining

was performed to check the sample quality extracted from second round SDG tube. **Figure 4-22** presented two-rounds SDG results as well as negative staining result. The supercomplex sample containing complete IsiA antenna ring (in red circles) could be detected, which was used for cryo-EM grid making test.

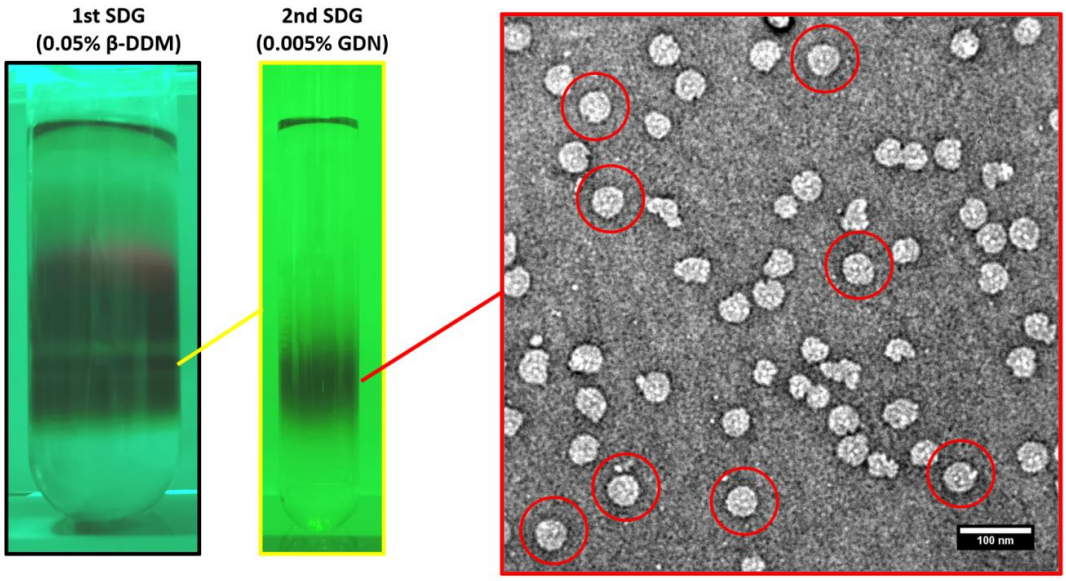

Figure 4-22 Two-rounds SDG and negative staining result.

4.3.3 Cryo-grids of purified sample

Cryo-grids were prepared as described in Method section, and checked by using a Talos Arctica (Thermo Fisher Scientific) transmission cryo electron microscope operated at 200 kV. **Figure 4-23** showed the typical micrograph of the purified sample in optimal buffer containing 75 mM NaCl, 30 mM Tricine-NaOH (pH8.0) and 0.005% GDN. Contaminant-like features were detected, indicating the antenna proteins detached from PSI trimer during grid making. Stacking-like aggregates were also observed in micrograph, which may cause potential adverse effect to following data processing (single particle auto-picking).

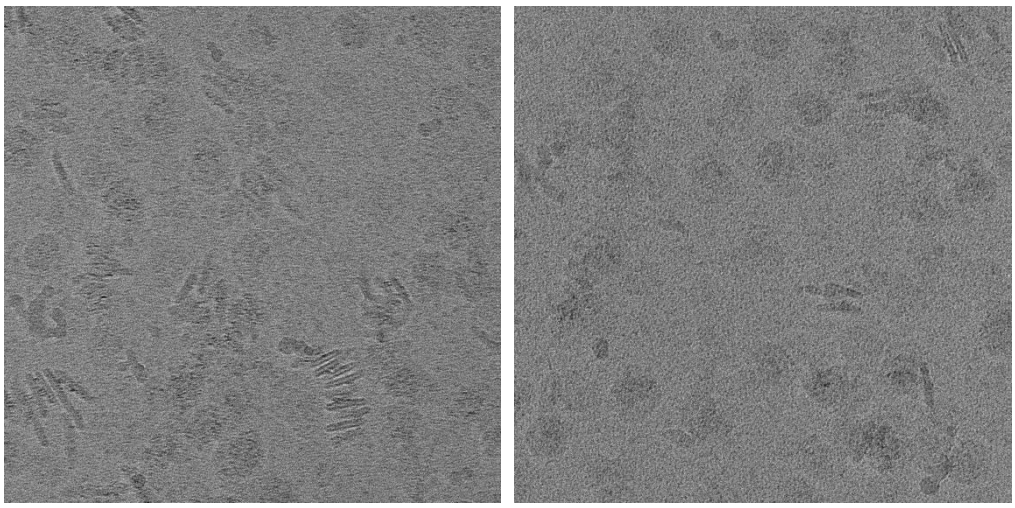

Figure4-23 Cryo-EM micrograph of PSI-IsiA supercomplex sample

4.4 Discussion

In this section, many attempts were described that performed to purify the PSI-IsiA supercomplex, which consists of PSI trimer “core” and surrounded IsiA antenna “ring” formed under iron-deficient cultivation condition. Many optimization trials during all stages were tested, which included iron-free cultivation time (also contained medium composition and brightness optimization, but not described in detail), cell disruption method and purification strategy.

In general, many factors could affect final purification result, and the purification strategy played the most important role in it based on the current results from negative staining transmission electron microscopy. The application of Ni-NTA affinity chromatography in the early stage of purification strategy exploration was a non-negligible fault, which caused IsiA antenna protein detached from PSI core during elution. The “disappearance” of IsiA antenna after purification caused frustration for a long time, until the experiment about iron-deficient cultivation time. During that experiment, Ni-NTA column was not washed as adequately as before since the resin amount was decreased from 20 mL to 10 mL. Shorter washing time and less column washing resulted in less losing of antenna protein, and finally got the negative staining result of distinguishable PSI-IsiA supercomplex and IsiA band in SDS-PAGE.

The adverse effect of Ni-NTA affinity chromatography derived from two possible reasons. The first reason was weak binding of IsiA antenna protein to the PSI trimer. Based on the cryo-EM structure determined recently, the interaction surface between IsiA and PSI trimer is very diversity and some of the antenna protein have only weak interactions with PSI, which likely is the reason of easy detachment from the PSI core. Another possibility was the detergent, which was added for stabilize the membrane after thylakoid membrane solubilization. Although PSI trimer could keep in relative stable status in buffer containing proper detergent, PSI-IsiA supercomplex may not be kept as complete architecture in same buffer. After buffer optimization in aspect of components composition and detergent type/concentration, proper buffer with ability of stabilizing PSI-IsiA was determined.

Beside the purification strategy, the cultivation procedure also affects the expression of IsiA protein and forming of supercomplex as previous literature described. Results from atomic force microscopy (AFM)[44] of thylakoid membranes demonstrated the diversity of supercomplexes *in situ*, showing the existence of double and even triple antenna rings surrounding the PSI monomer or trimer. Previous negative staining result also showed the existence of antenna-only features, which was empty at the center of it. These could be treated as the evidence for the high diversity and complexity of the photosynthetic molecular machinery.

Other practical details of the purification also affect the result such as the methods for cell disruption or protein concentration. Based on negative staining result, osmotic shock was determined as the optimal method for cell disruption. The mechanism was that, permeability of cell wall would be enhanced and became fragile after incubation in Lysozyme buffer, and hypertonic buffer could increase inner-cell osmotic pressure. Frozen by liquid nitrogen further reduced the flexibility of the cell membrane. Finally, sudden osmotic change caused by flooding hypotonic buffer into hypertonic buffer could result into cell crack-up. As for the PEG precipitation, which was applied as an effective protein concentrating step, proved to be adverse by negative staining result. The protein complex tended to form dimer-like

aggregates that not exist in case of applying other concentrating methods such as ultrafiltration. Such kind of dimer-like particles were treated as novel form of PSI-related complex, but proved to be an artifact caused by PEG precipitation.

In recent years, with more attention focusing on this stress-induced protein supercomplex, more structural biological results of PSI-IsiA supercomplex came out with more detailed investigations. In 2019, the first PSI-IsiA cryo-EM density map was determined in the overall resolution of 3.5 Å derived from *Synechocystis* sp. PCC 6803, based on which, the atomic model with the form of PSI_3-$IsiA_{18}$ was built. Such model stood out in regard to the size, flexibility and diversity of function when compared with other photosynthetic supercomplexes. In 2020, two relevant structures were determined by cryo-EM, one was PSI-IsiA supercomplex derived from *Thermosynechococcus vulcanus* in resolution of 2.74 Å[160], and another was PSI–IsiA–flavodoxin triple complex from *Synechococcus* sp. PCC 7942 in the resolution of 3.3 Å[87] (as well as PSI-IsiA structure from same strain in resolution of 2.9 Å). The improved resolution benefitted from the developing of cryo-EM "resolution revolution[57]" made it possible to build atomic model as well as atomic model based spatial pigment diagrams in higher accuracy. The optimized techniques for protein sample preparation and purification (such as using trehalose instead of sucrose during the density gradient centrifugation, and the novel thylakoid membrane solubilization method by applying detergent α-DDM) protected the completeness of supercomplex from disintegration and aggregation, which also shed light on our future trials of weak-bound and multi-partners membrane protein complex purification.

To summarize, in this section we tried to cultivate cyanobacteria BP-1 in iron-deficient condition for IsiA expression and tried to purify PSI-IsiA supercomplex for structural analysis. The PSI-IsiA supercomplex in major form of PSI_3-$IsiA_{18}$ was obtained, but more efforts needed to be made for optimization of cryo-grid and sample purity.

Chapter V. Concluding Remarks

The major research results described in this thesis, and almost all of author's efforts were focused on the trimeric form of Photosystem I from cyanobacteria *T. elongatus* BP-1. This protein-pigment complex with over 1 MDa molecular weights presented high value for further exploration because of its excellent electron transfer efficiency as well as its thermostability. The energy is treated as first priority for the organisms to live on, and study on how photosynthesis is realized in primary photoautotrophs is with irreplaceable scientific research value. The emergence of these giant, complex molecular machines have made a profound effect on this planet. Understanding of the theoretical molecular mechanism relied on the structural information details, which also contain practical potentials such as artificial photosynthesis and bio-photo sensor. These potential applications play more important role with the background of worse environmental issues in the modern society.

In Chapter II, crystallization trials were performed to the PSI trimers. Limited resolution of X-ray diffraction test blocked the acquisition of detailed structural information. The most progressed topic was described in Chapter III, which focus on the binding site of PSI's electron transfer partners. We got the current highest resolution PSI structure in all published articles, which benefited from the cutting-edged cryo-EM equipment and optimal protein sample as well as advanced data processing program. Fortunately, the Cryo-EM density map presented clear interaction surface between Ga-substituted Ferredoxin and PSI, which was much better than pervious researches. The atomic model of PSI-Fd complex as well as the ITC measurement results made it possible to make convincing descriptions on their binding mode from both structure biological view and thermodynamic view. However, it was a pity that Cyt c_6 could not be modeled precisely with the reason of limited local resolution, more optimization trials were required to get correct orientation of Cyt c_6 binding. In Chapter IV, PSI trimers with IsiA antenna rings were purified from iron-deficient cultured BP-1, whereas the diversity of supercomplex forming and poor homogeneity hindered Cryo-EM single particle analysis. The optimization of sample purification is still on the way.

The research of giant protein complexes is never-ending, and I hope the results described in this thesis could make at least a little contribution to the understanding of nature.

References

1. Fischer, W. *et al.* Evolution of oxygenic photosynthesis. *Annu. Rev. Earth Planet. Sci.* **44**, 647–683 (2016).
2. Blankenship, R. Molecular mechanisms of photosynthesis. 314 (2021)
3. Blackman, F. Optima and limiting factors. *Annals of Botany* **19**, 281–295 (1905).
4. Buchanan, B. The carbon (formerly dark) reactions of photosynthesis. *Photosynth Res* **128**, 215–217 (2016).
5. Anderson, J. Photoregulation of the composition, function, and structure of thylakoid membranes. *Annu. Rev. Plant. Physiol.* **37**, 93–136 (1986).
6. Allen, J. F. & Forsberg, J. Molecular recognition in thylakoid structure and function. *Trends in Plant Science* **6**, 317–326 (2001).
7. Umena, Y. *et al.* Crystal structure of oxygen-evolving photosystem II at a resolution of 1.9 Å. *Nature* **473**, 55–60 (2011).
8. Malone, L. *et al.* Cytochrome b_6f -orchestrator of photosynthetic electron transfer. *Biochimica et Biophysica Acta (BBA) - Bioenergetics* **1862**, 148380 (2021).
9. Fromme, P. *et al.* Structure of photosystem I. *Biochimica et Biophysica Acta (BBA) - Bioenergetics* **1507**, 5–31 (2001).
10. Battchikova, N. *et al.* Cyanobacterial NDH-1 complexes: novel insights and remaining puzzles. *Biochimica et Biophysica Acta (BBA) - Bioenergetics* **1807**, 935–944 (2011).
11. Hug, L. *et al.* A new view of the tree of life. *Nat Microbiol* **1**, 16048 (2016).
12. Ward, L. *et al.* Evolutionary implications of anoxygenic phototrophy in the bacterial phylum candidatus eremiobacterota (WPS-2). *Front. Microbiol.* **10**, 1658 (2019).
13. Hohmann-Marriott, M. F. & Blankenship, R. E. Evolution of photosynthesis. *Annu. Rev. Plant Biol.* **62**, 515–548 (2011).
14. Castenholz, R. *et al.* Phylum BX. cyanobacteria. *Bergey's Manual® of Systematic Bacteriology.* Springer, 473-599 (2001)
15. Shih, P. *et al.* Improving the coverage of the cyanobacterial phylum using

diversity-driven genome sequencing. *Proceedings of the National Academy of Sciences* **110**, 1053–1058 (2013).

16. Whitton, B. *et al.* Introduction to the cyanobacteria. *Ecology of cyanobacteria II.* Springer, 1-13 (2012)
17. Cardona, T. Photosystem II is a chimera of reaction centers. *J Mol Evol* **84**, 149–151 (2017).
18. Cardona, T. Thinking twice about the evolution of photosynthesis. *Open Biol.* **9**, 180246 (2019).
19. Cardona, T. & Rutherford, A. W. Evolution of photochemical reaction centres: more twists? *Trends in Plant Science* **24**, 1008–1021 (2019).
20. Sánchez-Baracaldo, P. & Cardona, T. On the origin of oxygenic photosynthesis and cyanobacteria. *New Phytol* **225**, 1440–1446 (2020).
21. O'Malley, M. A. Endosymbiosis and its implications for evolutionary theory. *Proc Natl Acad Sci USA* **112**, 10270–10277 (2015).
22. Guerrero R. *et al.* Symbiogenesis: the holobiont as a unit of evolution." *Int Microbiol* 133-143 (2013)
23. Martin, W. *et al.* Evolutionary analysis of arabidopsis, cyanobacterial, and chloroplast genomes reveals plastid phylogeny and thousands of cyanobacterial genes in the nucleus. *Proceedings of the National Academy of Sciences* **99**, 12246–12251 (2002).
24. Raven, J. A. & Allen, J. F. Genomics and chloroplast evolution: what did cyanobacteria do for plants? *Genome Biology* 5 (2003).
25. Giovannoni, S. *et al.* Evolutionary relationships among cyanobacteria and green chloroplasts. *J Bacteriol* **170**, 3584–3592 (1988).
26. Strasserf, R. J. & Alaka, S. Polyphasic chlorophyll *a* fluorescence transient in plants and cyanobacteria. *Photochemistry and photobiology* **61**, 32-42 (1995)
27. Barber, J. A mechanism for water splitting and oxygen production in photosynthesis. *Nature Plants* **3**, 17041 (2017).

28. Holland, H. D. The oxygenation of the atmosphere and oceans. *Phil. Trans. R. Soc. B* **361**, 903–915 (2006).
29. Farquhar, J. *et al.* Geological constraints on the origin of oxygenic photosynthesis. *Photosynth Res* **107**, 11–36 (2011).
30. Emerson R. & Lewis C. M. The dependence of the quantum yield of Chlorella photosynthesis on wave lenghth of light. *American Journal of Botany*, 165-178 (1943)
31. Emerson, R. *et al.* Some factors influencing the long-wave limit of photosynthesis. *Proceedings of the National Academy of Sciences* **43**, 133-143 (1957)
32. Govindjee, R. E. & Rabinowitch, E. Two Forms of Chlorophyll *a in vivo* with Distinct Photochemical Functions. *Science* **132**, 355–356 (1960).
33. Hill, R. & Bendall, F. Function of the two cytochrome components in chloroplasts: a working hypothesis. *Nature* **186**, 136–137 (1960).
34. Govindjee, S. D. & Björn, L. O. Evolution of the Z-scheme of photosynthesis: a perspective. *Photosynth Res* **133**, 5–15 (2017).
35. Zouni, A. *et al.* Crystal structure of photosystem II from *Synechococcus elongatus* at 3.8 Å resolution. *Nature* **409**, 739–743 (2001).
36. Jordan, P. *et al.* Three-dimensional structure of cyanobacterial photosystem I at 2.5 Å resolution. *Nature* **411**, 909–917 (2001).
37. Croce, R. & van Amerongen, H. Light-harvesting in photosystem I. *Photosynth Res* **116**, 153–166 (2013).
38. Golbeck, J. H. Photosystem I: the light-driven plastocyanin: ferredoxin oxidoreductase. *Springer Science & Business Media*, Vol. **24**. (2007)
39. De la Rosa, M. A. *et al.* An evolutionary analysis of the reaction mechanisms of photosystem I reduction by cytochrome c_6 and plastocyanin. *Bioelectrochemistry* **55**, 41–45 (2002).
40. Sétif, P. Ferredoxin and flavodoxin reduction by photosystem I. *Biochimica et Biophysica Acta (BBA)-Bioenergetics* **1507**, 161-179 (2001)

41. Latimer, P. *et al.* Quantum yields of fluorescence of plant pigments. *Science* **124**, 585–586 (1956).
42. Harwood, J. L. Plant lipid metabolism. *Plant biochemistry* 237–271 (1997).
43. Boekema, E. J. *et al.* Refined analysis of the trimeric structure of the isolated Photosystem I complex from the thermophilic cyanobacterium *Synechococcus* sp. *Biochimica et Biophysica Acta (BBA) - Bioenergetics* **974**, 81–87 (1989).
44. Zhao, L. *et al.* Structural variability, coordination and adaptation of a native photosynthetic machinery. *Nat. Plants* **6**, 869–882 (2020).
45. Netzer-El, S. *et al.* N. Crystal structure of Photosystem I monomer from *Synechocystis* PCC 6803. *Front Plant Sci* **9**, 1865 (2018).
46. Zheng, L. *et al.* Structural and functional insights into the tetrameric photosystem I from heterocyst-forming cyanobacteria. *Nat. Plants* **5**, 1087–1097 (2019).
47. Amunts, A. & Nelson, N. Plant Photosystem I design in the light of evolution. *Structure* **17**, 637–650 (2009).
48. Pålsson, L.-O. *et al.* Energy transfer and charge separation in Photosystem I: P700 oxidation upon selective excitation of the long-wavelength antenna chlorophylls of *Synechococcus elongatus*. *Biophysical Journal* **74**, 2611–2622 (1998).
49. Sétif, P. *et al.* The ferredoxin docking site of photosystem I. *Biochimica et Biophysica Acta (BBA) - Bioenergetics* **1555**, 204–209 (2002).
50. Knaff, D. B. & Hirasawa, M. Ferredoxin-dependent chloroplast enzymes. *Biochimica et Biophysica Acta (BBA) - Bioenergetics* **1056**, 93–125 (1991).
51. Hanke, G. & Mulo, P. Plant type ferredoxins and ferredoxin-dependent metabolism: Chloroplast ferredoxins. *Plant Cell Environ* **36**, 1071–1084 (2013).
52. Hervás, M. *et al.* A comparative thermodynamic analysis by laser-flash absorption spectroscopy of Photosystem I reduction by plastocyanin and Cytochrome c_6 in *Anabaena* PCC 7119, *Synechocystis* PCC 6803, and Spinach. *Biochemistry* **35**, 2693–2698 (1996).

53. Malavath, T. *et al.* Structure and function of wild-type and subunit-depleted photosystem I in Synechocystis. *Biochim Biophys Acta Bioenerg* **1859**, 645–654 (2018).
54. Wang, J. *et al.* Structure of plant photosystem I−light harvesting complex I supercomplex at 2.4 Å resolution. *J. Integr. Plant Biol.* **63**, 1367–1381 (2021).
55. Xu, C. *et al.* Structural basis for energy transfer in a huge diatom PSI-FCPI supercomplex. *Nat Commun* **11**, 5081 (2020).
56. Nagao, R. *et al.* Structural basis for assembly and function of a diatom photosystem I-light-harvesting supercomplex. *Nat Commun* **11**, 2481 (2020).
57. Kuhlbrandt, W. The resolution revolution. *Science* **343**, 1443–1444 (2014).
58. Kato, K. *et al.* Structural basis for the adaptation and function of chlorophyll *f* in photosystem I. *Nat Commun* **11**, 238 (2020).
59. Battye, T. *et al. iMOSFLM* : a new graphical interface for diffraction-image processing with *MOSFLM*. *Acta Crystallogr D Biol Crystallogr* **67**, 271–281 (2011).
60. Havaux, M. Plastoquinone in and beyond photosynthesis. *Trends in Plant Science* **25**, 1252–1265 (2020).
61. Redinbo, M. *et al.* Plastocyanin: structural and functional analysis. *J Bioenerg Biomembr* **26**, 49–66 (1994).
62. Eberhard, S. *et al.* The dynamics of photosynthesis. *Annu. Rev. Genet.* **42**, 463–515 (2008).
63. Nugent, J. Oxygenic photosynthesis: electron transfer in Photosystem I and Photosystem II. *Eur J Biochem* **237**, 519–531 (1996).
64. Wood, P. M. Interchangeable copper and iron proteins in algal photosynthesis: studies on plastocyanin and cytochrome *c*-552 in *Chlamydomonas*. *Eur J Biochem* **87**, 9–19 (1978).
65. Lambreva, M. *et al.* Structure/function/dynamics of photosystem II plastoquinone binding sites. *CPPS* **15**, 285–295 (2014).
66. Graan, T. & Ort, D. R. Detection of oxygen-evolving photosystem II centers inactive in

plastoquinone reduction. *Biochimica et Biophysica Acta (BBA) - Bioenergetics* **852**, 320–330 (1986).

67. Kurisu, G. *et al.* Structure of the cytochrome b_6f complex of oxygenic photosynthesis: tuning the cavity. *Science* **302**, 1009–1014 (2003).
68. Kölsch, A. *et al.* Current limits of structural biology: The transient interaction between cytochrome *c* and photosystem I. *Current Research in Structural Biology* **2**, 171–179 (2020).
69. Croce, R. A close view of photosystem I. *Science* **348**, 970–971 (2015).
70. Qin, X. *et al.* Structural basis for energy transfer pathways in the plant PSI-LHCI supercomplex. *Science* **348**, 989–95 (2015).
71. Ilbert, M. & Bonnefoy, V. Insight into the evolution of the iron oxidation pathways. *Biochimica et Biophysica Acta (BBA) - Bioenergetics* **1827**, 161–175 (2013).
72. Sandmann, G. Formation of plastocyanin and cytochrome *c*-553 in different species of blue-green algae. *Arch. Microbiol.* **145**, 76–79 (1986).
73. García-Cañas, R. *et al.* A protease-mediated mechanism regulates the cytochrome c_6/plastocyanin switch in *Synechocystis* sp. PCC 6803. *Proc Natl Acad Sci USA* **118** (2021).
74. Falke, S. *et al.* Crystal structures of native cytochrome c_6 from *Thermosynechococcus elongatus* in two different space groups and implications for its oligomerization. *Acta Crystallogr F Struct Biol Commun* **76**, 444–452 (2020).
75. Nakamura, Y. Complete genome structure of the thermophilic cyanobacterium *Thermosynechococcus elongatus* BP-1. *DNA Research* **9**, 123–130 (2002).
76. Weigel, M. *et al.* Plastocyanin is indispensable for photosynthetic electron flow in *Arabidopsis thaliana*. *Journal of Biological Chemistry* **278**, 31286–31289 (2003).
77. Gupta, R. *et al.* Functional relationship of cytochrome c_6 and plastocyanin in Arabidopsis. *Nature* **417**, 567–571 (2002).
78. Wastl, J. *et al.* Higher plants contain a modified cytochrome c_6. *Trends in plant science* **7**,

244-245 (2002)

79. Setif, P. Q. Y. & Bottin, H. Laser flash absorption spectroscopy study of ferredoxin reduction by Photosystem I: spectral and kinetic evidence for the existence of several Photosystem I-ferredoxin complexes. *Biochemistry* **34**, 9059-9070 (1995)
80. Mutoh, R. *et al.* X-ray structure and nuclear magnetic resonance analysis of the interaction sites of the Ga-Substituted cyanobacterial ferredoxin. *Biochemistry* **54**, 6052–6061 (2015).
81. Mignée, C. *et al.* Gallium ferredoxin as a tool to study the effects of ferredoxin binding to photosystem I without ferredoxin reduction. *Photosynth Res* **134**, 251–263 (2017).
82. Kubota-Kawai, H. *et al.* X-ray structure of an asymmetrical trimeric ferredoxin–photosystem I complex. *Nature Plants* **4**, 218–224 (2018).
83. Barth, P. *et al.* Ferredoxin reduction by Photosystem I from *Synechocystis* sp. PCC 6803: toward an understanding of the respective roles of subunits PsaD and PsaE in ferredoxin binding. *Biochemistry* **37**, 16233–16241 (1998).
84. Lelong, C. *et al.* Characterization of a redox active cross-linked complex between cyanobacterial photosystem I and soluble ferredoxin. *The EMBO Journal* **15**, 2160–2168 (1996).
85. van Thor, J. *et al.* Kinetic evidence for the PsaE-dependent transient ternary complex Photosystem I/Ferredoxin/Ferredoxin:$NADP^+$ Reductase in a cyanobacterium. *Biochemistry* **38**, 12735–12746 (1999).
86. Fischer, N. The PsaC subunit of photosystem I provides an essential lysine residue for fast electron transfer to ferredoxin. *The EMBO Journal* **17**, 849–858 (1998).
87. Cao, P. *et al.* Structural basis for energy and electron transfer of the photosystem I–IsiA–flavodoxin supercomplex. *Nat. Plants* **6**, 167–176 (2020).
88. Huang, Z. *et al.* Structure of photosystem I-LHCI-LHCII from the green alga *Chlamydomonas reinhardtii* in State 2. *Nat Commun* **12**, 1100 (2021).
89. Caspy, I. *et al.* The structure of a triple complex of plant photosystem I with ferredoxin

and plastocyanin. *Nat. Plants* **6**, 1300–1305 (2020).

90. Caspy, I. *et al.* Structure of plant photosystem I-plastocyanin complex reveals strong hydrophobic interactions. *Biochemical Journal* **478**, 2371–2384 (2021).
91. Allen, M. M. Simple conditions for growth of unicellular blue-green algae on plates. *Journal of phycology* **4**, 1-4 (1968):.
92. Kubota, H. *et al.* Purification and characterization of photosystem I complex from *Synechocystis sp.* PCC 6803 by expressing histidine-tagged subunits. *Biochim Biophys Acta* **1797**, 98–105 (2010).
93. Rögner, M. *et al.* Purification and characterization of photosystem I and photosystem II core complexes from wild-type and phycocyanin-deficient strains of the cyanobacterium *Synechocystis* PCC 6803. *Journal of Biological Chemistry* **265**, 6189–6196 (1990).
94. Hauer, F. *et al.* GraDeR: membrane protein complex preparation for single-particle cryo-EM. *Structure* **23**, 1769–1775 (2015).
95. Shin, M. *et al.* Purification of c-type cytochromes from a thermophilic blue-green alga, *Synechococcus vulcanus*, by hydrophobic column chromatography using toyopearls. *Plant and Cell Physiology* **25**, 1575–1578 (1984).
96. Koike, H. & Katoh, S. Heat-stabilities of cytochromes and ferredoxin isolated from a thermophilic blue-green alga. *Plant and Cell Physiology* **20**, 1157-1161 (1979)
97. Zivanov, J. *et al.* New tools for automated high-resolution cryo-EM structure determination in RELION-3. *eLife* **7**, e42166 (2018).
98. Pettersen, E. F. *et al.* UCSF Chimera—a visualization system for exploratory research and analysis. *J. Comput. Chem.* **25**, 1605–1612 (2004).
99. Zheng, S. *et al.* MotionCor2: anisotropic correction of beam-induced motion for improved cryo-electron microscopy. *Nat Methods* **14**, 331–332 (2017).
100. Rohou, A. & Grigorieff, N. CTFFIND4: fast and accurate defocus estimation from electron micrographs. *Journal of Structural Biology* **192**, 216–221 (2015).
101. Emsley, P. *et al.* Features and development of *Coot*. *Acta Crystallogr D Biol Crystallogr*

66, 486–501 (2010).

102. Liebschner, D. *et al.* Macromolecular structure determination using X-rays, neutrons and electrons: recent developments in *Phenix*. *Acta Crystallogr D Struct Biol* **75**, 861–877 (2019).
103. Moriarty, N. W. & Adams, P. D. Iron–sulfur clusters have no right angles. *Acta Crystallogr D Struct Biol* **75**, 16–20 (2019).
104. Hippler, M. *et al.* The N-terminal domain of PsaF: precise recognition site for binding and fast electron transfer from cytochrome c_6 and plastocyanin to photosystem I of *Chlamydomonas reinhardtii*. *Proceedings of the National Academy of Sciences* **95**, 7339–7344 (1998).
105. Drepper, F. *et al.* Binding dynamics and electron transfer between plastocyanin and photosystem I. *Biochemistry* **35**, 1282–1295 (1996).
106. Hervas, M. *et al.* Laser-flash kinetic analysis of the fast electron transfer from plastocyanin and cytochrome c_6 to photosystem I. Experimental Evidence on the Evolution of the Reaction Mechanism. *Biochemistry* **34**, 11321–11326 (1995).
107. Hippler, M. *et al.* Fast electron transfer from cytochrome c_6 and Plastocyanin to photosystem I of *Chlamydomonas reinhardtii* requires PsaF. *Biochemistry* **36**, 6343–6349 (1997).
108. Viola, S. *et al. In vivo* electron donation from plastocyanin and cytochrome *c* to PSI in *Synechocystis sp.* PCC6803. *Biochimica et Biophysica Acta (BBA) - Bioenergetics* **1862**, 148449 (2021).
109. Boudière, L. *et al.* Glycerolipids in photosynthesis: composition, synthesis and trafficking. *Biochimica et Biophysica Acta (BBA) - Bioenergetics* **1837**, 470–480 (2014).
110. Bottin, H. *et al.* Role of acidic amino acid residues of PsaD subunit on limiting the affinity of photosystem I for ferredoxin. *Biochemical and Biophysical Research Communications* **287**, 833–836 (2001).
111. Laskowski, R. & Swindells, M. LigPlot$^+$: Multiple ligand–protein interaction diagrams for

drug discovery. *J. Chem. Inf. Model.* **51**, 2778–2786 (2011).

112. Hippler, M. *et al.* The plastocyanin binding domain of photosystem I. *The EMBO Journal* **15**, 6374–6384 (1996).
113. Los, D. A. *et al.* Stress responses in *Synechocystis*: regulated genes and regulatory systems. *The cyanobacteria: molecular biology, genomics and evolution* 117-157 (2008)
114. Castielli, O. *et al.* Proteomic analyses of the response of cyanobacteria to different stress conditions. *FEBS Letters* **583**, 1753–1758 (2009).
115. Xiong, L. *et al.* Cell signaling during cold, drought, and salt stress. *Plant Cell* **14**, S165–S183 (2002).
116. Amme, S. Proteome analysis of cold stress response in *Arabidopsis thaliana* using DIGE-technology. *Journal of Experimental Botany* **57**, 1537–1546 (2006).
117. Donkor, V. & Häder, D. Effects of ultraviolet irradiation on photosynthetic pigments in some filamentous cyanobacteria. *Aquat. Microb. Ecol.* **11**, 143–149 (1996).
118. Xia, J. Response of growth, photosynthesis and photoinhibition of the edible cyanobacterium *Nostoc sphaeroides* colonies to thiobencarb herbicide. *Chemosphere* **59**, 561–566 (2005).
119. Dhankher, O. P. Arsenic metabolism in plants: an inside story. *New Phytologist* **168**, 503–505 (2005).
120. Andrews, S. *et al.* Bacterial iron homeostasis. *FEMS Microbiol Rev* **27**, 215–237 (2003).
121. Ferreira, F. & Straus, N. A. Iron deprivation in cyanobacteria. *J Appl Phycol* **6**, 199–210 (1994).
122. Shcolnick, S. *et al.* The mechanism of iron homeostasis in the unicellular cyanobacterium *Synechocystis sp.* PCC 6803 and its relationship to oxidative stress. *Plant Physiology* **150**, 2045–2056 (2009).
123. Coale, K. H. *et al.* A massive phytoplankton bloom induced by an ecosystem-scale iron fertilization experiment in the equatorial pacific ocean. *Nature* **383**, 495–501 (1996).
124. Richier, S. *et al.* Abundances of iron-binding photosynthetic and nitrogen-fixing proteins

of *Trichodesmium* both in culture and *in situ* from the north Atlantic. *PLoS ONE* **7**, e35571 (2012).

125. Latifi, A. *et al.* Oxidative stress in cyanobacteria. *FEMS Microbiol Rev* **33**, 258–278 (2009).
126. Latifi, A. *et al.* Iron starvation leads to oxidative stress in *Anabaena* sp. strain PCC 7120. *J Bacteriol* **187**, 6596–6598 (2005).
127. González, A. *et al.* FurA is the master regulator of iron homeostasis and modulates the expression of tetrapyrrole biosynthesis genes in *Anabaena sp.* PCC 7120. *Environmental Microbiology* **14**, 3175-3187 (2012)
128. Shcolnick, S. & Keren, N. Metal Homeostasis in cyanobacteria and chloroplasts. Balancing benefits and risks to the photosynthetic apparatus. *Plant Physiology* **141**, 805–810 (2006).
129. Morrissey, J. & Bowler, C. Iron utilization in marine cyanobacteria and eukaryotic algae. *Front. Microbio.* **3**, (2012).
130. Nicolaisen, K. *et al.* Alr0397 is an outer membrane transporter for the siderophore schizokinen in *Anabaena* sp. Strain PCC 7120. *J Bacteriol* **190**, 7500–7507 (2008).
131. Stevanovic, M. *et al.* The components of the putative iron transport system in the cyanobacterium *Anabaena sp.* PCC 7120: The iron transport system of *Anabaena sp.* *Environmental Microbiology* **14**, 1655–1670 (2012).
132. Ghassemian, M. & Straus, N. A. Fur regulates the expression of iron-stress genes in the cyanobacterium *Synechococcus sp.* strain PCC 7942. *Microbiology* **142**, 1469–1476 (1996).
133. González, A. *et al.* Expanding the role of FurA as essential global regulator in cyanobacteria. *PLoS ONE* **11**, e0151384 (2016).
134. González, A. *et al.* FurA influences heterocyst differentiation in *Anabaena sp.* PCC 7120. *FEBS Letters* **587**, 2682–2690 (2013).
135. González, A. *et al.* The FurA regulon in *Anabaena sp.* PCC 7120: *in silico* prediction and

experimental validation of novel target genes. *Nucleic Acids Research* **42**, 4833–4846 (2014).

136. Straus, N. A. Iron deprivation: physiology and gene regulation. *The molecular biology of cyanobacteria.* Springer, 731-750 (1994)
137. Peleato, M. *et al.* Iron homeostasis and environmental responses in cyanobacteria: Regulatory networks involving Fur. *Stress and Environmental Regulation of Gene Expression and Adaptation in Bacteria*, 1065-1078 (2016)
138. Michel, K.-P. & Pistorius, E. K. Adaptation of the photosynthetic electron transport chain in cyanobacteria to iron deficiency: The function of IdiA and IsiA. *Physiol Plant* **120**, 36–50 (2004).
139. Yingping, F. *et al.* Unravelling the cross-talk between iron starvation and oxidative stress responses highlights the key role of PerR (alr0957) in peroxide signalling in the cyanobacterium *Nostoc* PCC 7120: Oxidative stress and iron starvation crosstalk. *Environmental Microbiology Reports* **6**, 468–475 (2014).
140. Singh, A. K. *et al.* Microarray analysis of the genome-wide response to iron deficiency and iron reconstitution in the cyanobacterium *Synechocystis sp.* PCC 6803. *Plant Physiology* **132**, 1825–1839 (2003).
141. Leonhardt, K. & Straus, N. An iron stress operon involved in photosynthetic electron transport in the marine cyanobacterium *Synechococcus sp.* PCC 7002. *Journal of General Microbiology* **138**, 1613–1621 (1992).
142. Sherman, D. M. & Sherman, L. A. Effect of iron deficiency and iron restoration on ultrastructure of *Anacystis nidulans. J Bacteriol* **156**, 393–401 (1983).
143. Riethman, H. C. & Sherman, L. A. Purification and characterization of an iron stress-induced chlorophyll-protein from the cyanobacterium *Anacystis nidulans* R2. *Biochimica et Biophysica Acta (BBA) - Bioenergetics* **935**, 141–151 (1988).
144. Sun, J. & Golbeck, J. H. The presence of the IsiA-PSI supercomplex leads to enhanced photosystem I electron throughput in iron-starved cells of *Synechococcus* sp. PCC 7002.

J. Phys. Chem. B **119**, 13549–13559 (2015).

145. Schoffman, H. & Keren, N. Function of the IsiA pigment-protein complex *in vivo*. *Photosynth Res* **141**, 343–353 (2019).
146. Park, Y.-I. *et al.* Expression of the isiA gene is essential for the survival of the cyanobacterium *Synechococcus sp.* PCC 7942 by protecting photosystem II from excess light under iron limitation. *Mol Microbiol* **32**, 123–129 (1999).
147. Pakrasi, H. B. *et al.* Membrane development in the cyanobacterium, *Anacystis nidulans*, during recovery from iron starvation. *Plant Physiol.* **79**, 290–295 (1985).
148. De Las Rivas, J. & Barber, J. Analysis of the Structure of the PsbO protein and its implications. *Photosynthesis Research* **81**, 329–343 (2004).
149. Nogi, T. & Miki, K. Structural basis of bacterial photosynthetic reaction centers. *Journal of Biochemistry* **130**, 319–329 (2001).
150. Bibby, T. S. *et al.* Biogeography of photosynthetic light-Harvesting genes in marine phytoplankton. *PLoS ONE* **4**, e4601 (2009).
151. González, A. et al. The challenge of iron stress in cyanobacteria. *Cyanobacteria,* 109-138 (2018)
152. Pierella K. *et al.* Environmental selection pressures related to iron utilization are involved in the loss of the flavodoxin gene from the plant genome. *Genome Biology and Evolution* **7**, 750–767 (2015).
153. Razquin, P. *et al.* Differential activities of heterocyst ferredoxin, vegetative cell ferredoxin, and flavodoxin as electron carriers in nitrogen fixation and photosynthesis in *Anabaena sp. Photosynth Res* **43**, 35–40 (1995).
154. Fillat, M. F. *et al.* Structural and chemical properties of a flavodoxin from *Anabaena* PCC 7119. *Biochimica et Biophysica Acta (BBA) - Protein Structure and Molecular Enzymology* **1040**, 301–307 (1990).
155. Vigara, A. J. *et al.* Flavodoxin as an electronic donor in photosynthetic inorganic nitrogen assimilation by iron-deficient *Chlorella fusca* Cells. *Photochem Photobiol* **67**, 446–449

(1998).

156. Lodeyro, A. F. *et al.* The importance of flavodoxin for environmental stress tolerance in photosynthetic microorganisms and transgenic plants. Mechanism, evolution and biotechnological potential. *FEBS Letters* **586**, 2917–2924 (2012).
157. Boekema, E. *et al.* A giant chlorophyll–protein complex induced by iron deficiency in cyanobacteria. *Nature* **412**, 745–748 (2001).
158. Bibby, T. S. *et al.* Iron deficiency induces the formation of an antenna ring around trimeric photosystem I in cyanobacteria. *Nature* **412**, 743–5 (2001).
159. Bibby, T. S. *et al.* Three-dimensional model and characterization of the iron stress-induced CP43′-photosystem I supercomplex isolated from the cyanobacterium *Synechocystis* PCC 6803. *Journal of Biological Chemistry* **276**, 43246–43252 (2001).
160. Akita, F. *et al.* Structure of a cyanobacterial photosystem I surrounded by octadecameric IsiA antenna proteins. *Commun Biol* **3**, 232 (2020).